



10. - 12. April
2024

Freiberg

keep the fire of
metallurgy burning

27th International Students' Day of Metallurgy

– Conference Proceedings –



Preamble

On behalf of the board of our association ‘Metallurgiestudenten zu Freiberg e.V.’, we would like to express our gratitude to all participants, presenters, sponsors, and supporters of the 27th International Students’ Day of Metallurgy (ISDM) here at the TU Bergakademie Freiberg.

The ISDM serves as a forum for scientific and personal discussion, highlighting the benefit of networking in our area. We trust that the connections established during this event will significantly strengthen metallurgical knowledge and cooperation.

After a long absence due to several obstacles created by the COVID-19 pandemic, we are pleased to have the ISDM resurgent in Freiberg. This is an important milestone, indicating the start of a renewed commitment to keep the fire of metallurgy burning, also in the years ahead.

We are thankful about the opportunities that lay ahead and look forward to further engagement and collaboration within the metallurgical community.

With a cordial metallurgical Glück Auf

Johann Albert Gey, Janus Schaarschmidt and Lukas Neubert

The association’s board



Metallurgiestudenten
zu Freiberg e.V.

**Kontakte im Studium
und darüber hinaus!**

Stammtische, Exkursionen,
International Students' Day of Metallurgy



Traditionspflege & Networking
Finanz. Unterstützung von Studierenden
Werde Mitglied:  info@metallurgiestudenten.de
 www.metallurgiestudenten.de

Table of Contents

Preamble	2
Removal of copper from steel melts by way of vaporization from the tapping stream Andrä, S.	6
Examination of the foam behaviour of highly FeO rich EAF slags Angelini, A.	12
Hot deformation behaviour of Inconel 718 superalloy by SLM 3D-printing . . Benč, M.	18
CFD analysis of steel flow in the five-strand tundish at different casting speeds Cupek, J.; Walek, J.; Tkadlečková, M.	25
Overview about wear and plastic deformation of MP159 alloy Djimaoui, N.; Mertinger, V.; Adonyi, Y.	34
Analysis of the properties of hot work tool steel Długosz, J.; Bednarczyk, A.; Łukaszek – Sołek, A.; Ficak, G.	41
Application of modern manufacturing methods in sword blades restoration . Długosz, J.; Kokot, K.; Fidura, W.; Ledwig, P.	48
Variations in the wettability behavior of material surfaces caused by petroleum and hydraulic oil Fadhil, M.	55
Comparative study of the influence of selected trace elements on the phase transformation in medium-carbon steels Gruber, I.; Cejka, J.; Michelic, S. K.	64
Influence of Q & P-parameters and Al-content on the microstructural evolution of lean-medium-Mn-steels Höger, K.; Kaar-Schickinger, S.; Wallner, M.; Schneider, R.	73
Analysis of the impression die forging process of a forging model with elongated shape Kała, P.; Bednarczyk, A.; Łukaszek – Sołek, A.; Ficak, G.	82

Single-point incremental forming of thin metallic sheets with the use of the robotic arm	90
Knap, K.; Żarski, J.; Lisiecki, Ł.; Perzyński, K.; Madej, Ł.	
Strain aging phenomena at mild steels produced by today's steel making technology	97
Kondas, B.; Mertinger, V.	
Influencing parameters on reduction rate during hydrogen-based reduction of iron ore pellets	105
Kovtun, O.; Levchenko, M.; Aneziris, C. G.; Volkova, O.	
Mechanical properties of steel reinforcing bars	118
Magyari, Z. E.	
Microstructural transformations of DC01 carbon steel via cross-rolling process	124
Marouani, J.; Toth, L. S.; Szűcs, M.	
Anodizing Challenges in High-Silicon Aluminum Alloy AlSi12Cu1(Fe): Microstructural Impact and Thickness Variation under Different Surface Conditions and Power Modes	130
Razzouk, E.; Koncz-Horváth, D.; Török, T. I.	
Comparative study of inclusion modification with calcium for structural steel grade S235JR + N	139
Veszprémi, R.; Palkovics, M.; Szabó, G.	
Rolling Process Variation Estimation Using a Monte-Carlo Method	146
Weiner, M.; Renzing, C.; Schmidtchen, M.; Prahl, U.	
The effect of Fe impurity on the electrodeposition of Zn from spent pickling liquor	154
Zakiyya, H.; Kékesi, T.	

Removal of copper from steel melts by way of vaporization from the tapping stream

Stefan Andrä¹

¹ TU Bergakademie Freiberg

Copper is generally considered to be an undesirable element in steel production, mainly due to it causing hot shortness during rolling operations of the billet. It is introduced into the steel resource cycle during recycling of scrap. As it cannot be removed from steel melts via conventional means, a novel method of vaporization of copper during the tapping stream of a simulated BOF process has been proposed and investigated, as the BOF is one of the principal scrap recycling units. Experiments have been conducted at the vacuum induction furnace at the Institute of Iron and Steel Technology, where operating parameters were chosen in such a way as to simulate the BOF tapping process as accurately as possible. Samples were analyzed via optical emission spectrometer. Influence of oxygen and sulfur content on vaporization behavior has also been explored. Results show a correlation between absence of sulfur and oxygen from the melt and increase in vaporization rate of copper. Furthermore, possible secondary vaporization and segregation of copper in the mold have been investigated. Results are promising and warrant further investigation.

Introduction

Steel is currently the most produced metallic material and of vital importance for all branches of modern society. Additionally, it is distinguished by its ability to be easily recyclable. The biggest limiting in the recycling of steel is the occurrence of tramp elements that enter the material flow of steel due to the use of scrap during steelmaking. Of these tramp elements, copper is considered the most problematic. [1] While it is used as an alloying element in certain steel grades, copper content in steel makes the material vulnerable to hot shortness. [2, 3] Furthermore, due to the properties of copper, it can not be removed by conventional means in a modern steel plant, as it is a much less prone to oxidation, as the Gibb's free energy of its reaction with oxygen is higher than that of iron. [4]

Since scrap use is an integral part of both primary (Blast Furnace / Basic Oxygen Furnace – BF / BOF) and secondary (Electric Arc Furnace - EAF) steelmaking, it is imperative that in the face of an ever more increasingly global economy, ways of removal of copper that are viable for bulk applications must be found.

One such approach is the vaporization of copper from a steel melt. This is possible in principle because copper has a higher vapor pressure than iron at steelmaking temperatures and as much, may vaporize readily in an atmosphere of sub-atmospheric pressure. Additionally, vacuum treatment of steel melts is today a common, proven technology in many steel plants, such as Vacuum Degassing (VD) or Vacuum Oxygen Decarburization (VOD). As such it is

conceivable that the necessary equipment for the vaporization of copper may already be designed with certain common components with the mentioned technology, such as vacuum pumps and seals. Furthermore, it would mean no additional process time would be necessary, as the tapping process would not take additional time compared to modern industry standards.

In this paper, it is hypothesized that copper vaporization during the tapping stream of a BOF is especially effective since it would take place at a time where the greatest turbulent flow of hot metal is achieved during the steelmaking process. This is already being taken advantage of today, as systems are in operation that allow the charging of alloying elements or desoxidation agents during the tapping process, since it enhances the mixing of these agents and the hot metal.

Experimental Setup

Experiments were conducted at the Vacuum Induction Melting (VIM) furnace of the Institute of Iron and Steel Technology. This unit was chosen due to it being able to closely approximate tapping conditions of a real BOF, as well as its installed systems for sampling, alloying and thermocouple temperature measurements without affecting the internal atmosphere. Experimental parameters were chosen to reflect real BOF conditions. Target tapping temperature for all samples was set at 1640°C, while the target tapping atmosphere was argon at 100 mbar. This pressure was determined to be closely reflective of currently operational low-pressure metallurgical plants, such as Vacuum Degassing (VD) or Vacuum Oxygen Decarburization (VOD) plants. During the melting phase, the pressure was kept at 100 mbar of argon to prevent premature vaporization of copper as well as the formation of any kind of slag layer.

Armco iron was chosen as the base material for all experiments due to its purity. Additionally, it was sandblasted before the experiments were conducted as to minimize to inclusion of oxygen into the furnace chamber and as such to prevent the formation of a slag layer. This base material was alloyed to a copper content of 0.5%. The target mass of hot metal for all experiments was set at 25 kg. Table 1 shows the measured chemical analysis of non-alloyed Armco iron.

Table 1: Chemical composition of Armco iron

Fe	Cu	S	O	N	C	Si	Mn
99.9	0.0058	0.0035	0	0	0.0116	< 0.0050	0.0212
P	Cr	Mo	Ni	Al	Co	Nb	Ti
< 0.0030	< 0.0030	< 0.0050	< 0.0050	< 0.0010	< 0.0020	< 0.0020	< 0.0010
V	W	n	B	Ca	Zr	As	
< 0.0020	< 0.0150	< 0.0020	< 0.0010	< 0.0001	< 0.0030	< 0.0050	

To mechanically simulate the tapping process, the crucible, after ascertaining that target temperature and composition have been achieved, was turned on its supporting trunnion and tapped into the steel mold. This resulted in a tapping duration of 140 s, which was achieved using the slowest possible angular velocity of the trunnion.

To evaluate the effect that sulfur and oxygen in solution have on the vaporization behavior, four experiments have been conducted with different concentrations of these elements. Iron oxide and iron sulfide, respectively, were used as alloying agents.

To evaluate the vaporized copper, the chemical composition of the resulting steel rod has been analyzed in the following way: Three samples were cut from it on approximately equidistant locations of the rod, as to ascertain that no additional vaporization of still-liquid copper-bearing melt took place in the mold. The samples were designated in the following way: Sample 1 being the baseline iron-copper hot metal before vaporization took place, sample 2 being at the lowermost point of the mold after casting and as such represents the first material that reached the mold and solidified, sample 3 representing the approximate center point of the mold and sample 4 representing the top point of the mold, which was identified as the point where secondary vaporization was the most likely to occur.

For chemical analysis during and after experiments, the optical emission spectrometer at the Institute of Iron and Steel Technology (IEST) was used.

Results

It was originally intended for the first experiment to be used as a baseline to ascertain the vaporization behavior of a binary iron-copper melt, to be compared to samples with additional sulfur and oxygen content. However, it was observed that the oxygen content of the sample rose without charging of oxygen-bearing iron oxide. This could be attributed to the reaction of the melt and the crucible. It indicated that the addition of deoxidizing agents are necessary to evaluate the vaporization behavior of copper in the absence of oxygen.

Regardless of additional oxygen ingress into the melt, experiment 1 showed a reduction of measured copper content across all samples of 0.01 %.

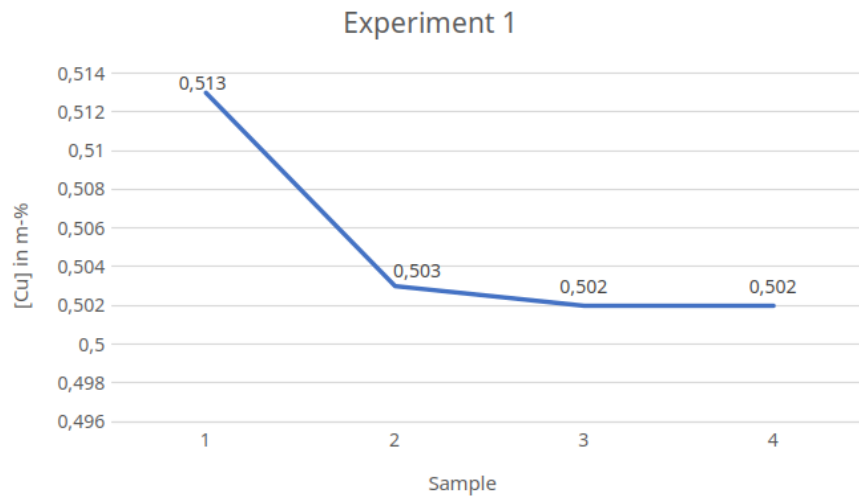


Figure 1: Diagram showing the concentration of copper before and after vaporization took place during experiment 1

The second experiment was intended to evaluate the vaporization behavior of copper in the presence of both sulfur and oxygen in the melt.

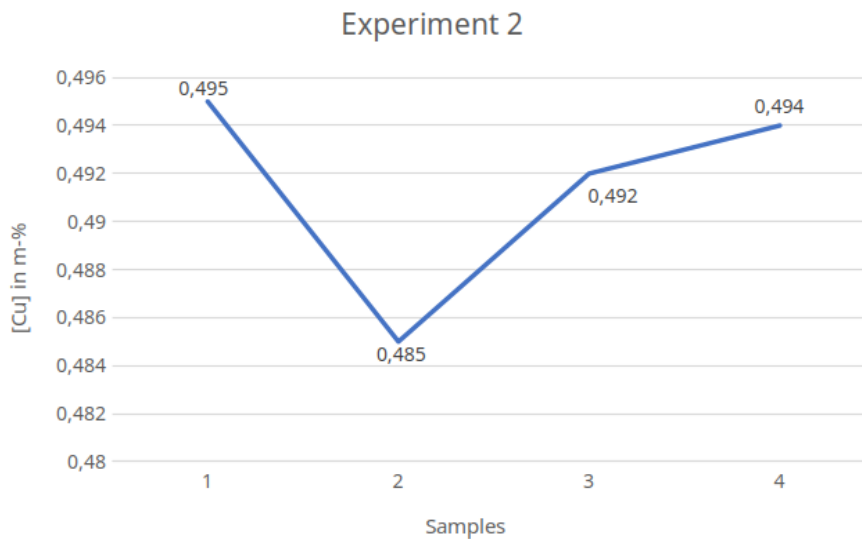


Figure 2: Diagram showing the concentration of copper before and after vaporization took place during experiment 2

It may be observed that a significant segregation of copper has occurred in the mold. This is consistent with the result of experiment 3, where the melt has been deoxidized and sulfur was added.

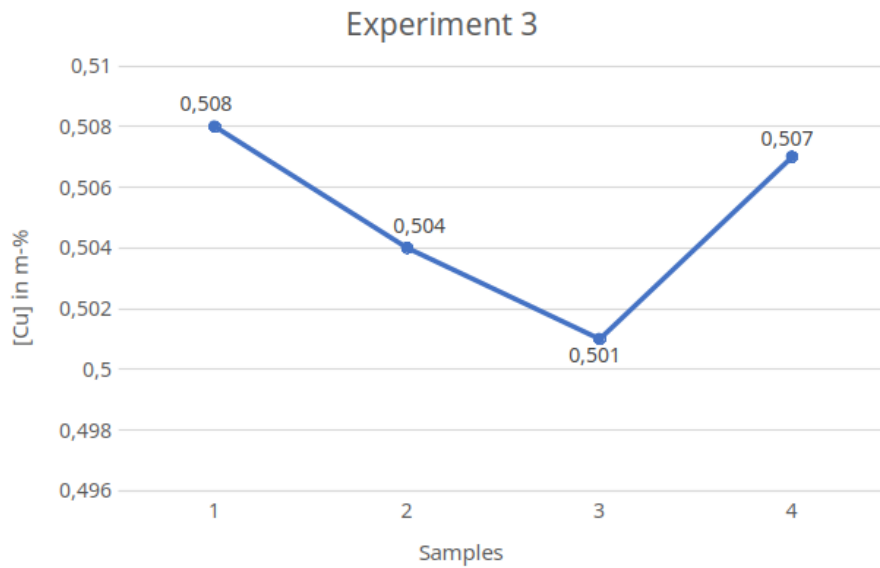


Figure 3: Diagram showing the concentration of copper before and after vaporization took place during experiment 3

Lastly, a last experiment was conducted to compare the effect of vaporization during the tapping stream to that of a stirred melt bath. To facilitate this, the pressure inside the furnace melting chamber was reduced to the target pressure of tapping for the other experiments for the same duration as the tapping would take, and then raised again to 100 mbar. Afterwards, it was tapped at that pressure to prevent any further vaporization. It was observed that the vaporization rate was comparable to the ones observed during the vaporization from the tapping stream.

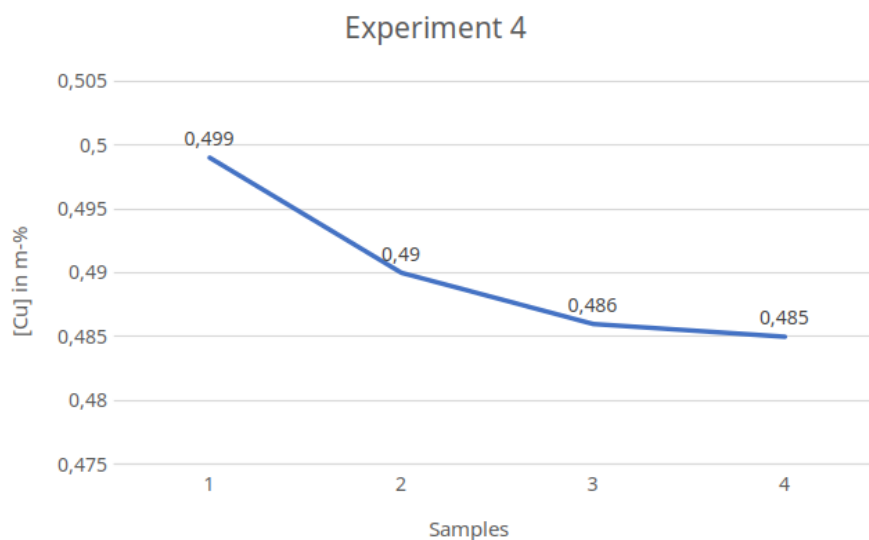


Figure 4: Diagram showing the concentration of copper before and after vaporization took place during experiment 4

Conclusion

Several possible modes of vaporization of copper from steel melts have been investigated. It has been shown that the proposed method of vaporization from the tapping stream is equivalent in efficiency to an inductively stirred melt, with the added benefit of it not requiring additional time in a real-world application. It can generally be ascertained that sulfur content in the melt reduces the vaporization potential of the examined melts. As such, current hot metal desulfurization regimes may be continued if this technology is to be applied to industrial-scale applications.

As such, the efficacy of the proposed process has been proved on a laboratory scale.

However, the observed segregation of copper in the mold with sulfur present in the melt warrant further investigation.

In conclusion, the fundamental usability of this proposed approach appears to be proved, even though certain aspects of the process, such as the copper segregation observed, must be further refined before industrial-scale pilot plants may be commissioned.

References

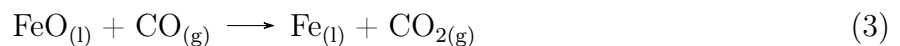
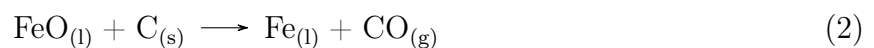
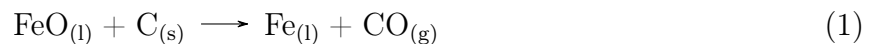
- [1] Environ. Sci. Technol. 2017, 51, 11, 6599–6606.
- [2] Cheng Lu, Wanlin Wang, Jie Zeng, Chenyang Zhu, Sub-rapid solidified high copper-bearing steel with excellent resistance to hot shortness, Scripta Materialia, Volume 239, 2024, 115800, ISSN 1359-6462.
- [3] Durowaye, Stephen. (2014). Effect of Copper on Microstructure and Mechanical Properties of Construction Steel. World Academy of Science, Engineering and Technology International Journal of Chemical, Nuclear, Metallurgical and Materials Engineering. 8. 785-789.
- [4] Ellingham, Harold JT. 'Reducibility of oxides and sulphides in metallurgical processes.' J. Soc. Chem. Ind 63.5 (1944): 125-160.

Examination of the foam behaviour of highly FeO rich EAF slags

Angelini, Alberto¹

¹ TU Bergakademie Freiberg

Slag foaming was mainly used in electric arc furnaces (EAF) to protect the refractory materials from the high energy intensity (radiation) generated by electrodes and to improve the productivity and energy efficiency of this equipment. Nevertheless, the correct control and optimisation of foam production is still limited by some of the main factors: Basicity, viscosity, surface tension, presence of suspended solid particles, FeO content and injection rate of carbon particles and oxygen. The shielding of the light arcs by the foaming slag reduces the energy losses via the water-cooled furnace walls and ceilings and thus enables a significantly improved energy. The foaming of the slag by CO / CO₂ gas bubbles occurs in the EAF process through oxidation of carbon dissolved in the molten steel by oxides in the slag (reaction 1). This foaming process is intensified and maintained by injecting carbon into the slag. The injected carbon can react directly with the iron oxide after reaction 2 or reduce the iron oxide indirectly after reactions 3 and 4 via an intermediate gasification step.



The slags are divided into two groups: acidic oxides and basic oxides and they are SiO₂, MnO or for the acidic fluxes MgO and CaO for the base. In the slag Al₂O₃ can be acidic or basic his behaviour is shown at the viscosity diagram. The creation of the foam came from the balance between the acidic and basic oxides. In this case as Figure 1 shows:

$$B_4 = \frac{\% \text{CaO} + \% \text{MgO}}{\% \text{SiO}_2 + \% \text{Al}_2\text{O}_3} \quad (5)$$

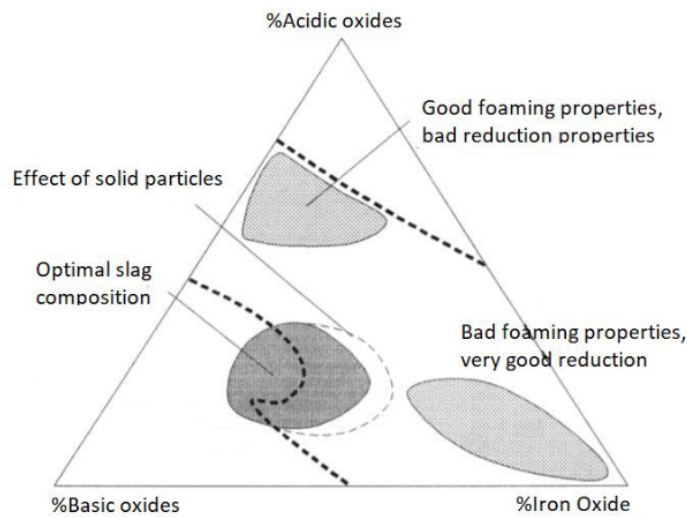


Figure 1: Foam slag zones

A distinction is made between alkaline and acidic slags depending on their reaction behaviour. Basic slags are those whose basicity is > 1.0 and therefore contain an excess of basic oxides. Acidic slags have a basicity < 1.0 .

For my experiments it has been used a slag with an Iron oxide content $> 35\%$ with an acid basicity.

Experiments

Viscosity

The slag is once heated to 1650°C (at a heating rate of $16^{\circ}\text{C}/\text{min}$). The viscosity of the slag is measured with the aid of an immersed dysentery body (made of molybdenum) until the dysentery body is no longer able to rotate. Three measurements are taken in succession (Figure 2), but the three curves have different shapes because the chemical composition of the slag changes with each measurement. The first measurement can be assumed to be the real one. For this reason, a chemical analysis is carried out at the end of the third measurement to show the change in chemical composition after 3 measurements (Table 1).

Table 1: Chemical composition after the third viscosity measurement

Chemische Zusammensetzung in [%]									
CaO	SiO ₂	Fe ₂ O ₃	MgO	Al ₂ O ₃	MnO	Cr ₂ O ₃	P ₂ O ₅	Ti ₂ O	MoO ₃
									9,71

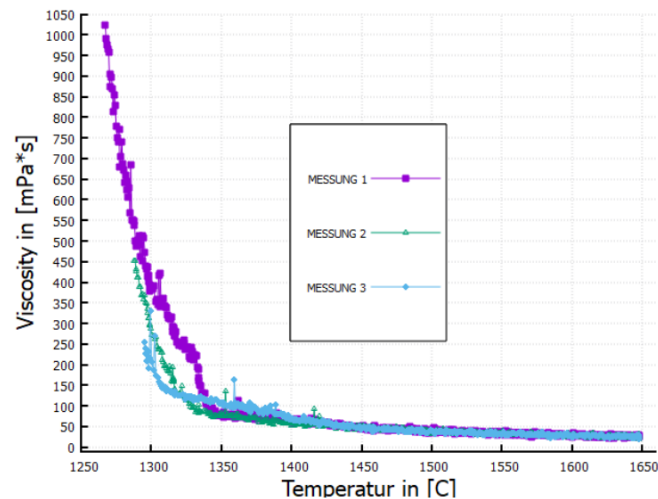


Figure 2: Viscometry of all 3 measurements

Compared to the chemical composition at the beginning of the experiment, it consists of only two thirds Fe_2O_3 , CaO has increased as well as SiO_2 , Cr_2O_3 , P_2O_5 , MgO, MnO and TiO_2 slightly, whereas the proportion of Al_2O_3 and Cr_2O_3 has decreased significantly. The biggest factor is that in the end the chemical composition has over 9% MoO_3 , which was not the case at the beginning. This means that the release of Mo from the crucible should not be underestimated, and the curve can no longer be taken into account in the second measurement. The figure also shows how the 3 curves change: When cooling in ‘Messung 1’ to 1330 °C, there is a ‘kink’ due to the formation with a high probability of Mo spinels because of the change in the chemical composition already in ‘Messung 2’ the curve solidifies beforehand. This can also be seen in ‘Messung 3’, where the solidification point is even lower due to the increase in MoO_3 in the slag with each measurement. For this reason, only ‘Messung 1’ is examined and analysed.

Density & Surface tension

Similar to the preparation for the viscosity measurement, in a molybdenum crucible filled first with 20 g of slag, always at 16 °C/min up to 1650 °C. When the crucible was cold, it was transferred to the MBP (Maximum Bubble Pression) system. There the Molybdenum crucible is placed in a carbon crucible with a very wide wall diameter and covered with a carbon lid (on the surface a small hole for the passage of the capillary the same capillary was used for the MFG40) and inserted into the furnace at the MBP plant. Figure 3 shows when the temperature reaches 1650 °C, the capillary is immersed in the melt and a gas bubble of argon is forced through the capillary into the liquid under investigation and the maximum internal bubble pressure is used as a measure of the surface tension.

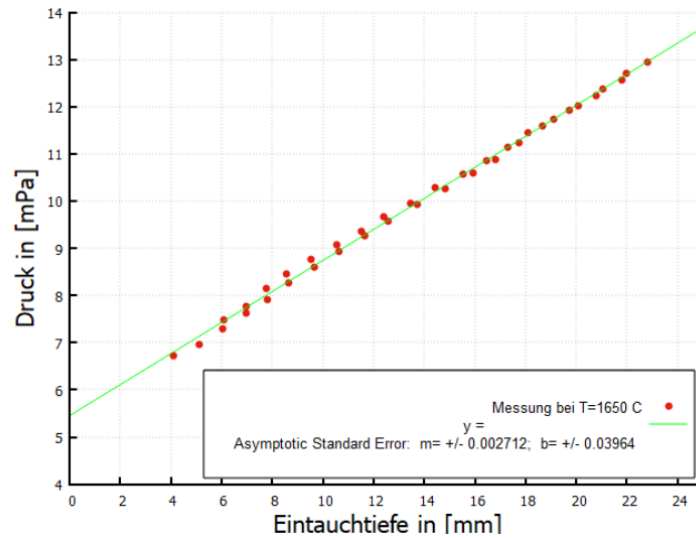


Figure 3: Surface tension measurement through pression

Measuring the bubble diameter

With a specific software, I could determine the diameter of the bubble during the maximal height of the foam in the Figure 4:

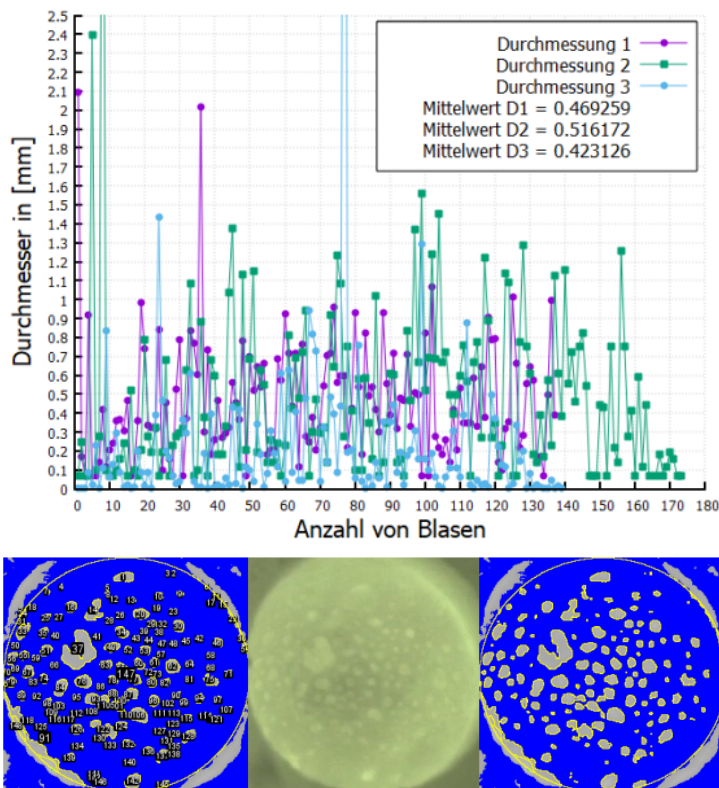


Figure 4: Diameter of the foam bubbles on different frames, mean values in [mm]

Foam slag Height

In Figure 5 for ‘untreated polymers’ (Nicht behandelte Polymere) the polymers are used directly without prior processing, we speak of polymers of different shapes, most of them spindle-shaped with very different sizes, colours and lengths. Because of the different shapes of the polymers, there was also the difficulty of filling the steel box. But the biggest challenge is to estimate the chemical composition of the input plastics due to the heterogeneity of the material. In contrast to ‘treated polymers’ (Behandelte Polymere), polymers are used with a relatively very homogeneous size (significantly longer than wider), colour and length. Mixed polymers are separated with water and only those with a density lower than that of water (PE/PP) are used. The practical method of separating polymers by means of liquid also resulted in some problems due to the very small differences in density compared to the total polymers. Of course, the production of processed feedstocks requires additional labour, as shown in the figure, to perform a good foam study. The height is measured using a caliper positioned at the opening of the crucible, the depth gauge is immersed to the height of the remaining foam slag. The value is read off a scale with millimetre graduations, the so-called Vernier scale is located on the slide, which makes the values very accurate.

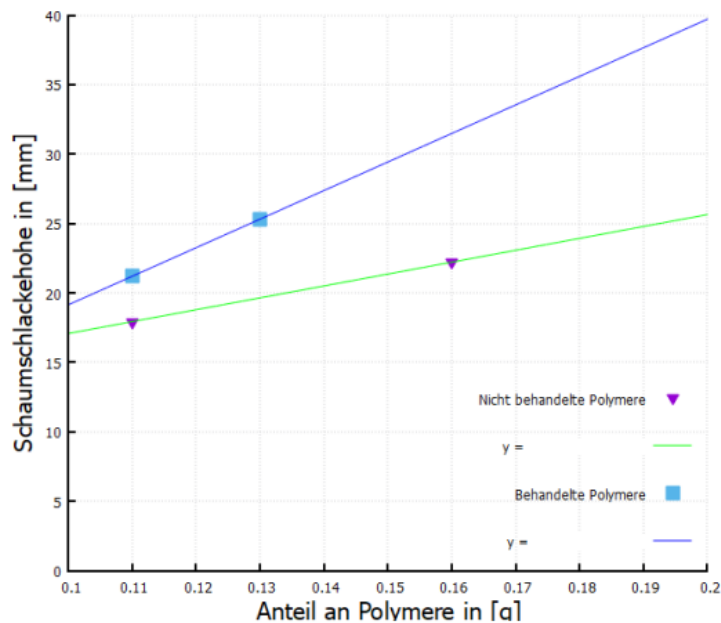


Figure 5: Achieved height during foaming

Foam index calculation

Having all the parameter I need I for the calculation of the slag foam index I used the formulas

$$\Sigma_{th} = \frac{H}{V_g * \Phi} = \frac{0.025 \text{ m}}{0.057684836 \text{ m/s} * 0.9069} = 4.8371 \text{ s} \quad (6)$$

$$\Sigma_{basic} = 115 * \frac{\sigma^{1.2}}{\mu^{0.2} * \rho * D_b^{0.9}} = \frac{0.3046^{1.2} \text{ N/m}}{0.028428^{0.2} \text{ Pa s} * 3352.081 \text{ kg/m}^3 * 0.0014^{0.9} \text{ m}} = 6.2172 \text{ s} \quad (7)$$

where:

σ – surface tension

ρ – density

H – height of the foam

D_b – average bubble diameter

V_g – volume gas flow

Φ – volumetric proportion of the gas

μ – viscosity

The values Σ_{basic} [Observed Foam Index] reflect reality and are very close to the value of $\Sigma_{th} = 4.8371 \text{ s}$ [Predicted Foam Index] and as is can be seen in Figure 6 the measured values fall within the values of Zhang and Freuhan:

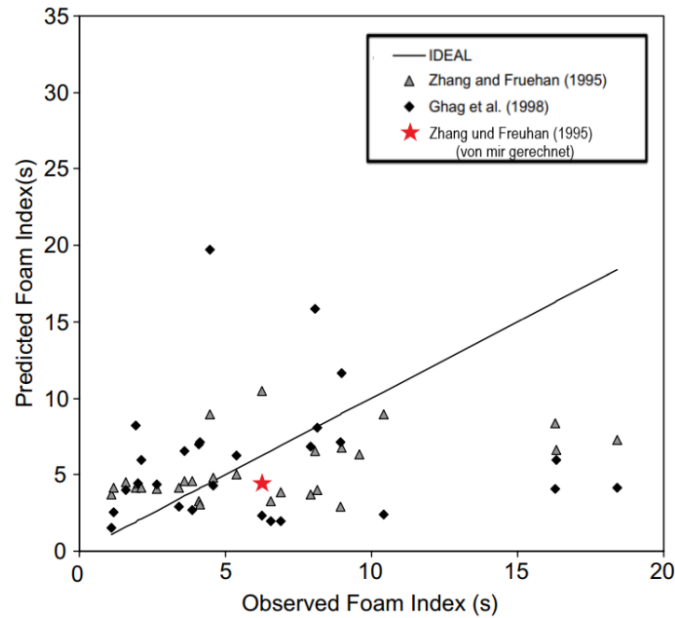


Figure 6: Achieved height during foaming

Hot deformation behaviour of Inconel 718 superalloy by SLM 3D-printing

Marek Benč^{1*}

¹ Faculty of Materials Science and Technology, VSB–Technical University of Ostrava, 17. listopadu 2172/15, 70800 Ostrava–Poruba, Czech Republic

* Corresponding author: marek.benc@vsb.cz

The purpose of this research was to examine the deformation behaviour of a 3D-printed workpiece from the Inconel 718 superalloy. The 3D printed samples were produced using the selective laser melting SLM method when the metal powder is gradually melting with using a powerful laser. The SLM samples were subjected to uniaxial hot compression tests at the temperature range of 900–1200 °C and, combined with a strain rate range of 0.1–10 s⁻¹. The experimental data obtained revealed a minimal and maximal flow stress level of 98 MPa and 683 MPa as for the combination of 1200 °C–0.1 s⁻¹ and 900 °C–10 s⁻¹, respectively. Visual observation and hardness measurements confirmed that higher strain rates and lower temperatures result in greater strain hardening of the material, which can reduce or eliminate the disadvantages of 3D printing technology. The sample tested at a deformation temperature of 900 °C with a combined strain rate of 10 s⁻¹ exhibited the highest microhardness value of 410 HV.

1. Introduction

Inconel 718 is a nickel-based superalloy with high nickel content (around 50%), as well as significant amounts of cobalt, chromium, molybdenum, niobium, and titanium. The alloy has a wide range of applications in various industries, particularly in aerospace, chemical processing, nuclear engineering, and marine engineering due to its excellent mechanical properties, including resistance to high-temperature corrosion, oxidation, and creep strength [1, 2].

The SLM (Selective Laser Melting) process is a widely adopted additive manufacturing technique that involves selectively melting metal powder using a laser to build up complex 3D structures layer by layer. The primary benefit of 3D printing is its capability to produce dimensionally complex products that are difficult or impossible to manufacture using conventional methods. However, 3D printed materials do have some disadvantages, including surface roughness, internal porosity and voids, inhomogeneous distribution of residual stress, and limited product size [3, 4].

Combining 3D printing with post-processing through thermomechanical treatment involving severe plastic deformation (SPD) methods, such as equal channel angular pressing (ECAP) and its modifications, particularly the continuous method of ECAP-Conform, as well as the intensive plastic deformation method of rotary swaging (RS), is a possible way to improve the properties and performance of 3D printed materials. RS is primarily used in the automotive

industry. Similar to SPD methods, this technique induces a mainly compressive stress state, resulting in the homogenization of residual stress [5, 6].

The aim of the research is explored the effects of various processing conditions on the deformation behaviour and gain how the material responds to different of deformation temperature and strain rate levels. Understanding the deformation behaviour of additively manufactured materials is crucial for identifying suitable processing conditions that can enhance their performance and eliminate any defects that may arise during the printing process. By optimising the post-process thermomechanical treatment, it is possible to improve the mechanical properties of the printed components, such as their strength, ductility, and fatigue resistance. The 3D-printed Inconel 718 were subjected to uniaxial hot compression tests, followed by visual inspection and evaluation of the flow stress obtained under different thermomechanical conditions, and finally microhardness measurements were performed.

2. Metal 3D printing and hot compression test

The samples of Inconel 718 for experiment were built using the selective laser melting (SLM) method (see Figure 1a) The powder about size of 15 to 44 μm was melted with a laser a power of 200 W in an inert argon atmosphere using AM400 3D printer. Chemical composition of the Inconel powder is presented in Table 1. The printed samples were printing with the vertical direction from left to right using the stripes printing strategy and processed into 12 cylindrical hot compression specimens of 10 mm diameter and 15 mm length (see Figure 1b). The printed samples were surface machined to the required roughness. The prepared specimens were then subjected to a series of 12 uniaxial hot compression tests using a Gleeble 3800 thermo-mechanical simulator in conjunction in connection with the Hydrawedge II Mobile Conversion Unit (see Figure 1c). Tests were carried out at four deformation temperatures (900, 1000, 1100 and 1200 $^{\circ}\text{C}$) combined with four strain rates (0.1, 1, 10 s^{-1}).

Table 1: Chemical composition of the power Inconel 718 used for SLM.

Element	Cr	Mo	Fe	Nb	Co	Cu	Mn	Si	Al	Ti	C	Ni
Wt. %	20.0– 23.0	8.0– 10.0	5.0	3.15– 4.15	1.0	0.5	0.5	0.5	0.4	0.4	0.1	Balance

2.1 Microhardness analysis

Microhardness was measured on a cross section of the specimen in the direction of the compression. The microhardness was measured at a distance of 1 mm with a load of 0.3 kg on an FM-ARS 900 Automatic microhardness testing system equipment.

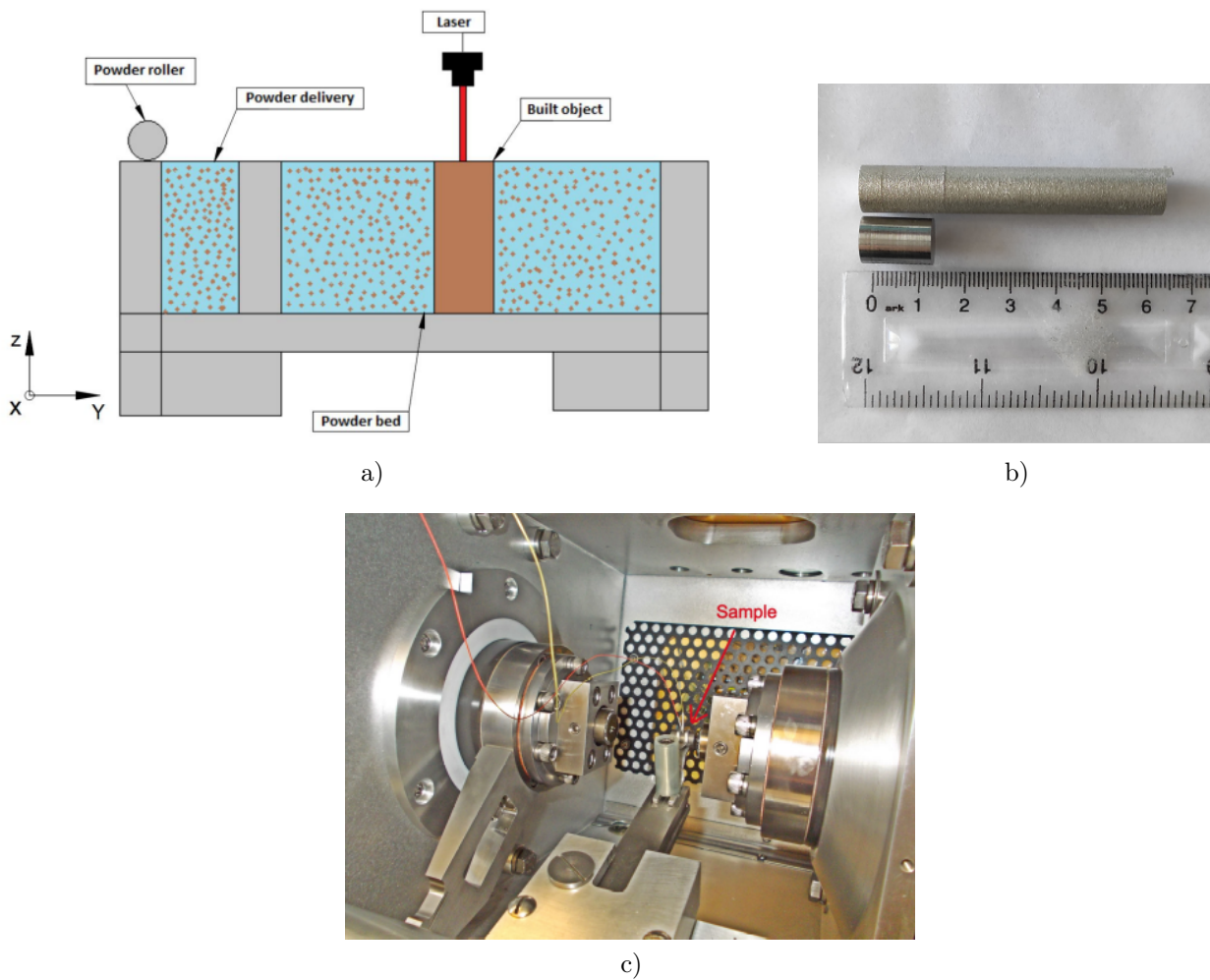


Figure 1: a) Schematic of the SLM process b) Printed sample c) The testing chamber.

3. Results and discussion

3.1 Hot deformation behavior

The results of the compression tests showed that under certain thermomechanical conditions, deformation led to the formation of cracks on the circumferences of the samples. Table 2 summarizes the occurrence of these cracks and evaluates their size and visual documentation are shown in Figure 2. As can be seen the crack size increases with increasing deformation temperature. The influence of strain rate is comparable. Higher deformation rates at lower deformation temperatures allow crack-free surfaces to be achieved. Since the 3D-printed superalloy will undergo rotary swaging with higher levels of deformation, it is likely that this technology will reduce or eliminate the defects of 3D printing technologies.



Figure 2: a) Schematic of the SLM process b) Printed sample c) The testing chamber.

Table 2: The cracks size on the sample circumference.

$\dot{\epsilon}$ (s ⁻¹) / T (°C)	900	1000	1100	1200
0.1	no cracks	no cracks	no cracks	small cracks
1	no cracks	no cracks	no cracks	large cracks
10	no cracks	no cracks	no cracks	large cracks

The data obtained from the hot compression test provided 12 flow curves covering the evolution of material flow stress over a wide range of thermo-mechanical conditions, see Figure 3. It can be seen from the figure that the flow stress curves show the expected trends. In other words, the flow stress increases with decreasing temperatures and increasing strain rates. The maximum acquired flow stress level was ~ 683 MPa (sample deformed at 900 °C and 10 s⁻¹).

3.2 Microhardness

The results of the microhardness measurements are shown in Figure 4. The plot shows that microhardness increases with decreasing deformation temperature and increasing deformation rate. The samples deformed at 1200 °C exhibited comparable microhardness values, with an average of approximately 250 HV0.3. The samples deformed at a lower temperature of 900 °C had an average microhardness value of approximately 350 HV0.3. The effect of strain rate had the opposite effect on the microhardness values as the microhardness increased with increasing strain rate. The sample deformed at 900 °C and a strain rate of 10 s⁻¹ exhibited the highest microhardness of 410 HV0.3. Compared to the results of flow stress analysis, we can conclude that lower deformation temperatures and higher strain rates result lead to softening process and work hardening.

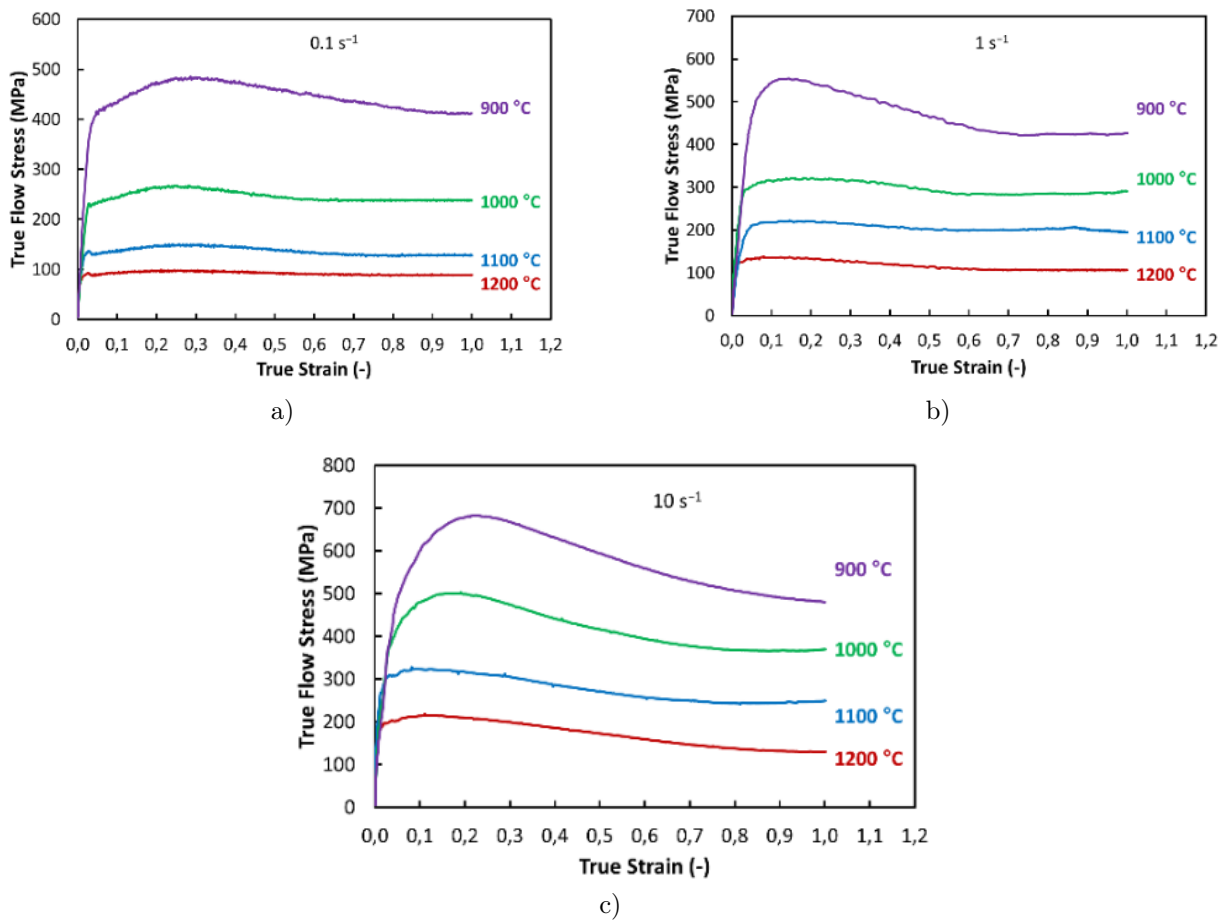


Figure 3: Courses of flow stress for four strain rates and each temperatures (a) strain rate of 0.1 s⁻¹ (b) strain rate of 1 s⁻¹ (c) strain rate of 10 s⁻¹.

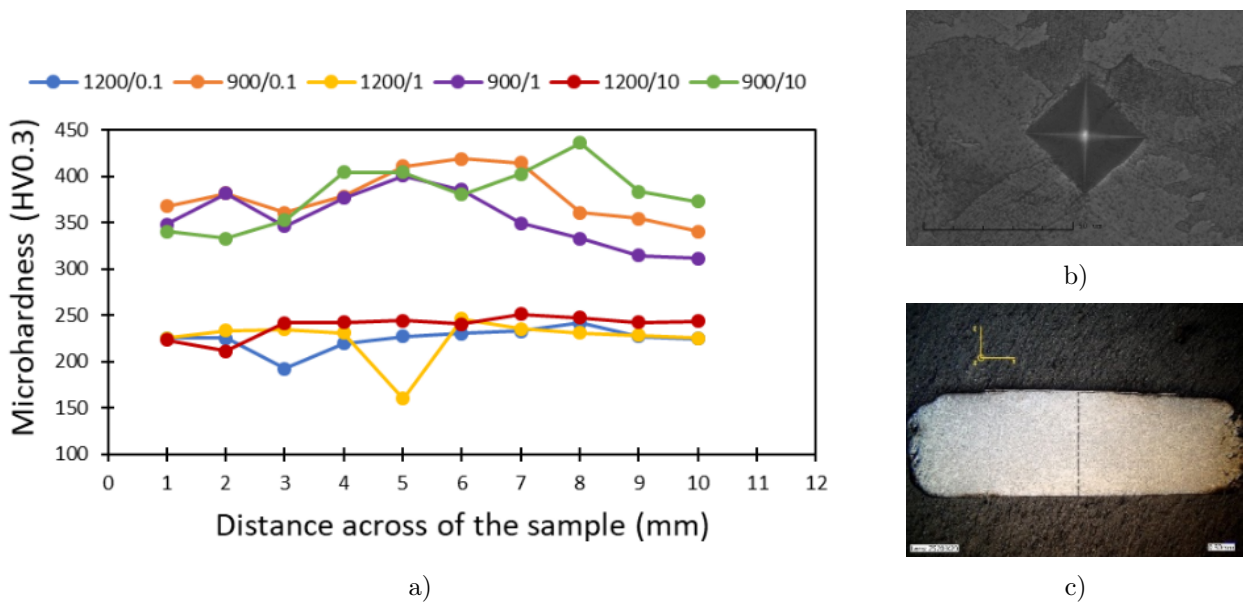


Figure 4: Progress of Vickers microhardness measurement b) indent c) line of the measuring.

4. Conclusion

The submitted research evaluates the hot deformation behavior of the 3D-printed workpiece of the Inconel 718. The results showed the presumed trend in flow stress, i.e. the lower the temperature, the higher the flow stress and the opposite in the case of strain rate influence. The maximal flow stress level is around 683 MPa as for the case of 900 °C and 10 s⁻¹. The visual evaluation of the hot-compression-test samples after deformation then revealed a crack occurring on the sample circumference. With respect to this phenomenon, It can be concluded that lower temperatures result in larger crack sizes. The results of the microhardness measurements showed that microhardness increases with decreasing deformation temperature and increasing deformation rate. The highest microhardness of 410 HV0.3 was obtained from the sample deformed at a temperature of 900 °C and a strain rate of 10 s⁻¹. Comparison of 3D printed Inconel 718 with conventionally produced alloy will be the focus of future studies.

5. Acknowledgment

This work was made with the financial support of the ‘Student Grant Competition’ projects ‘Research and development of unconventional methods for the preparation of progressive materials and their processing’ SP2024/089.

6. References

- [1] BUSCHOW, K. H. J. Encyclopedia of materials: science and technology. Vol. 10, T-Z. Amsterdam; London: Elsevier, 2001, viii, s. 9081-9913 : il. ISBN 0-08-043152-6.
- [2] HOSSEINI, Ehsan, V. POPOVICH. A review of mechanical properties of additively manufactured Inconel 718, Additive Manufacturing, 2019,30,100877.
- [3] Zhang, Dongyun, Pudan Zhang, Zhen Liu, Zhe Feng, Chengjie Wang, Yanwu Guo, Thermofluid field of molten pool and its effects during selective laser melting (SLM) of Inconel 718 alloy. Additive Manufacturing. 2018, 21, 567-578.
- [4] Richter J., Vollmer M., Bartzsch G., Scherbring S., Volkova O., Mola J., Niendorf T. Novel austenitic Cr-Mn-Ni TWIP-steel with superior strength enabled by laser powder bed fusion—On the role of substrate temperatures. Addit. Manuf. Lett. 2022;3:100065. doi: 10.1016/j.addlet.2022.100065.
- [5] Kunčická, L, Radim, Kocich, Gergely, Németh, Karel, Dvořák, Marek, Pagač. Effect of post process shear straining on structure and mechanical properties of 316 L stainless steel manufactured via powder bed fusion. Additive Manufacturing, 2022, 59, 103128.

- [6] Opěla, Petr, Marek Benč, Stepan Kolomy, Zdeněk Jakůbek a Denisa Beranová. High Cycle Fatigue Behaviour of 316L Stainless Steel Produced via Selective Laser Melting Method and Post Processed by Hot Rotary Swaging. *Materials* [online]. Switzerland: MDPI AG, 2023, 16(9), 3400 [cit. 2023-05-22]. ISSN 1996-1944. Dostupné z: doi:10.3390/ma16093400.

CFD analysis of steel flow in the five-strand tundish at different casting speeds

Jiří Cupek^{1*}, Josef Walek¹, Markéta Tkadlečková²

¹ Department of Metallurgical Technologies, Faculty of Materials Science and Technology, VSB – Technical University of Ostrava, 17. listopadu 2172/15, 70800 Ostrava, Czech Republic

² TŘINECKÉ ŽELEZÁRNY, a.s., Průmyslová 1000, Staré Město, 73961 Třinec, Czech Republic

* Correspondence: jiri.cupek@vsb.cz

This paper presents a research focused on the optimization of the steel flow in the tundish during the continuous casting process. The tundish is one of the most important technological parts of the casting machine. It primarily provides supplying steel during ladle change and steel distribution between casting strands. The tundish is the last reactor in which it is possible to influence the final quality and purity of the cast steel. A key element of this study is the use of numerical simulations to compare two turbulence models, namely k-epsilon and k-omega, at variable steel casting speeds. Simulations were performed in the software ANSYS Fluent, examining a total of six different variants with combinations of turbulence models and casting speeds. The aim of this paper is to gain a deeper understanding of the character of the steel flow and its effect on the quality of the resulting steel under different process conditions. Numerical results were interpreted in schemes of the model. These schemes included the analysis of velocity vectors in different planes, the temperature distribution on the surface of the tundish, and the monitoring of the tundish walls wear.

1. Introduction

The tundish is the last reactor in which it is still possible to influence the final quality and purity of the cast steel. For this reason, emphasis is placed on the study of events in the tundish. The tundish ensures the stability of the casting process, primarily fulfils the function of a reservoir of liquid steel during the exchange of casting ladles during sequential casting and distributes the flow of steel between individual casting strands [1–3].

The tundish consists of a steel shell with a heat-resistant lining. The tundish is placed between the ladle and the molds. To minimize heat loss, remove non-metallic inclusions and ensure the ideal course of chemical reactions, the level of the melt in the tundish is covered with slag. To control the flow of steel from the tundish to the molds, the individual casting strands are equipped with stopper rods or slide gate system [3–5].

Optimum steel flow during continuous casting is essential in the tundish. A number of elements can be constructed in the tundish that affect the resulting flow of steel. The flow can be modified by the use of impact pads, dams or weirs, baffles, or the use of a porous block for argon blowing [3–8].

The so-called retention time is related to the flow of steel in the tundish, which determines the time spent by a certain element of the melt in the tundish. In order to ensure the desired course of removal of non-metallic inclusions, to support chemical reactions and to achieve a homogeneous melt, it is necessary to maximize the retention time and, in the case of multi-strand casting, to maintain the lowest possible dispersion of retention times on individual casting strands [6–8].

The flow of steel in the tundish can be divided into active and passive. In the case of active flow, this is the area of the so-called active volume, which can be divided into a well-mixed volume and a plug flow volume. The well-mixed volume is characterized by turbulent flow and occurs mainly in the inlet area. The plug flow volume is characterized by slow directed laminar motion and its occurrence in the intermediate basin is essential. In the case of passive flow, this is the so-called dead volume. The dead volume is characterized as an ineffective area of the tundish where the flow is substantially slowed down. The flow of steel in the dead volume area reaches at least twice the value of the mean retention time [1, 2, 8].

The location of the five-strand tundish between the ladle and the molds is shown in Figure 1.

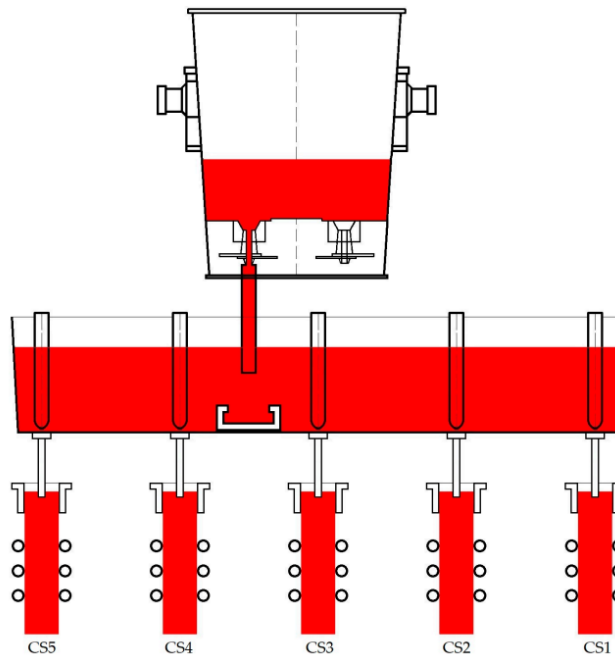


Figure 1: Five-strand tundish [1]

2. Principle of numerical modelling

In the case of numerical modelling, the numerical model is described using a system of partial differential equations that solve, for example, the flow of liquids and gases, heat sharing or chemical reactions in the model [2].

The partial differential equations are solved on a computational mesh that covers the constructed geometry. Partial differential equations are then solved in each individual cell of the computational mesh separately. The accuracy of the calculation is determined by the fineness of the calculation mesh and the calculation method. Basic numerical methods include finite difference method (FDM), finite element method (FEM) and finite volume method (FVM) [2].

Finite difference method (FDM) – the essence is the conversion of the investigated system to a system of differential equations and the subsequent solution within certain limits. The limits are set by the boundary and initial conditions of the model. The solved area is covered by a mesh with a finite number of non-overlapping elements. Derivatives at nodal points are replaced by differences. The differential equations are further adjusted to a system of algebraic equations and then solved numerically using a system of iterations [8–10].

Finite element method (FEM) – is the most important among the numerical methods. It is used especially when solving tasks in the area of temperature fields and in the area of flexibility and strength. The essence consists in the division into a mesh of elements of a finite number, which can also be unstructured. A two-dimensional mesh is most often divided into triangular or quadrilateral elements, in the case of a three-dimensional division, it is most often tetrahedrons, pentahedral or cuboids. The solution on each element takes the form of a quadratic polynomial or linear function [8–10].

Finite volume method (FVM) – when calculating with the finite volume method, the object is first divided into a certain number of non-overlapping finite volumes. The method across the volume of the computational cell calculates the values of the variables and directly discretizes the integral equation, which is subsequently solved in the general form. The calculation usually takes place at one point that characterizes the given final volume. The representative point is located in the centre of the finite volume and contains information about the values of scalar quantities and velocity components [8–10].

3. Experimental conditions

Ansys software package was used for numerical simulations and their preparation. Ansys software package was used for numerical simulations and their preparation. The DesignModeler software was used to create the geometry, followed by meshing in Ansys Mesh and flow simulations in Ansys Fluent. Software version 19.2 was used for the simulations.

3.1 Geometry

For numerical simulations, only the inner part of the tundish was constructed. The created geometry of the tundish is schematically shown in Figure 2.

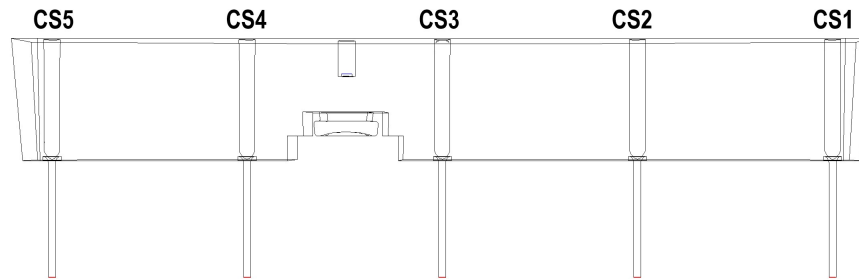


Figure 2: Geometry of the five-strand tundish

For numerical simulations, 2 configurations of computing mesh were used. The CutCell computational network proved to be optimal, as it had higher orthogonal quality and lower skewness than tetrahedral mesh. The parameters of the mesh are shown in Table 1. The schematically displayed meshes are shown in Figure 3.

Table 1: Configurations of computing mesh

Computing mesh	Number of nodes	Number of cells	Orthogonal Quality	Skewness
Tetrahedral	248 977	1 331 930	0.7824	0.2162
CutCell	735 713	680 460	0.9827	0.0243

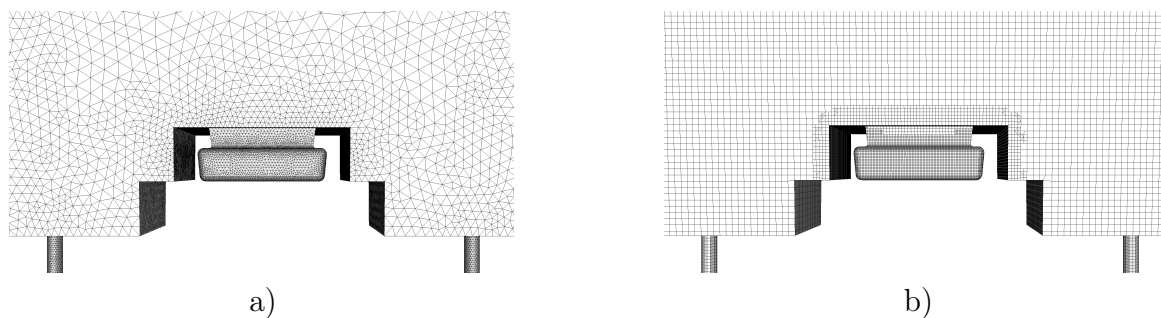


Figure 3: Computing meshes: a) Tetrahedral; b) CutCell method

For the calculation, it was necessary to define the boundary conditions of the simulation. The boundary conditions used for the simulations are shown in Table 2.

The simulations were performed using the k-epsilon and k-omega turbulence models. In addition, the variants differed in casting speed, which is determined by the mass flow rate of the steel. Variants of the simulations are shown in Table 3.

Table 2: Boundary conditions of model setting

Parameter	Value
Casting speed – Mass flow rate (kg s^{-1})	39.7; 46.32; 52.93
Casting temperature (K)	1773.15
Gravity (m s^{-2})	-9.81
Operating pressure (Pa)	101 325
Heat flux of free surface (W m^{-2})	13 000
Heat flux of tundish walls (W m^{-2})	2000

Table 3: Boundary conditions of model setting

Model variant	Turbulent model	Mass flow rate (kg s^{-1})
V1	k-epsilon	39.70
V2	k-epsilon	46.32
V3	k-epsilon	52.93
V4	k-omega	39.70
V5	k-omega	46.32
V6	k-omega	52.93

4. Results and discussion

Figure 4 shows a comparison of the velocity vectors of all simulation variants. It can be seen that a higher casting speed leads to higher turbulence at the tundish surface, which can cause oxidation of the surface and entrainment of undesirable inclusions into the casting strands. These turbulences are evident by comparing variant V1 with variant V2 and also by comparing variant V4 with variants V5 and V6. In the V3 variant, large turbulence and irregular flow are visible, which could have been caused by a calculation error. From the point of view of the turbulence model, by comparing variants V1, V2 (k-epsilon) with variants V4, V5, V6 (k-omega), it can be seen that in the k-epsilon model the flow after hitting the impact pad is directed more towards to the surface, while in k-omega is directed more towards the volume of the tundish. In this case, the k-epsilon flow more closely corresponds to the real flow, which was described, for example, in the paper [1].

A simulation of the wear prediction of the refractory lining was performed (Figure 5). It is evident that a higher casting speed, i.e. comparing variant V1 with variant V2 and comparing variant V4 with variant V5 leads to higher wear in the upper and lower areas of the tundish. In the case of the turbulence model. The results for k-epsilon (V1, V2) and k-omega (V4, V5) are very similar. The K-epsilon model achieves smoother results and the results are closer to the operational state of the real device.

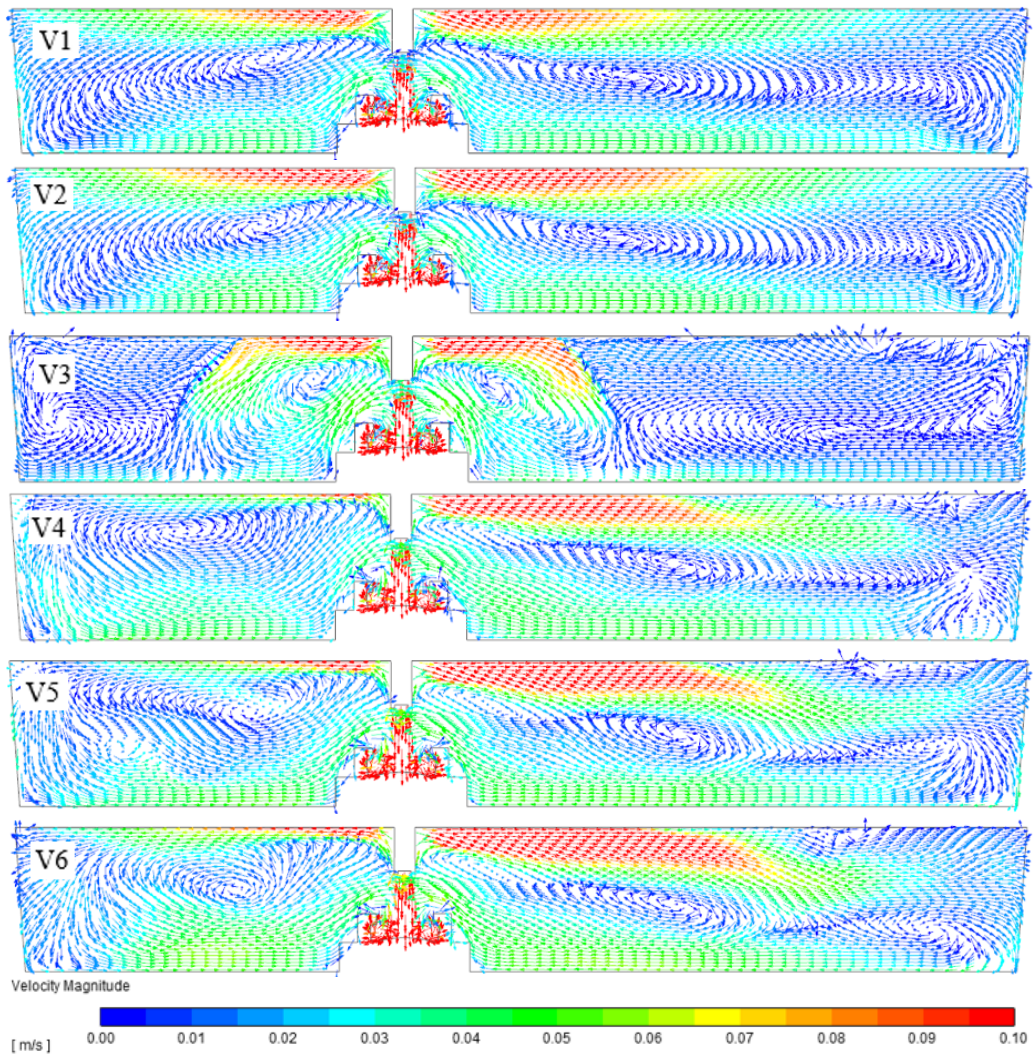


Figure 4: Flow vectors in the shield tube section for all variants.

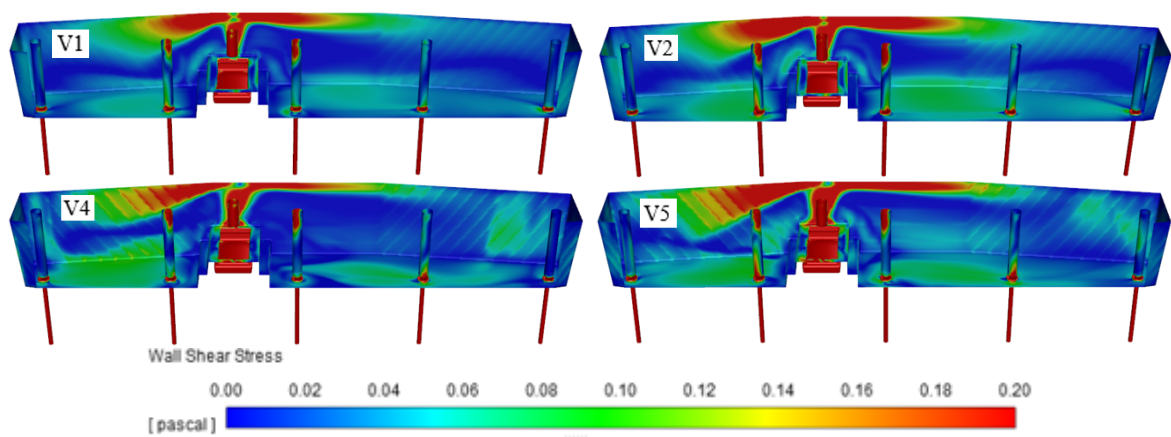


Figure 5: Flow vectors in the shield tube section for all variants.

Conclusion

In the paper, 6 variants of steel flow in the tundish were compared. Different casting rates and turbulence models were compared. Reviews of velocity vectors in different planes, reviews of temperature distribution on the surface of the tundish, and overviews of wear on the walls of the tundish were monitored. It has been proven that a higher casting speed leads to a higher oxidation of the steel, a greater amount of entrainment of inclusions into the casting strands and above all to a higher wear of the lining. From the point of view of the turbulence model, the k-epsilon model is significantly closer to the flow in a real system. There are smoother transitions in the wear of the lining and the places of wear correspond to reality. The k-epsilon model proved to be optimal for monitoring events in the tundish.

Acknowledgements

The work was created within the solution of the Student Grant Competition of number SP2024/089. This paper has been elaborated in the framework of the grant programme 'Support for Science and Research in the Moravia-Silesia Region 2022' (RRC/12/2022), financed from the budget of the Moravian-Silesian Region.

References

- [1] WALEK, J., TKADLEČKOVÁ, M., VELIČKA, M., MACHŮ, M., CUPEK, J., HUCZALA, T., CIBULKA, J., RŮŽIČKA, J., MICHALEK, K. Physical Experiments and Numerical Simulations of the Influence of Turbulence Inhibitors and the Position of Ladle Shroud on the Steel Flow in an Asymmetric Five-Strand Tundish. *Metals*. 2023, 13(11). ISSN 2075-4701. Available from (DOI): <https://doi.org/10.3390/met13111821>.
- [2] MICHALEK, K. Využití fyzikálního a numerického modelování pro optimalizaci metalurgických procesů. Ostrava: VŠB-TU Ostrava, 2001, ISBN 80-7078-861-5.
- [3] LOUHENKILPI, S. Continuous Casting of steel. *Treatise on Process Metallurgy*. 2014, 3, 373-434. ISBN 978-0-08-096988-6.
- [4] ZHANG, J., YANG, S., LI, J., TANG, H., JIANG, Z. The Effect of a Dissipative Ladle Shroud on Mixing in Tundish: Mathematical and Experimental Modelling. *High Temperature Materials and Processes* [online]. 2018, 37(1), 25-32. Available from (DOI): <http://doi.org/10.1515/htmp-2016-0093>.

- [5] SUJATA, D., RAJEEV, K. S., AMITAVA, P. Role of Tundish Argon Diffuser in Steel-making Tundish to Improve Inclusion Flotation with CFD and Water Modelling Studies. *International Journal of Engineering Research and Technology* [online]. 2015, 4(8), 213-218. Available from (DOI): <http://doi.org/10.17577/IJERTV4IS080223>. ISSN 2278-0181.
- [6] HARNSIHACACHA, A, PIYAPANEEKOON, A, WATTANAPORN, Ch. Flow prediction in the multi-strand continuous casting tundish of Millcon Steel PLC. *Materials Today: Proceedings*. 2018, 5(3), 9229-9237. ISSN 2214-7853.
- [7] CUPEK, J., PIEPRZYCA, J., WALEK, J., SATERNUS, M., TKADLEČKOVÁ, M., MERDER T. Optimization of the Steel Flow in the Two-Strand Tundish Using Different Geometry of Impact Pad. *Journal Metalurgija*. 2023, 62(2). ISSN 0543-5846.
- [8] ZHANG, H., FANG, Q., LIU, Ch. Effect of flow control devices on grade change process in a five-strand Tundish. *Metallurgical research and Technology* [online]. 2022, 119(3). Available from (DOI): <https://doi.org/10.1051/metal/2022039>.
- [9] KOZUBKOVÁ, M. Modelování proudění tekutin FLUENT, CFX. Ostrava, 2008. Vysoká škola báňská - Technická univerzita Ostrava.
- [10] Ansys Fluent ver. 19.2 – user’s guide, Canonsburg, USA 2022.

Wir bieten:

Praktika für Studenten
und Diplomarbeiten

Interessant & praxisnah



Agosi – Ihr Partner für Edelmetall

Overview about wear and plastic deformation of MP159 alloy

Djimaoui Nour El Imane¹, V. Mertinger¹, Y.Adonyi²

¹ University of Miskolc, Institute of Physical Metallurgy, Metal forming and Nanotechnology

² Welding Technology Center, University West, Sweden

Introduction

Friction Stir Welding (FSW) is a solid-state welding process used to join materials, particularly metals. It was invented and developed in 1990 by The Welding Institute (TWI). FSW is a highly efficient and innovative technique that offers several advantages over traditional welding methods.

FSW involves the joining of materials using a specially designed tool. This tool consists of a cylindrical shoulder and a non-consumable pin. The process begins by placing the rotating tool on the joint line between the two materials to be welded. The tool is then plunged into the workpieces, generating frictional heat, and plasticizing the material. The combination of heat and mechanical action causes the material to soften and mix, creating a solid-state weld without melting the materials.

One critical aspect of FSW is tool wear. The FSW tool is subjected to high temperatures, friction, and mechanical stresses during welding, leading to wear and degradation over time. Tool wear affects the quality and efficiency of the welding process and must be carefully monitored and managed.

MP159 material

MP159 alloy is a cobalt-based superalloy, which possesses a good combination property of ultra-high strength, ductility, corrosion resistance, and low thermal conductivity. The MP159 Superalloy is a Co–Ni–Cr-based multiphase superalloy and is usually applied in aerospace as a bolting workpiece produced by hot upset processes [1].

Mechanisms of wear

Wear has been defined as the progressive loss of material from rubbing surfaces. A broad classification of the main wear mechanisms is shown below, and each of these mechanisms results in material removal (Figure 1) [2]:

Abrasive wear: is caused by cutting or ploughing one surface by another, harder surface. The harder material may simply be a harder alloy or hard irregularities on the counter surface; it may also be an oxide, carbide, work-hardened particle or other foreign material.

Adhesive wear: material loss by transfer and adhesion to the counter surface. It is the most common and difficult to control. It results from the welding or adhesion and subsequent rupturing of contacting asperities on a surface. It is particularly severe between sliding pairs of metals that are chemically similar and/or mutually soluble. Adhesive wear is closely related to surface friction in such a way that an increase in frictional forces generally causes a large increase in resulting wear.

Erosion wear: the wear of material under the flow of any environment (gas, liquid, or mixtures thereof in the presence or absence of mechanical particles), which are the result of changing the geometry, of the weight loss, etc.

Corrosive wear: the wear of material that occurs due to some type of chemical or electrochemical reaction with the environment. It may be due to general oxidation, chemical fumes, humidity, or combustion products, and may also be inadvertently caused by ingredients in lubricants.

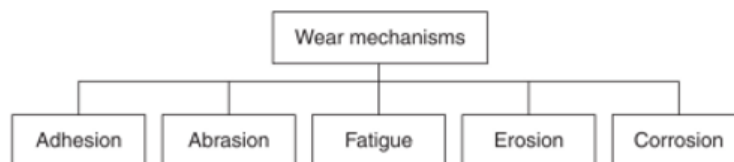


Figure 1: Various types of wear mechanisms.

Adhesive Wear Failures

Friction and wear are important when considering the operation and efficiency of components and mechanical systems. Among the different types and mechanisms of wear, adhesive wear is very serious. Adhesion results in a high coefficient of friction as well as in serious damage to the contacting surfaces. In extreme cases, it may lead to complete prevention of sliding; as such, adhesive wear represents one of the fundamental causes of failure for most metal sliding contacts,

accounting for approximately 70 % of typical component failures. The different mechanisms and failure modes of adhesive wear are scoring, scuffing, seizure, and galling [3].

Adhesive wear is characterized by transferring a material from one contacting surface to another during the relative motion caused by localized bonding. It occurs when high loads, temperatures, or pressures cause the asperities on two contacting metal surfaces in relative motion to deform and spot weld together, followed by plowing, tangential shearing, and tearing of the metal in small, discrete areas called micro joints [3].

During the adhesion process and material transfer, particles are removed from one contact surface and either permanently or temporarily attached to the other surface by a cold-welding process, thus leaving pits, voids, or cavities on the surface and causing roughening of both contact surfaces as well as rapid wear.

Due to the cold-welding process, the generated particles are harder than the surfaces from which they originate and thus can cause great damage and speed up abrasive and erosive wear [4]. As such, adhesive wear initiates microscopically but progresses macroscopically.

The adhesive wear failure process can be summarized as [5, 6] (Figure 2):

1. Formation of adhesive micro junctions,
2. Deformation of contacting asperities,
3. Removal of protective oxide surface films,
4. Crack initiation and propagation,
5. Failure of junctions by shearing and tearing, and
6. transfer of material.

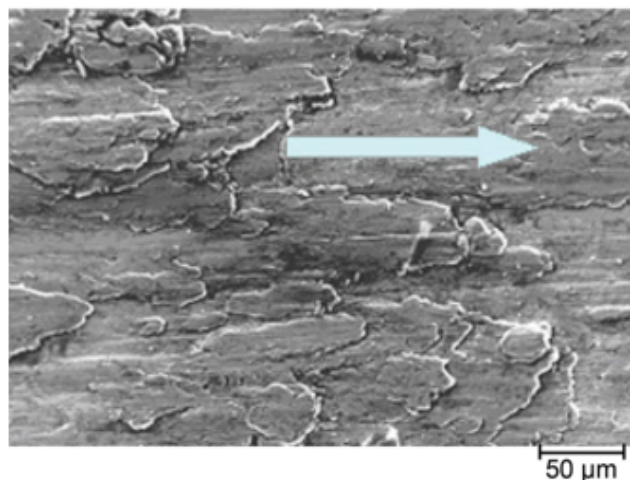


Figure 2: Adhesive wear shown by transferred layers of titanium alloy on a steel surface [3].

In such cases, a large frictional force and plastic Deformation caused by dislocations are introduced to the contact region. As a result of such a large deformation, a crack is initiated and is propagated in the combined fracture mode of tensile load and shearing [3] (Figure 3).

Recrystallization of MP159 superalloy during hot Deformation

The microstructure evolution of the superalloy during hot deformation is a complex process, involving deformation heat, flow location, dynamic recovery, and dynamic recrystallization. The size and volume fraction of recrystallized grains were significantly affected by hot working parameters [7, 8].

The dynamic recrystallization behavior of MP159 superalloy studied by Cai et al. [9], since they found that:

The volume fraction and grain size of recrystallized grains increased with increasing strain rate and deformation temperature. Deformation twins that formed during hot deformation provided nucleation sites for dynamic recrystallization (DRX) and accelerated the DRX process.

Discontinuous dynamic recrystallization (DDRX) was the dominant mechanism for the MP159 alloy at different deformation strains. Due to the low thermal conductivity of the MP159 superalloy, the heat generated by plastic deformation could not be released in time at higher strain rates [9]. Figure 3b) and c) show that the DRX grain size increased with increasing strain rate, which was attributed to increased deformation heating.

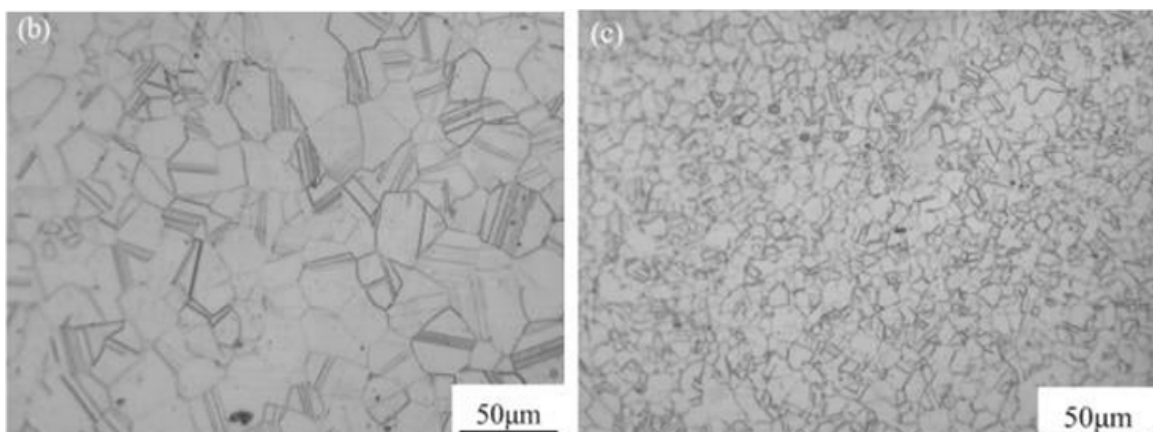


Figure 3: DRX grain presented in MP159 alloy with deferent strain rate and deformation heating: b) 950 °C / 10 s⁻¹, c) 980 °C / 1 s⁻¹.

Wu et al. [10] reported that the dynamic recrystallization of GH984G was strongly affected by the initial grain sizes of alloys. The dynamic recrystallization (DRX) mechanism for GH984G alloys is mainly continuous dynamic recrystallization (CDRX) for larger initial grains and discontinuous dynamic recrystallization (DDRX) for fine grains. God suet al. [11] observed

the hot deformation of cast superalloy 625 and found that the dynamic recovery and DDRX mechanisms are mostly.

Responsible for microstructural modification, and the formation of twins controlled the recrystallization rate. Moreover, factors including the initial δ phase, deformation temperature and strain rate also have a clear influence on the DRX of superalloys [12, 13]. Wen et al. [12] showed that the δ phase pre-existing in alloys first stimulates the occurrence of DRX and then gives rise to a weak effect with increasing deformation temperature. Above all, the hot deformation behavior of different superalloys varies with the chemical composition, initial grain size, initial phases, strain rate, and deformation temperature.

Severe plastic deformation

Severe plastic deformation (SPD) refers to a group of techniques used to process metals and alloys to achieve ultrafine-grained microstructures. These techniques induce very high strains on the material, resulting in significant changes in its microstructure and properties [14]. Severe plastic deformation (SPD) refers to a group of techniques used to process metals and alloys to achieve ultrafine-grained microstructures. These techniques induce very high strains on the material, resulting in significant changes in its microstructure and properties. The FSW process has been recently classified as a special type of severe plastic deformation method. FSP technique with certain improvisations can be used to modify the material microstructure by densification of localized grain refinements and homogenization of precipitate particles such that the metal properties can be changed through intense plastic deformation at elevated temperature [14].

The procedure for grain refinement using SPD techniques is mentioned below [14]:

- i. The dislocations, initially scattered across the grains, reorganize, and regroup together into dislocation cells to minimize overall strain energy.
- ii. Misorientation between the cells occurs as the deformation picks up and more dislocations are formed, resulting in sub-grains forming.
- iii. This process continues inside the sub-grains till the size is small enough for the sub-grains to rotate.
- iv. More deformation leads to the rotation of sub-grains to rotate into high-angle grain boundaries, which are often equiaxed in shape.

Plastic deformation by grain boundaries sliding mechanism

The deformation behavior caused by the coarse-grained materials has become well-understood by now. The postulated mechanism has followed the model explaining the grain boundary sliding at high temperatures that were initially established. Therefore, the exterior dislocations slide across the grain boundaries, which gives rise to an accumulation of dislocations at the obstruction points like triple junctions. Stress builds up at the top of the pile-up, triggering a source of dislocation in a distinct slip mechanism of the obstructed grain. Such dislocations slip through the blocking grain, keep piling up at the adjoining grain boundary, climb the barrier, and are then consumed into it. Basic characterizations for the model are depicted visually in Figure 4 [14].

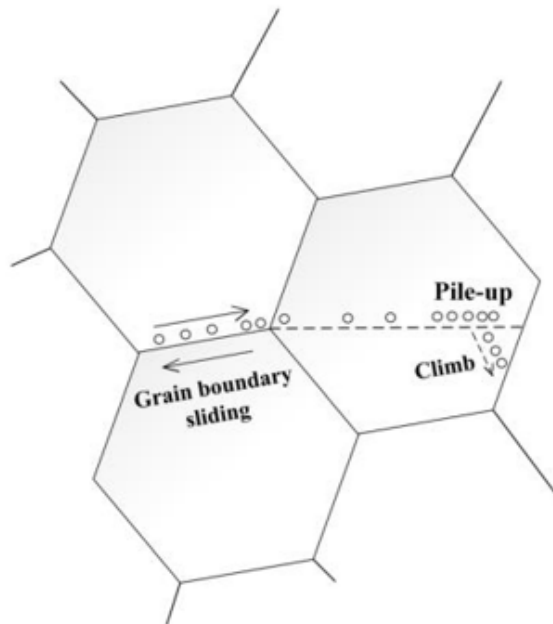


Figure 4: Schematic of deformation mechanism [14].

References

- [1] G. W. Han, I. P. Jones, and R. E. Smallman, 'Direct evidence for Suzuki segregation and Cottrell pinning in MP159 superalloy obtained by FEG(S)TEM/EDX,' *Acta Mater.*, vol. 51, no. 10, pp. 2731–2742, Jun. 2003, doi: 10.1016/S1359-6454(02)00359-2.
- [2] M.-K. Besharati-Givi and P. Asadi, *Advances in Friction-Stir Welding and Processing*. Elsevier, 2014.
- [3] 'Adhesive Wear Failures | SpringerLink.' <https://link.springer.com/article/10.1007/s11668-021-01322-4> (accessed Jun. 13, 2023).

- [4] B. Podgornik, 'Adhesive Wear Failures,' *J. Fail. Anal. Prev.*, vol. 22, no. 1, pp. 113–138, Feb. 2022, doi: 10.1007/s11668-021-01322-4.
- [5] B. Bhushan, *Modern Tribology Handbook, Two Volume Set*. CRC Press, 2000.
- [6] H. Hirani, *Fundamentals of Engineering Tribology with Applications*. Cambridge University Press, 2016.
- [7] S. Mitsche, C. Sommitsch, D. Huber, M. Stockinger, and P. Poelt, 'Assessment of dynamic softening mechanisms in Allvac® 718Plus™ by EBSD analysis,' *Mater. Sci. Eng. A*, vol. 528, no. 10, pp. 3754–3760, Apr. 2011, doi: 10.1016/j.msea.2011.01.044.
- [8] Y. Cai, S. Xiang, and Y. Tan, 'Insight into the Dynamic Recrystallization Behavior and Microstructure Evolution of MP159 Superalloy During Hot Deformation,' *Met. Mater. Int.*, vol. 28, no. 10, pp. 2381–2394, Oct. 2022, doi: 10.1007/s12540-021-01139-8.
- [9] Y. Wu, Z. Liu, X. Qin, C. Wang, and L. Zhou, 'Effect of initial state on hot deformation and dynamic recrystallization of Ni-Fe based alloy GH984G for steam boiler applications,' *J. Alloys Compd.*, vol. 795, pp. 370–384, Jul. 2019, doi: 10.1016/j.jallcom.2019.05.022.
- [10] A. K. Godasu, U. Prakash, and S. Mula, 'Flow stress characteristics and microstructural evolution of cast superalloy 625 during hot deformation,' *J. Alloys Compd.*, vol. 844, p. 156200, Dec. 2020, doi: 10.1016/j.jallcom.2020.156200.
- [11] 'A new dynamic recrystallization kinetics model for a Nb containing Ni-Fe-Cr-base superalloy considering influences of initial δ phase - ScienceDirect.' <https://www.sciencedirect.com/science/article/pii/S0042207X17302385> (accessed Jun. 14, 2023).
- [12] Y. C. Lin et al., 'EBSD analysis of evolution of dynamic recrystallization grains and δ phase in a nickel-based superalloy during hot compressive deformation,' *Mater. Des.*, vol. 97, pp. 13–24, May 2016, doi: 10.1016/j.matdes.2016.02.052.
- [13] P. S. Sahoo, A. Meher, M. M. Mahapatra, and P. R. Vundavilli, 'Understanding the Fabrication of Ultrafine Grains Through Severe Plastic Deformation Techniques: An Overview,' *JOM*, vol. 74, no. 10, pp. 3887–3909, Oct. 2022, doi: 10.1007/s11837-022-05442-6.
- [14] W. Kuang et al., 'Fretting wear behaviour of machined layer of nickel-based superalloy produced by creep-feed profile grinding,' *Chin. J. Aeronaut.*, vol. 35, no. 10, pp. 401–411, Oct. 2022, doi: 10.1016/j.cja.2021.10.007.

Analysis of the properties of hot work tool steel

Jakub Długosz¹, Adrian Bednarczyk¹, Aneta Łukaszek – Sołek¹, Grzegorz Ficak^{1,2*}

¹ Akademia Górniczo-Hutnicza im. Stanisława Staszica w Krakowie, Wydział Inżynierii Metali i Informatyki Przemysłowej, Al. Mickiewicza 30, 30-059 Kraków

² GK Forge Sp. z o.o. Przemysłowa 10, 43-440 Golezów

* Author to whom correspondence should be addressed

The study analyzed and compared the properties of three types of hot work tool steels: X37CrMoV5-1, Unimax, and Vidar Superior. All mentioned steels are intended for use in forging dies. The focus of the study was to investigate properties critical to selected die wear mechanisms. A literature review guided the selection of research and desired properties to characterise the dies. The main objectives of the study were formulated, including verification of manufacturer's warranties, heat treatment of the steel, microstructural investigation, hardness, impact toughness and wear resistance. The results of the research were compiled and compared, leading to conclusions regarding the suitability of the steels for use in forging tools.

Keywords: forging dies, heat treatment, tool steels, forging dies, tools, hardness, toughness

1. Introduction

The aim of this study is to compare and analyze the properties of three types of hot work tool steels. These are: X37CrMoV5-1, Unimax, and Vidar Superior. All of the steels mentioned are used in forging dies. The main objectives of the study are as follows:

- Verification of manufacturer's warranties regarding the properties of steel in the as-delivered condition and after heat treatment,
- Selection of parameters and conducting heat treatment of the tested steels,
- Microstructure analysis,
- Investigation of properties such as hardness and toughness at elevated temperatures.

Commonly used materials for dies and die inserts for hot forging are tool steels characterized by stable properties at elevated working temperatures ranging from 200 to 700 °C. A literature review was conducted to identify research areas and the desired properties that die cavities should exhibit. Die forging tools must meet a series of requirements such as [1–3]:

- High impact toughness (resistance to dynamic loads),
- Wear resistance,
- Thermal-mechanical fatigue resistance,
- Compressive strength.

Forging dies are made of hot work tool steels, which must exhibit high hardness, toughness, and wear resistance [4, 5]. Steels should exhibit stability of these parameters at elevated temperatures, usually up to 500 °C [6].

The aim of this study is to compare three selected types of hot work tool steels: X37CrMoV5-1, Unimax, and Vidar Superior. The chemical compositions of the respective steels are presented in the Table 1 [7–9]:

Table 1: Chemical composition of the selected steels.

Steel:	Chemical composition [wt%]							
	C	Mn	Si	P	S	Cr	Mo	V
X37CrMoV5-1	0.33 – 0.41	0.25 – 0.50	0.8 – 1.2	< 0.03	< 0.02	4.8 – 5.5	1.1 – 1.5	0.3 – 0.5
Unimax	0.5	0.2	0.5	–	–	5.0	2.3	2.5
Vidar Superior	0.36	0.3	0.3	–	–	5.0	1.3	0.5

- Vidar Superior – Vidar Superior is a chrome-molybdenum steel produced by Uddeholm company. Its chemical composition is similar to X37CrMoV5-1 steel. The manufacturer states that increased metallurgical purity and small grain size enable achieving higher hardness (up to 2 HRC) with higher toughness than in the case of X37CrMoV5-1 steel. The working hardness of the steel ranges from 40 to 52 HRC. At such hardness, the tensile strength reaches 1680 MPa. The tempering temperature is 1000 °C [7].
- Unimax - Uddeholm Unimax is a tool steel with additions of chromium, molybdenum, and vanadium. The steel production process has been enriched with electric arc furnace refining, which beneficially affects its mechanical properties. The steel is characterized by relatively high working hardness – above 55 HRC after double tempering. At this hardness, the tensile strength reaches 1780 MPa [8].
- X37CrMoV5-1 - is an alloy steel with high hardenability, characterized by resistance to thermal fatigue, tempering, and oxidation. Typically, its working hardness can range from 45 to 55 HRC. The addition of carbide-forming elements enables achieving secondary hardness effects and increases resistance to the tempering effect of temperature. The steel exhibits a tensile strength of 1600 MPa (yield strength of 1380 MPa) at a hardness of 48 HRC [9].

2. Experimental procedure

Samples measuring 10.5x10.5x55 mm were quenched and tempered according to the schemes presented in the Table 2.

Table 2: Heat treatment procedures for selected steels.

No.	Steel	Manufacturer's recommendations		Heat treatment		Quenching medium
		Quenching [°C]	Tempering [°C]	Quenching [°C/min]	Tempering [°C/min]	
1	X37CrMoV5-1	1000 – 1050	525 – 650	1030/25	580/2x120	Oil
2	Unimax	1000 – 1025	525	1025/35	525/2x120	OH70 -
3	Vidar Superior	980 – 1000	525 – 600	1000/35	580/2x120	70 °C

After quenching, a finishing operation was performed with the aim of removing the decarburized and oxidized layer and machining a 'V' notch for Charpy impact testing.

During experimental procedure the following parameters were measured and analyzed:

- Hardness of the samples was measured in the as-delivered state, after quenching, between tempering cycles, and after the entire heat treatment process. Hardness measurements after heat treatment were conducted using the Rockwell method. After preparing metallographic specimens, hardness was measured using the Vickers method with a 5 kg load (HV5).
- Toughness was measured by Charpy impact test. Samples were prepared according to the standard [10]. To replicate the working conditions of the dies, tests were conducted at temperatures of 20, 200, 400, and 600 °C.
- Microstructures of the steel in the as-delivered state and after heat treatment were examined. Samples of hardened steel were cut from the center of the tested components to allow for examination of the microstructure across the entire cross-section. The examinations were conducted using a LEICA DM4000M light microscope. Images of each sample were taken using a 100x magnification objective lens.

3. Results and discussion

The chapter presents the results of the conducted research. Hardness of the steel was measured in its as-delivered state as well as after subsequent heat treatment processes. Microstructure analysis and impact toughness measurements were performed on samples after the complete heat treatment process.

3.1. Analysis of Hardness

Results of the hardness test is presented in Table 3.

Table 3: Results of the hardness test.

Steel	Hardness after each process				
	As-delivered [HV5]	Quenched [HRC]	Tempered [HRC]	Tempered twice [HRC]	[HV5]
X37CrMoV5-1	190	57	51	50.3	520
Unimax	177	62	55	54	580
Vidar Superior	162	56.5	49	48.5	480

Hardness of X37CrMoV5-1 steel in its as-delivered state is 190 HV5. Directly after hardening, the hardness reaches around 57 HRC. A double tempering process resulted in a reduction of hardness to 520 HV5 (approximately 50 HRC), with a minor difference between the hardness after the first and second tempering, approximately 0.7 HRC.

Vidar Superior steel exhibited the lowest as-delivered hardness of 165 HV5. Hardening and double tempering led to an increase in hardness to around 480 HV5. Immediately after hardening, the hardness was similar to that achieved by X37CrMoV5-1 steel. However, after tempering, the difference exceeded 40 HV5.

Unimax steel measured 177 HV5 on the tested samples, consistent with the hardness provided by the manufacturer. Hardness after hardening reached 62 HRC, and as a result of double tempering, it decreased to 54 HRC.

3.2. Analysis of Toughness

Results of the toughness test are presented in Table 4.

Table 4: Results of the toughness test.

No.	Steel	KCV [J/cm ²]			
		20 °C	200 °C	400 °C	600 °C
1	X37CrMoV5-1	22.1	33.1	38.6	60.1
2	Unimax	5.5	24.5	33.7	45.4
3	Vidar Superior	26.1	73.6	117.7	131.2

Vidar Superior steel exhibited the highest impact toughness at all temperatures. There is also a correlation between the results and hardness measurements – the steel with the lowest hardness demonstrates the highest impact toughness. X37CrMoV5-1 steel showed lower impact toughness than Vidar Superior. Despite initially similar fracture work of 22.1 J/cm², this steel does not exhibit such a significant increase in impact toughness.

Unimax is characterized by relatively low impact toughness compared to the two previously described steels. The low impact toughness correlates with high hardness and an expected high carbide content in the microstructure.

3.3. Analysis of Microstructure

The examinations were conducted using a LEICA DM4000M light microscope. Images of each sample were taken using a 100x magnification objective lens. The microstructure of the steel X37CrMoV5-1 is presented in the Figure 1.

The microstructure of the X37CrMoV5-1 steel in the as-delivered state (Figure 1a) consists of spheroidite with remnants of pearlite plates. Precipitates are unevenly distributed and align along the grain boundaries in an interrupted line.

The microstructure of the Unimax and Vidar Superior steels in the as-delivered state (Figure 1c and 1e) consists of spheroidite. Precipitates are evenly distributed throughout the sample, indicating good uniformity of chemical composition.

The microstructure of all hardened steels (Figure 1b, 1d and 1f) comprises tempered martensite with primary carbide precipitates. The nature of the microstructures cases correlates with the hardness of the samples.

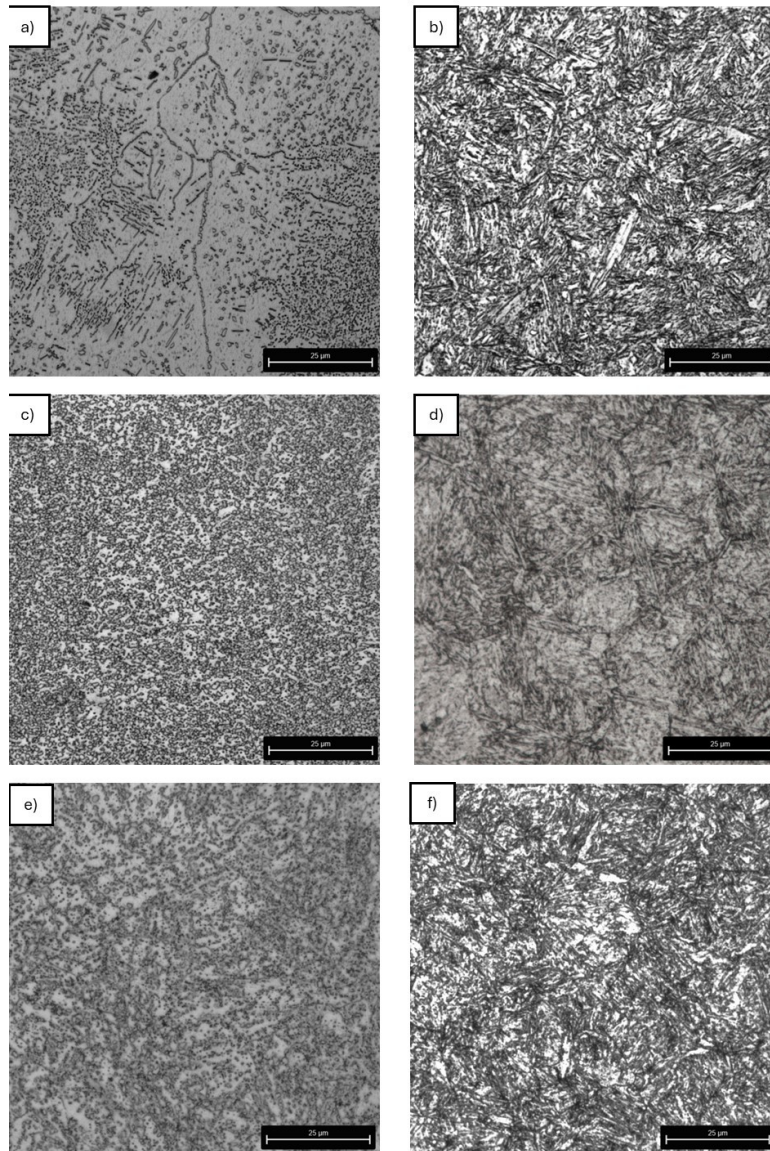


Figure 1: a) X37CrMoV5-1 as delivered b) after heat treatment, c) Unimax as delivered d) after heat treatment, e) Vidar Superior as delivered d) after heat treatment.

4. Conclusions

This study analyzed three types of hot work tool steels: X37CrMoV5-1, Unimax, and Vidar Superior, aimed at evaluating their suitability for use in forging dies and other tools used in die forging.

- Microstructure analysis in the as-delivered state indicates that the steels supplied by Uddeholm company exhibit high quality in terms of microstructure uniformity and heat treatment.
- For X37CrMoV5-1 steel, minor segregations of chemical composition and remnants of pearlite were observed, which could potentially affect the steel's quality.

- The tested samples, after quenching, exhibit a uniform structure of tempered martensite. Hardness values after heat treatment align with the assumptions based on hardness-tempering temperature dependency charts.
- Based on impact toughness testing at elevated temperatures, it was found that Vidar Superior steel demonstrates the highest resistance to cracking-related wear. Its very high toughness enables its use in tools operating at high deformation speeds, such as forging hammer dies. However, caution should be exercised when using it in tools subjected to high pressures.

References

- [1] Turek J., Struktura i właściwości warstw napawanych na wykrojach matryc kuźniczych, wydawnictwo Politechniki Krakowskiej, Kraków 2019.
- [2] Żmichorski E., Stale narzędziowe i obróbka cieplna narzędzi, Wydawnictwo Naukowo – Techniczne, Warszawa 1967.
- [3] Gronostajski Z., Będza T., Kaszuba M., Marciniak M., Polak S., Modeling the mechanisms of wear in forging tools, *Obróbka Plastyczna Metali* Vol. XXV Nr 4 (2014).
- [4] Gronostajski Z., Kaszuba M., Hawryluk M., Nowak M., Tool lifetime in forging processes, *Obróbka Plastyczna Metali* vol. XXVI nr 3 (2015).
- [5] Hawryluk M., Widomski P., Ziemia J., Analysis of the causes of rapid damage of forging tools, *Obróbka Plastyczna Metali* vol. XXVIII nr 1 (2017).
- [6] <https://wm.pollub.pl/wydzial-mechaniczny/jednostki-organizacyjne/katedra-obrobki-plastycznej-metali/nauka/kucie-matrycowe>. Acces online 25.03.2024.
- [7] Uddeholm Vidar ® Superior, datasheet.
- [8] Uddeholm Unimax ®, datasheet.
- [9] Uddeholm Vidar ® 1, datasheet.
- [10] PN-EN ISO 4957:2004 standard.

Funding: The Ministry of the Education and Science financed this work within the seventh edition of the Implementation PhD programme.

Application of modern manufacturing methods in sword blades restoration

Jakub Długosz¹, Kamil Kokot¹, Weronika Fidura¹, Piotr Ledwig¹

¹AGH University of Science and Technology, Faculty of Metals Engineering and Industrial Computer Science

The paper describes the examination and restoration process of a pattern-welded damascus steel sword blade. The blades were received by our science club in a corroded state and without any handle elements. Initial analysis suggests that they were crafted by a German blacksmithing company in the early 20th century. To gain a better understanding of their history, samples were taken for evaluation under an optical microscope, and the blades' hardness was measured. These observations indicate that the blades served a purely decorative function rather than a utilitarian one. The restoration of the blades involved cleaning and acid etching to reveal the damascus pattern. New pommels were made using the laser powder bed fusion additive manufacturing method. It is planned to create new handles and a crossguard based on the historical design.

Keywords: sword, pattern weld, microstructure analysis, hardness, restoration

1. Introduction

Metal components are damaged by corrosion and mechanical failure. A repair or manufacture of a replacement part is then required. However, for historical or old objects finding suitable replacements can be a challenge and custom-made parts may be necessary.

The modern manufacturing methods such as 3D printing of metal are increasingly being utilized to produce replacement parts that are no longer in production. The process of 3D printing involves producing components layer by layer using 3D computer models. This enables the production of components with complex shapes that cannot be produced using casting or cavity machining methods. The ability to easily modify 3D models makes 3D printing a quick method for producing the necessary components for restoration. Nowadays, 3D printing enables the production not just prototypes, but also functional materials with good mechanical properties. The Laser Powder Bed Fusion (LPBF) method allows for excellent reproduction of metallic components, due to the use of micrometric powder layer thickness and precise selective melting with a laser beam. The LPBF method has been used to produce pommels for old sword blades.

The received sword was presented at Figure 1. Blade is made of pattern welded steel, commonly referred to as Damascus steel. Considering the production technology and materials of that time it can be assumed that the sword was purely ceremonial and decorative applications. Swords made of Damascus steel were most often memorabilia or gifts, because despite the complicated manufacturing process, they not characterized by better mechanical properties than conventional

steel produced at that times. It is highly likely that these swords belonged to an army or navy officer.

The aim of the project was to characterize the microstructure and properties of the steel of the swords, and then to restore them using classical and modern methods, including LPBF.



Figure 1: Picture of swords.

2. Experimental procedure – microstructure and hardness

To microstructure and hardness investigations 3 small samples were collected from areas near the tang and at the tip of the blade (Figure 2). The samples were embedded perpendicular to the layer arrangement so that all layers were visible in the cross-section of the blade. The steel samples were ground, polished and etched in 2% nital, and analyzed using a LEICA DM4000M optical microscope.



Figure 2: Scheme of the sword, with sample cut-out areas marked in red.

Hardness was measured using Vickers hardness tester using 0.5 kg load. Five measurements were taken for analysis, with the lowest and highest values discarded.

3. Microstructure analysis

At the Figure 3 the microstructure of sample B taken near the tang were shown.

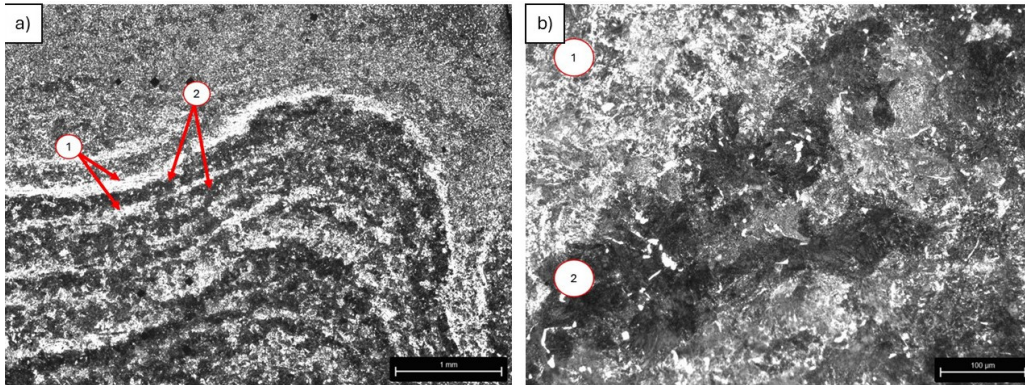


Figure 3: Microstructure of sword in area near the tang.

The microstructure shows a layered structure, consisted with ferritic-pearlitic microstructure, indicating a steel with lower carbon content (area No. 1) and perlite with small grains of ferrite in areas with dark contrast. In Figure 3b, the transition between the medium and high carbon layers was observed. The variation in the content of microstructural components in individual layers suggests the use of two steels differing in carbon content. The presence of perlite and ferrite in the microstructure indicates relatively slow cooling after forging. Which was confirmed by hardness values at around 250 HV5.

At the Figure 4 the microstructure of steel sample taken from the tip were shown. The microstructure in both layers exhibits a martensitic character, indicating a conducted heat treatment - quenching and tempering. The hardness of the sample was about 500 HV0.5.

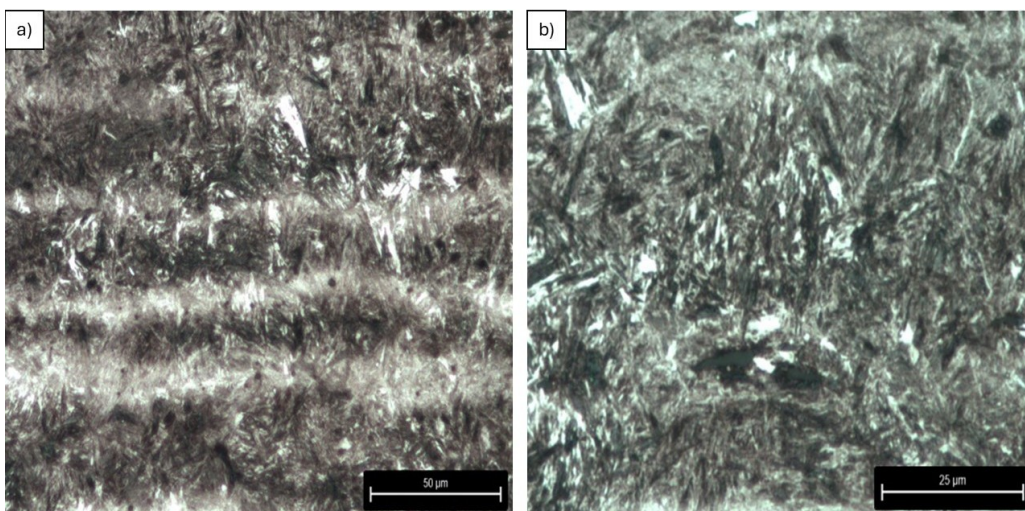


Figure 4: Microstructure of sword in area of the tip.

4. Blade restoration

The blade of the received sword was covered by corrosion products due to prolonged storage in non-dry conditions. Despite the advancing corrosion, it was still possible to discern the previously etched pattern of the Damascus steel layers. To prepare the sword for re-etching, the blade was first ground and then polished. The successive stages of preparation consisted of:

1. Coarse grinding – using P220 grit sandpaper, the corroded layer was removed, and part of the pits was ground down.
2. Finishing grinding – the surface finished with P220 grit sandpaper was smoothed using P400 grit sandpaper. The resulting surface was ready for polishing.
3. Polishing – was carried out using two polishing pastes. The first (coarse) paste had grain sizes at around $6\ \mu\text{m}$. The abrasive material used was iron (III) oxide. The second stage involved finishing polishing using a paste with a grain size of $3\ \mu\text{m}$, consisting of chromium oxide.

The schematic of the grinding and polishing process is presented in the Figure 5.

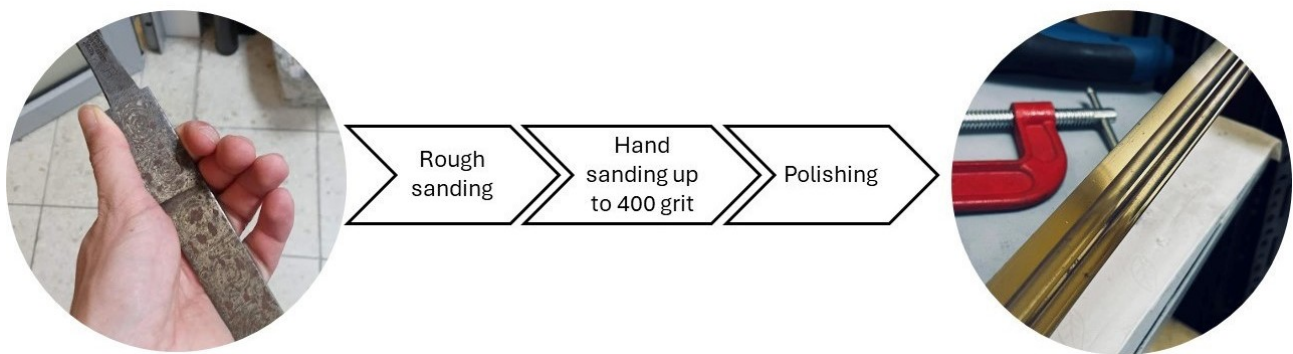


Figure 5: Polishing process.

5. Manufacturing pommels by LPBF

To prepare the sword pommels, LPBF were used. 3D models were created in SOLIDWORKS software. Examples of two models are shown in the Figure 6.

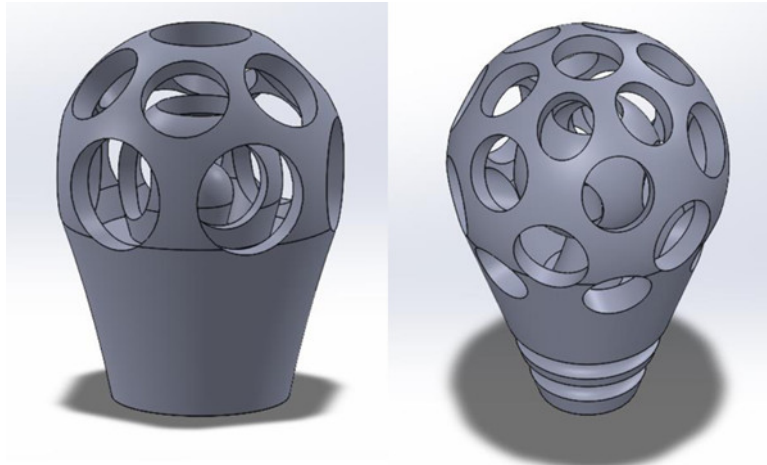


Figure 6: 3D models of pommels.

Manufacturing of the sword pommels was performed on AYAS 120 LM LPBF 3D printer using following parameters:

- Laser power: 130 W,
- Scanning speed: 0.9 m/s,
- Hatch distance: 80 μm ,
- Layer thickness: 30 μm ,
- Scanning strategy: 67° rotation,
- argon

In the process the mixture of of 316L steel and Inconel 625 were used. The powder was recycled from previously conducted researches using two separates powders. The Pictures of as-printed models is shown on the Figure 7.



Figure 7: Image of LPBF printed pommels on build plate.

Microstructure of LPBF samples

Microstructure of LPBF material were showed on the Figures 8 and 9. The material had a low porosity of less than 0.2%. Mainly gas porosity was observed. In the Figure 8a gas pores are marked by red arrows. At the Figure 8b higher magnification were showed. The microstructure consisted by elongated in build direction grains with cellular substructure and evenly dispersed nanometric oxides. The observed microstructure is characteristic of steels and nickel alloys produced by this method. No significant segregation from the different powders was observed in the material, indicating that good mixing of the two materials occurred during the process. In material some amount of cracks in the grain boundary areas were observed (Figure 9).

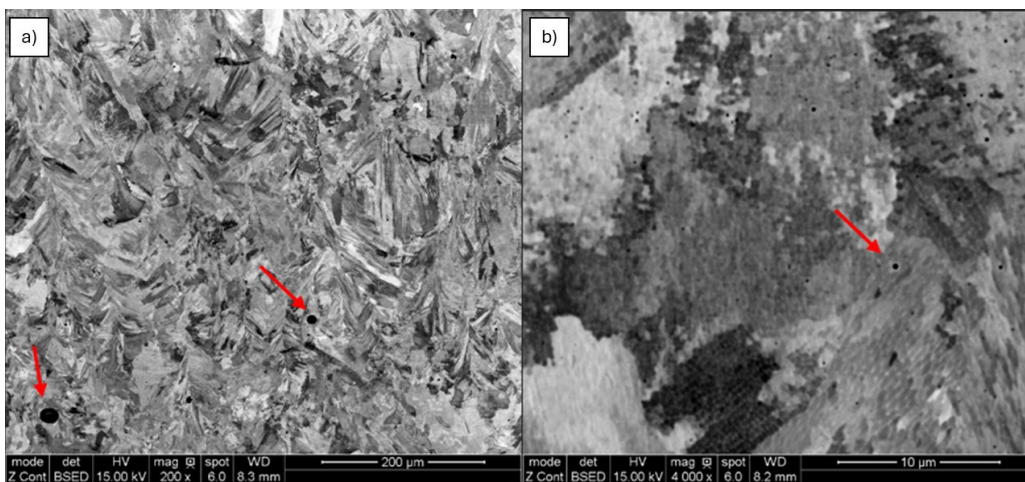


Figure 8: Microstructure of LPBF samples.

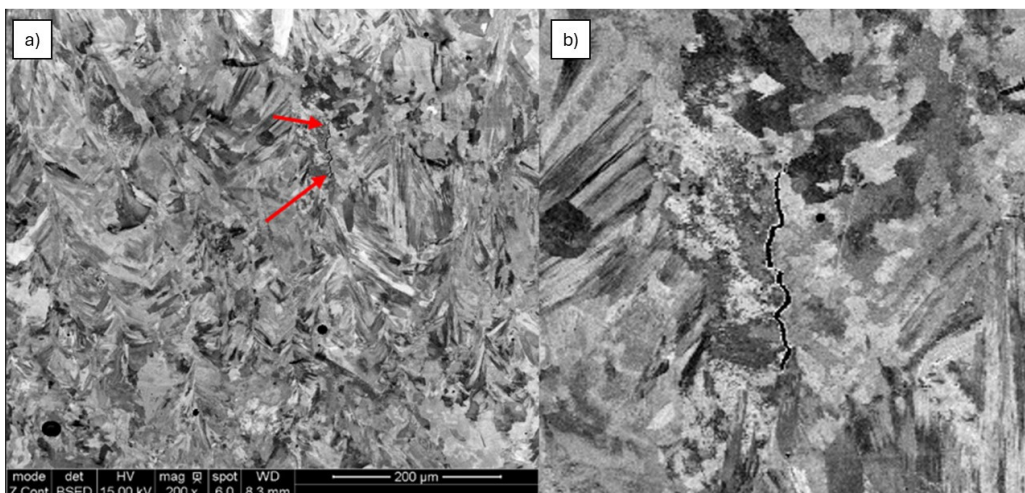


Figure 9: Microstructure of LPBF samples.

6. Conclusions

On the basis of the study, it can be concluded that:

- The material for the sword blade was intentionally chosen to possess good mechanical properties alongside high hardness.
- The character of the microstructure indicates partial hardening of the blade, only in the sharpened part, while the tang and the area between the blade and the hilt remain unhardened.
- The conducted polishing allowed for achieving a surface finish enabling re-etching to reveal the pattern of Damascus steel.
- Through the LPBF process, it was possible to produce a sword pommel that can be successfully used in reconstructing original pommels that are no longer manufactured.

Variations in the wettability behavior of material surfaces caused by petroleum and hydraulic oil

Fadhil Mohanad^{1*}

¹ University of Miskolc, Institute of Physical Metallurgy and Metal Forming and Nanotechnology

* Corresponding author: mohanad.khairi@uni-miskolc.hu, engineer81@yahoo.com

1. Literature review

1.1. Introduction

Water is an essential component of oil and gas operations; it is produced and used in both upstream and downstream facilities, and it had a strong corrosion-inducing agent on the equipment surface. Corrosion is a process in which the metal's surface becomes impaired and eventually destroyed. It is a natural process that takes place in alloys, and it can cause problems with the structural integrity of steel structures over time. In some cases, the corrosion will cause a significant structural weakening in the steel or could cause the steel to break apart completely. This phenomenon is known as 'steel rot'. Steel rot can occur in many different types of steel structures, including pipelines, tanks, vessel, beams, columns, girders. In extreme cases, steel rot can cause the metal pitting, which could cause the metal to crack and fall away from the structure, and special if a crack extends all the way through the wall, it could collapse and cause significant damage to the rest of the structure.

To prevent these serious problems, it is important to inspect the steel on a regular basis and to address any areas that show signs of corrosion. For this reason, it is necessary to add corrosion inhibitors such as phosphates and nitrates during the refining process. Corrosion inhibitors are commonly added to coolants, fuels, hydraulic fluids, boiler water, engine oil, and many other fluids used in industry. One of the ways to improve anti-corrosion properties is by improving the wettability. This can be done by adding special coatings to the surface. This type of coating is usually applied to carbon steel parts after they have been treated with corrosion inhibitors and primers. It is expecting that by improving wettability for the coating can help reduce the amount of liquid present on a metal surface, thereby preventing it from coming into contact with oxygen and reducing the rate of corrosion.

1.2. Oil / Water Problems set on the metal surfaces

The expansion of Oil and Gas (O & G) production from atypical resources was extremely dependent upon technologies, which utilize large amount of water such as hydraulic fracturing for O & G extraction from shale regions. In terms of produced water production volumes, about three to four barrels of water are produced with each barrel of normal oil extracted. Many factors (type, geological properties and the time life of a formation) effect on this amount of barrels could be increases the number of the water barrels more than four [1, 2].

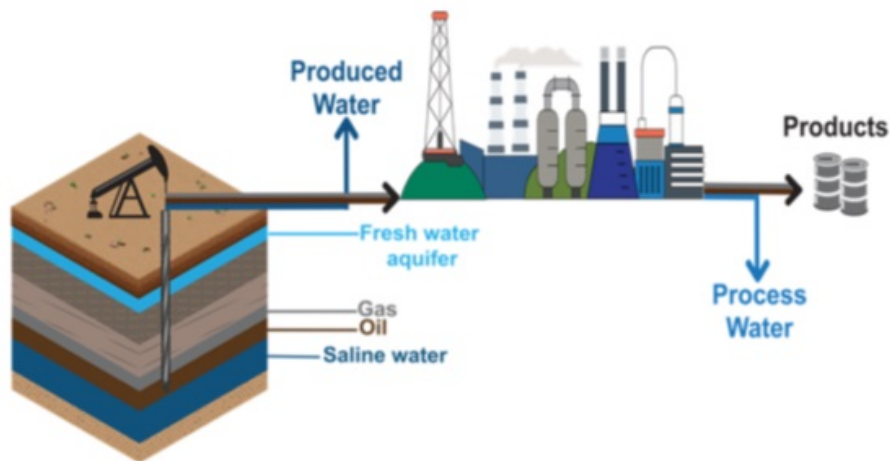


Figure 1: Produced and process water in the Oil and Gas industry [1].

Generally, oil / water mixture may be labelled as categories not miscible or the emulsion that consists of oil-water emulsions [3]. The petroleum enterprise typically classifies crude oil depend on the geographic region it's produced in (Brent, Oman, West Texas) and its API gravity (The degree of density of the oil foundation) with the content of sulphur. Crude oil can be taken into consideration as mild if it has low density, heavy if it has excessive density, or medium if it has a density among that of mild and heavy [4]. Additionally, it may be described as sweet if it contains little sulphur or sour if it contains a lot of sulphur [5]. Produced water with crude oil typically contains different type of additives and in varying concentrations could be leading to the corrosion as shown the composition in Table 1 [6]:

Table 1: Oil Composition by weight [6].

Element	Carbon	Hydrogen	Nitrogen	Oxygen	Sulphur	Metals
% Range	83 to 85 %	10 to 14 %	0.1 to 2 %	0.05 to 1.5 %	0.05 to 6.0 %	< 0.1 %

Corrosive media aggressive is a real scientific and technical issue. Pipes used for crude oil extraction and transportation are constantly in contact with corrosive media and harmful materials of the metal surface that cause in-depth corrosion of pipes with the increase of

corrosiveness media aggressive (air, soil and water) Figure 2. Thus, crack resistance of metallic are decreased, leading to lessen the thickness of the pipe wall, and led to metallic abrasion (like: Pitting, uniform corrosion, hydrogen induced cracking, flow induced, stress corrosion, etc.) at some point of the pipeline under-process and their abrasion is followed with high economic losses and extreme ecological consequences [7, 8]. This has been affirmed through the day statistical data, namely, that nearly 80% of all oil pipeline disasters are due to number one corrosion-mechanical harm and through progressing bases fissuring problems in locations of corrosive caverns and welding joints [9].

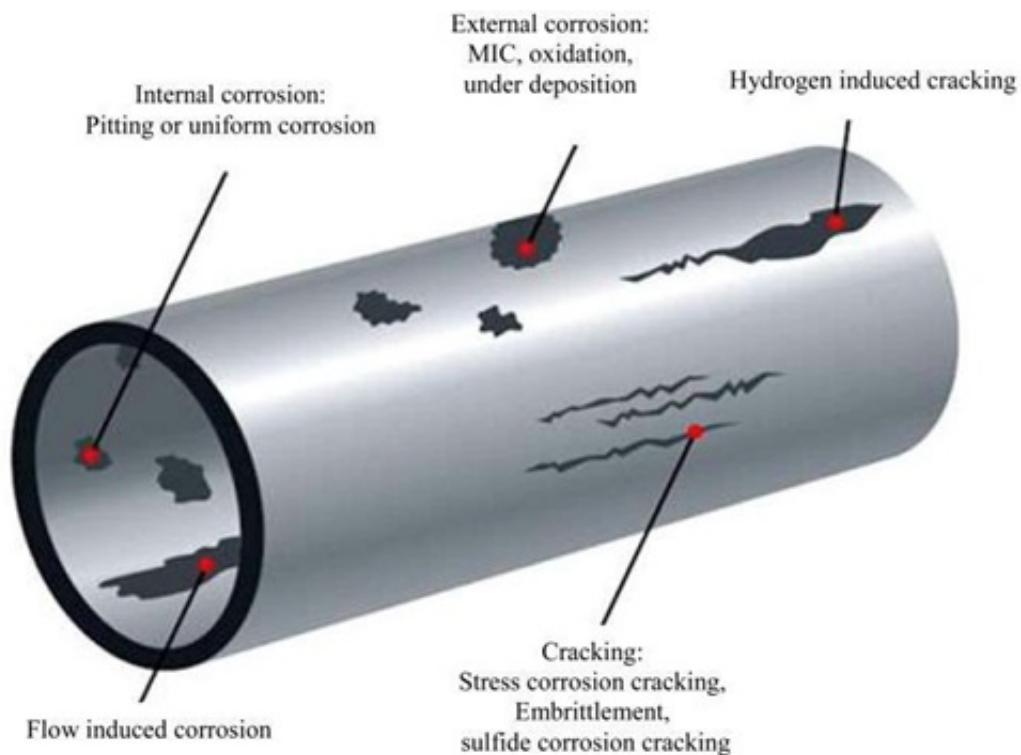


Figure 2: Corrosion types in oil pipeline [10].

The properties of fatigue and corrosive fatigue failure of pipes in dependence on the preliminary length and shape of the distorted with inside the pipeline defects may be obtained, then the investigation of the results could outline the degree of an effect on aggressive corrosive media at the propagation of fatigue failure in steel. It has additionally been clear that corrosive aquatic media (soil and water) basically have an effect on the manner of fatigue failure propagation in steel, which have an effect on probable growth of the detected damages [11, 12].

1.3. Oil-pipelines Protection

There are many protection methods used to protect oil pipelines from corrosion resulting from the oil and its content or the external and mechanical environmental conditions accompanying the operation process. The goal of my work is to avoid the corrosion, and the following methods we can protect the pipelines from corrosion:

- lining with HDPE (high-density polyethylene),
- anti-corrosion coatings,
- electrochemical way,
- if the oil is separated from the water.

1.4. Importance of studying wettability behavior and contact angle

Wettability behavior is one of the most important topics in interfacial sciences. It is a liquid ability to preserve contact with the surface of the solid, it's come from intermolecular interactions while meeting together. It is described as solid selection to be in contact with one liquid rather than another, and if the solid does not prefer one liquid over the other, it is called intermediate-wetting or neutral-wetting, the degree of wettability is determined by the balance of surface and interfacial forces between adhesive and cohesive forces. It deals with the phases of the materials liquid, gas and solid, and the importance is clear in the combination of two materials and it is managed for other related influences, containing capillary influences [13]. A droplet takes shape on the solid substrate as a function of wetting properties (Figure 3). When a liquid drop on a solid surface (Figure 3a) forms a bead and the contact angle (θ) is higher than 90° it means non-wetting. A liquid wets a solid surface (Figure 3b) when the drop spreads on it and the contact angle is lower than 90° . Perfect wetting means the droplet spreads on the substrate and the contact angle is zero (Figure 3c).

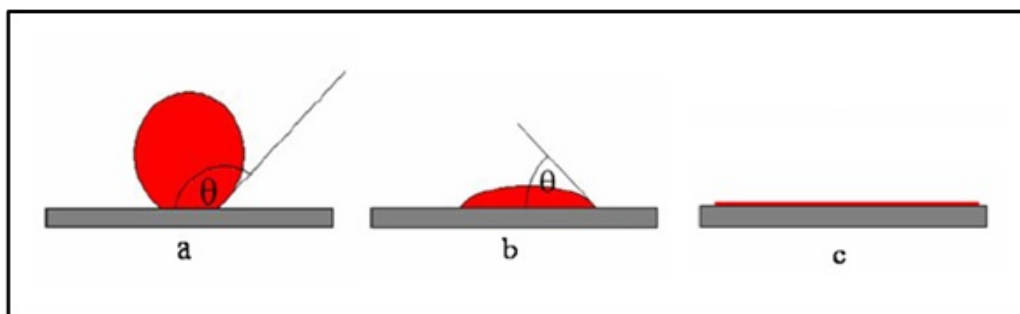


Figure 3: Liquid drop wettability and Contact angle on the solid surface
 [Wettability: a) non-wetting, b) wetting, c) perfect wetting]

2. Experiment

In the experiment part, the samples were the substrates have dimensions (10 mm × 8 mm × 5 mm) of different types of metals include (Al, Ag, Sn, Ni, and Cu) with 99.99% purity of the metals, and ceramics (TiC and WC) were ground and polished mechanically immediately before the measurement. The substrates average surface roughness (R_a) was 0.02 μm by using a surface roughness measurement device (MARSURF M 40).

Research Contact angle measurement is a widely used technique to assess the wetting behavior of liquids on solid surfaces. Sessile drop and captive bubble techniques, are employed to determine the contact angle, wetting in-sights into the wetting characteristics of oils on metal surfaces. In the contact angle measurement, by using an automatic pipette a drop of 5 μl of two types of oil include (Hydraulic oil (HME10) from Mol group company, Petroleum from Mol group company) was placed on the surface of a polished substrate for 5 minutes for each sample, then used a CCD camera to record the changing in the silhouettes of the formed drop. The CCD camera is connected to the computer, were installed KSV software (CAM2008, KSV Instruments Ltd., Helsinki, Finland) to determine the worth of the contact angle.

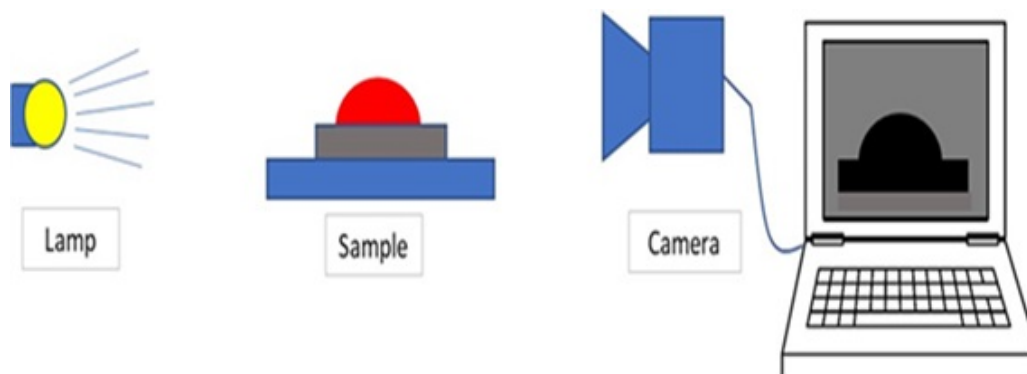


Figure 4: Equipment for the contact angle measurement.

3. Results and discussion

Depending on the results listed in Table 2 obtained of experiments, the contact angle on metal surfaces approaches zero value after 3-4 seconds it has a very high speed of liquid expansion and diffusion on all types of metal surfaces, and the wettability of petroleum was better than other oils we used on all types of substrates (for example on Ag surface, $\Theta_{\text{petroleum}} = 9^\circ$, but $\Theta_{\text{hydraulic}} = 17^\circ$) and these differences depend on the balance between adhesive forces (between the oil and the metal) and cohesive forces (within the oil). Furthermore, the gradual escalation in the oil proportion within the hydraulic system in turn decelerates the rate of its expansion. Although this effect is confined to a consistent trajectory on the surface, it underscores the

potential to influence oil wettability either through custom mixtures or, alternatively, by considering the type of metal surface in question, paves to enhance the wetting behavior, this could involve the addition of metallic coatings derived from alternative metals with superior wetting characteristics.

Table 2: The measured contact angle of the liquids on the metal surfaces.

	Liquid	Al	Ni	Cu	Sn	Ag	TiC	WC
Contact angle θ°	hydraulic	17	15	20	19	17	17	15
	petroleum	9	8	11	11	9	9	8

The different types of oils have varying chemical compositions, which influence their intermolecular forces and surface tension. Some oils have low surface tension and strong adhesive forces, allowing them to spread easily over the metal surface and exhibit good wetting. In Figure 5 shows how the difference in oil composition could affect wettability behavior on the surface, where the results show that increasing the hydraulic wetting when increasing petroleum percentage to the oil.

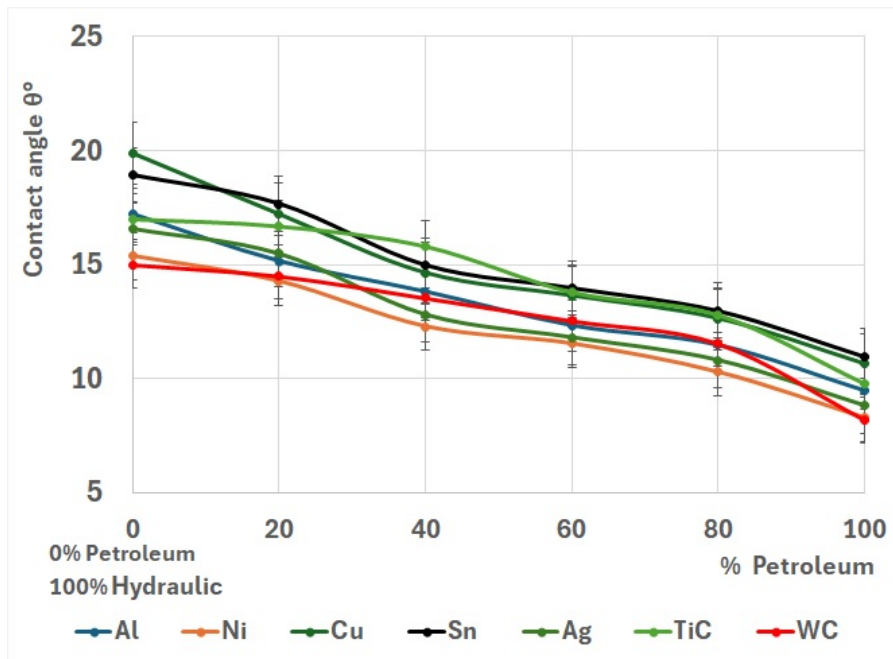


Figure 5: The Wettability behavior of different percentages of the oil petroleum droplet composition during 2 seconds.

4. Conclusion

This study explores wettability through the examination of two types of oil (Petroleum and Hydraulic oil (HME10) from Mol group company) which were applied to a range of distinct samples: (Al, Ag, Sn, Ni, and Cu), and two types of ceramics (TiC and WC). The findings are as follows:

- Ni exhibit superior oil wetting, displaying consistently lower contact angles throughout the entire duration of testing. This distinction can be attributed to oxide formation on the other metals surface, resulting in decreased surface energy and decrease the wettability.
- Petroleum oil demonstrates remarkably rapid wetting compared to distilled water in other studies. These novel observations could find applications in water-oil separation processes.
- Enhanced wetting efficiency could potentially be achieved through modifications in surface characteristics.

5. References

- [1] Dardor, Dareen, et al. 'Protocol for Preparing Synthetic Solutions Mimicking Produced Water from Oil and Gas Operations.' *ACS omega* 6.10 (2021): 6881-6892.
- [2] Montgomery, Carl T., and Michael B. Smith. 'Hydraulic fracturing: History of an enduring technology.' *Journal of Petroleum Technology* 62.12 (2010): 26-40.
- [3] Zheng, Weiwei, et al. 'Advanced materials with special wettability toward intelligent oily wastewater remediation.' *ACS Applied Materials & Interfaces* 13.1 (2020): 67-87.
- [4] Schultz, N. 'Canadian Association of Petroleum Producers presentation to the Propane Gas Association of Canada' *TransPosium 2001*. (2001).
- [5] Marafi, A., H. Albazzaz, and Mohan S. Rana. 'Hydroprocessing of heavy residual oil: Opportunities and challenges.' *Catalysis Today* 329 (2019): 125-134.
- [6] Speight, J. G., and C. R. C. Press. 'The chemistry and technology of petroleum.' (1999): 298-300.
- [7] Dmytrakh, I. M. 'On corrosion fatigue initiation from notches and the local corrosion fracture approaches.' *Notch Effects in Fatigue and Fracture*. Springer, Dordrecht, 2001. 331-346.
- [8] Nykyforchyn, H. M., and O. T. Tsyryl'nyk. 'Specific features of the in-service bulk degradation of structural steels under the action of corrosive media.' *Strength of materials* 41.6 (2009): 651-663.

- [9] Panasyuk, V. V. 'Fracture mechanics and strength of materials: advances and prospects.' *Materials Science* 40.3 (2004): 305-319.
- [10] Al-mashhadani, Mohammed H., et al. 'Inhibition of corrosion: mechanisms and classifications in overview.' *Al-Qadisiyah Journal Of Pure Science* 25.2 (2020): 1-9.
- [11] Pustovoi, V. M., and I. O. Reshchenko. 'Modeling of the in-service degradation of steels of cargo seaport structures under the laboratory conditions.' *Materials Science* 48.5 (2013): 561-568.
- [12] Khoma, M. S. 'Application of electrochemical methods to the investigation of corrosion fatigue of metals.' *Materials Science* 36.1 (2000): 80-86.
- [13] Carpenter, Chris. 'A study of wettability-alteration methods with nanomaterials application.' *Journal of Petroleum Technology* 67.12 (2015): 74-75.



**WIR BRAUCHEN DICH
FÜR UNSER
STAHL- UND WALZWERK**

WWW.FERALPI-STAHL.COM

Comparative study of the influence of selected trace elements on the phase transformation in medium-carbon steels

I. Gruber^{1*}, J. Cejka¹, and S. K. Michelic¹

¹ Christian Doppler Laboratory for Inclusion Metallurgy in Advanced Steelmaking, Montanuniversitaet Leoben, 8700 Leoben, Austria.

* Corresponding author: isabell.gruber@unileoben.ac.at

By 2017, the steel industry was the single biggest global emitter of industrial CO₂ emissions with 7% of all energy-related emissions worldwide [1]. In the EU, it is responsible for over 5% of total CO₂ emissions [2]. However, in order to comply with the European Commission's Green Deal and reduce CO₂ emissions by 55% compared to 1990 until the year 2030 and to reach net neutrality by 2050, it is necessary to transform the European iron and steel industry towards a more sustainable, scrap-based electric arc furnace-route [3, 4]. Increased amounts of various trace elements, such as copper and molybdenum, compared to the traditional integrated route pose a very important challenge here, affecting the steels' properties and thus the performance of the finished steel products. In order to gain more knowledge about these effects, medium-carbon steels were alloyed with different amounts of trace elements and subjected to various testing methods. Inter alia, the steels were subjected to high-temperature quenching dilatometry. Subsequently, they were metallographically prepared and investigated under the light optical and scanning electron microscopes. Already small amounts of certain tracing elements affected the steels' surface quality during hot working. Furthermore, phase transformation during cooling was influenced even by trace amounts of various elements and thus different microstructures were found in the differently modified steels after being subjected to the same heat treatment.

1. Introduction

The iron and steel industry is responsible for 5% the EU's total CO₂ emissions [2]. Not only is a shift in energy sources to renewables necessary but the reduction of iron ore to hot metal via the traditional blast furnace / basic oxygen furnace (BF-BOF) route in itself is a very CO₂ intensive process due to the use of coke as reduction agent [4]. Estimations by Broadbent [5] in 2016 projected that steel production from scrap via the electric arc furnace (EAF) route could potentially reduce CO₂ emissions by up to 75%.

However, increased usage of this aggregate leads to accumulation of certain elements – alloying or tramp – in the steel in circulation over time [4] which can lead to affected material properties. Copper and nickel are known to be so-called austenite stabilizing elements which means that the austenitic area in a phase diagram is expanded while at the same time the ferritic area is diminished [6]. Molybdenum, on the other hand, is a ferrite stabilizer [7]. Tin is not known to stabilize any single phase but influences a steel's microstructure in various other ways, such as interactions between precipitates and matrix interface or affecting the recrystallization start

temperature [7–10]. Furthermore, Trzaska et al. [11] postulate that critical temperatures of steels during cooling are affected by even small amounts of, inter alia, nickel, molybdenum, and copper.

Therefore, cooling behavior of medium-carbon steels with trace amounts of copper, nickel, tin, and molybdenum was observed in this work. Subsequently, the steels' resulting microstructures were investigated using light optical and scanning electron microscopy.

2. Materials and methods

In this study, two different low-alloyed medium-carbon steels were used as base materials and alloyed with varying amounts of the elements copper, tin, nickel, and molybdenum. The base steels were 42CrMo4 and 30MnVS6.

All samples were heated to 900 °C and then quenched using a TA Instruments DIL805 A dilatometer (Delaware, USA). The unmodified samples were quenched using different cooling rates of 500 K/s, 50 K/s, 5 K/s and 0.5 K/s. The modified 42CrMo4 samples were quenched with a cooling rate of 0.5 K/s. In Table 1 the different modifications of the 42CrMo4 base steel, their respective cooling rates and their respective name for easier differentiation are shown.

Table 1: Modifications of 42CrMo4 with their respective names.

Alloying element added	Modification name	Cooling rates [K/s]
–	Alloy 1	500, 50, 5, 0.5
+ 0.50 wt –% Cu	Alloy 1-Cu050	0.5
+ 0.20 wt –% Ni	Alloy 1-Ni020	0.5
+ 0.025 wt –% Sn	Alloy 1-Sn0025	0.5

The modified samples of 30MnVS6 were quenched with 5 K/s. In Table 2 the modifications of the 30MnVS6 steel, their respective cooling rates and their respective names are given.

Table 2: Modifications of 30MnVS6 with their respective names.

Alloying element added	Modification name	Cooling rates [K/s]
–	Alloy 2	500, 50, 5, 5
+ 0.50 wt –% Cu	Alloy 2-Cu050	5
+ 0.20 wt –% Ni	Alloy 2-Ni020	5
+ 0.025 wt –% Sn	Alloy 2-Sn0025	5
+ 0.04 wt –% Mo	Alloy 2-Mo004	5
+ 0.08 wt –% Mo	Alloy 2-Mo008	5

The quenched specimens were embedded in electroconductive resin, ground on silicon carbide paper in grit size of 180, 320, 600 and 1200 and erosively polished with diamond suspension with a diamond particle size of 9 μm and 3 μm . The last metallographic preparation step was chemical polishing with OPS suspension. The samples were color etched with Beraha I etching solution which consists of diluted hydrochloric acid (6%), ammonium hydrogen bifluoride, and potassium bisulfite solved in distilled water.

3. Results

3.1. Dilatometry

During dilatometry, the length and thus length change of the specimens as well as sample temperature are measured. In Figure 1 specimen length of the differently quenched unmodified 42CrMo4 samples as well as their respective first derivative is shown.

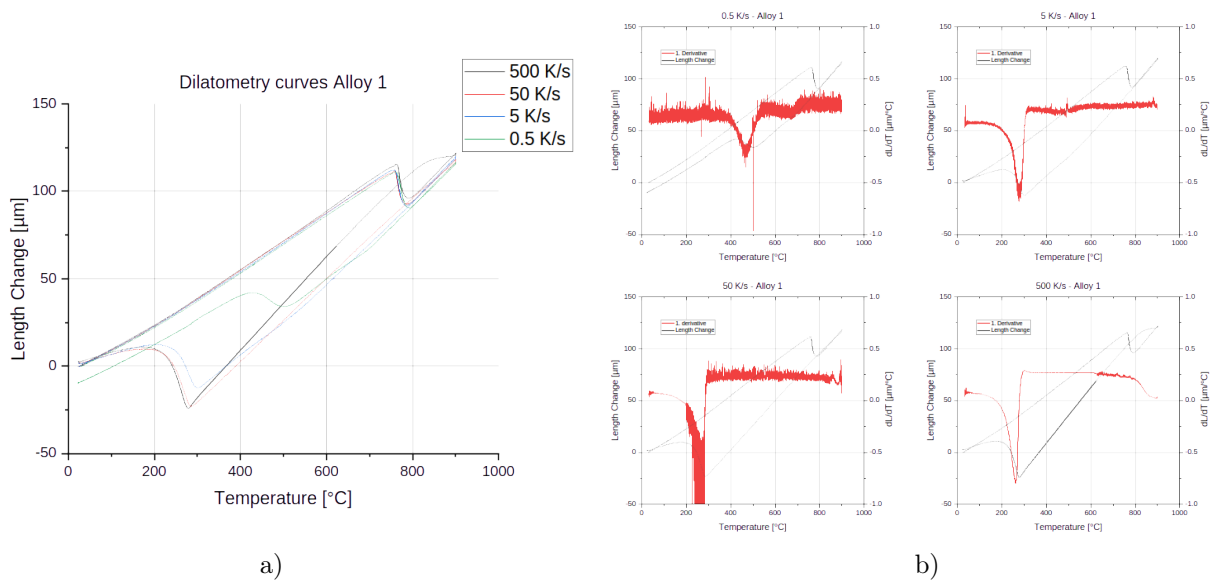


Figure 1: Dilatometry curves (a) and their respective first derivatives (b) of unmodified 42CrMo4.

It can be seen that the curves of the cooling rates of 500 K/s, 50 K/s and 5 K/s do not show much variation, and only the curve for cooling with 0.5 K/s differs from the other three and also the first derivatives show that phase transformation for the 500, 50 and 5 K/s curves set in rather late in the martensite region. Only at 0.5 K/s, phase transformation starts earlier which was why 0.5 K/s was selected as cooling rate for the modified 42CrMo4 steels. In Figure 2 the dilatometry curves and their first derivatives of the differently alloyed 42CrMo4 modifications cooled with 0.5 K/s are given.

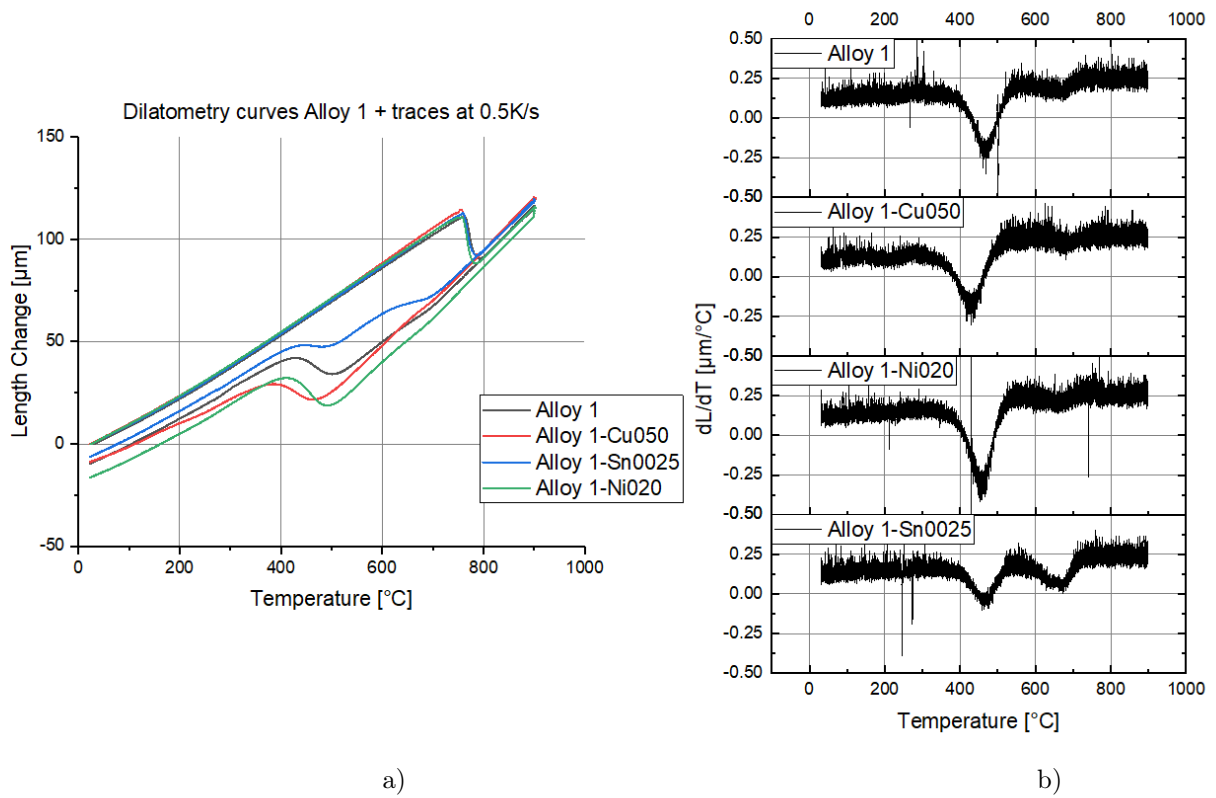


Figure 2: Dilatometry curves (a) and their first derivatives (b) of the modified 42CrMo4 steels cooled with 0.5 K/s.

In Figure 3 the length change over temperature and the first derivative curves for unmodified 30MnVS6 steel quenched at different cooling rates are illustrated.

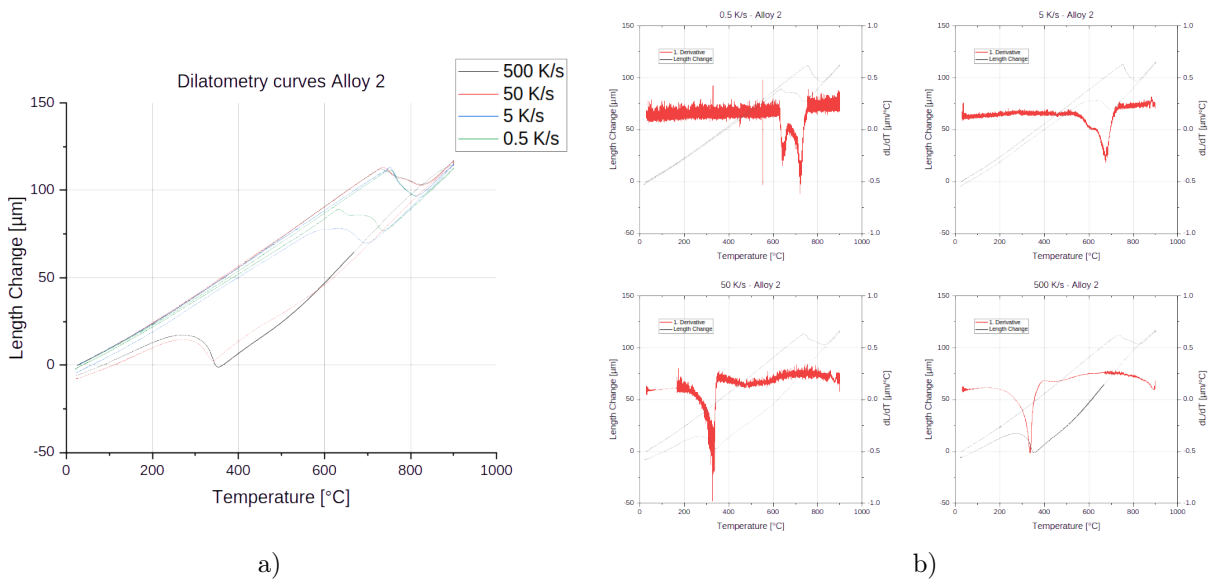


Figure 3: Dilatometry curves (a) and their respective first derivatives (b) of unmodified 30MnVS6.

The phase transformation points and thus the expected microstructure are rather similar for 500 K/s and 50 K/s as well as for 5 K/s and 0.5 K/s, respectively. This is why for the modified alloys of 30MnVS6 a cooling rate of 5 K/s was selected. In Figure 4 the dilatometry curves and their respective first derivatives of the modified 30MnVS6 samples are depicted.

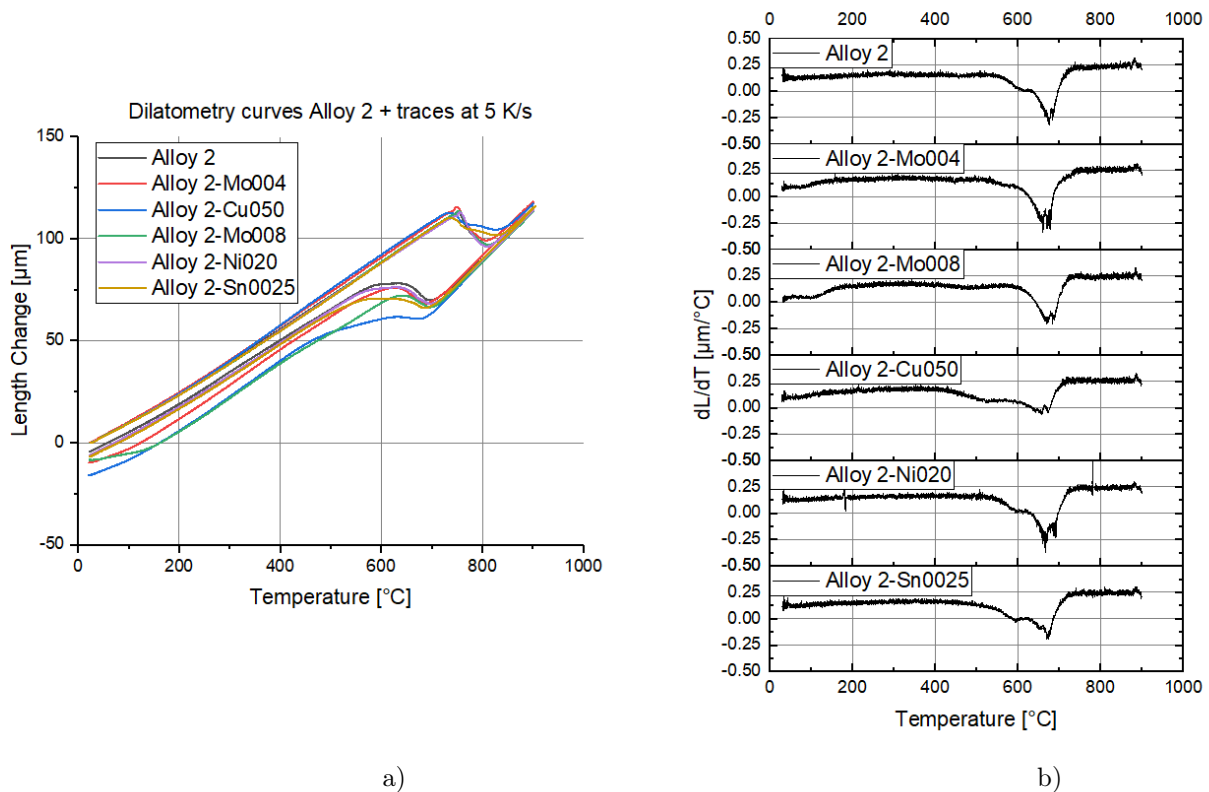


Figure 4: Dilatometry curves (a) and their first derivatives (b) of the modified 30MnVS6 steels cooled with 5 K/s.

3.2. Microstructure

The etched samples were examined under the light microscope for quantitative phase characterization. In Table 3 the findings of the light microscopic investigations are listed.

For certain modifications of 30MnVS6 the phase distribution was not exactly quantifiable under the light microscope which led to a scanning electron microscopy (SEM) investigation with a backscattered electron (BSE) and a secondary electron (SE) detector in a JEOL 7200F (JEOL Ltd., Akishima, Japan), coupled with the Aztec 6.0 (Oxford Instruments NanoAnalysis, UK) software. Exemplarily, the SE image of Alloy 2-Cu050 and its elemental mappings of iron and carbon, respectively, are given in Figure 5.

Table 3: Quantitative phase analysis under the light microscope.

	42CrMo4 – Alloy 1	30MnVS6 – Alloy 2
Blind 500 K/s	Martensite: 100 %	Martensite: 95 – 100 % Ferrite: < 5 %
Blind 50 K/s	Martensite: 100 %	Martensite: 90 – 95 % Ferrite: 5 – 10 %
Blind 5 K/s	Martensite: > 95 % Ferrite: < 5 %	Martensite: 75 – 80 % Pearlite: 20 – 25 %
Blind 0.5 K/s	Bainite: ~ 85 % Ferrite: < 10 % Pearlite: < 10 %	Ferrite: ~ 80 % Pearlite: ~ 20 %
+ Cu 0.50	Bainite: ~ 90 % Ferrite: < 10 % Pearlite: 5 – 10 %	Ferrite & Pearlite not precisely quantifiable
+ Ni 0.20	Bainite: 80 – 85 % Ferrite: < 15 % Pearlite: < 10 %	Ferrite: ~ 85 % Pearlite: ~ 15 %
+ Sn 0.025	Bainite: 85 – 90 % Ferrite: 5 – 10 % Pearlite: ~ 5 %	Bainite: < 5 % Ferrite: 80 – 85 % Pearlite: ~ 15 %
+ Mo 0.04		Ferrite & Pearlite not precisely quantifiable
+ Mo 0.08		Ferrite & Pearlite not precisely quantifiable

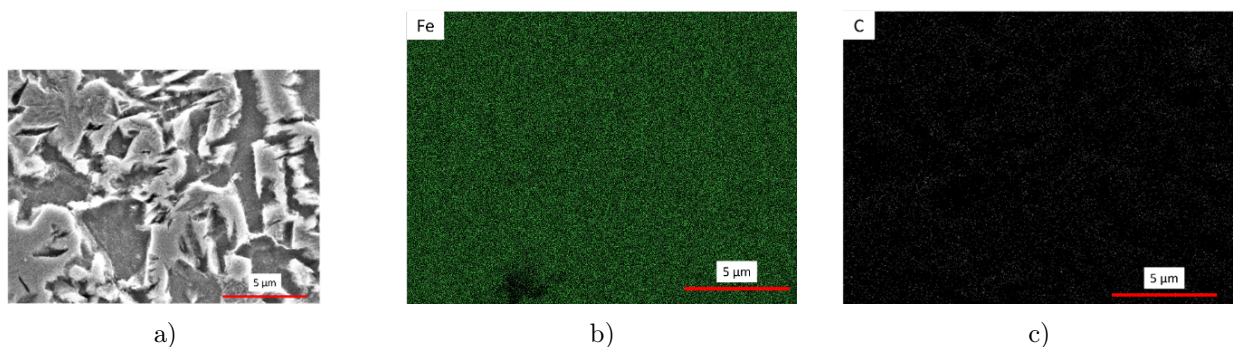


Figure 5: SE image (a) and BSE elemental mappings of iron (b) and carbon (c) of Alloy 2-Cu050.

4. Discussion

From Table 3 and the phase transformation curves, it is apparent that minimal amounts of certain tramp elements already influence phase transformation at a given cooling rate.

Copper delays phase transformation already after an addition of 0.50 wt-% to 42CrMo4. The 30MnVS6 steel with an addition of 0.50 wt-% could not be accurately quantified under the light microscope. SEM measurements showed that the size of the microstructure was in the micrometer range. The brighter areas in a SE image are higher than the darker areas, indicating that the material has been selectively etched. The transformation curve and its first derivative suggest that the microstructure is ferritic-pearlitic. The elemental mapping of iron does not show any variation in iron distribution over the sample area. On the other hand, the carbon mapping shows a network-like structure matching the lighter areas in the SE image, which can likely be attributed to pearlite. Beraha I etching solution forms a film on the material and thus it is logical to assume that the etching solution was too viscous to penetrate into the pearlite lamellae and instead has formed a film over the whole of the pearlitic area. However, this has not occurred for the 30MnVS6 blinds, which makes it obvious that those lamellae are wider in distance. If copper delays phase transformation, carbon has a smaller time frame to enter the cementite areas in the pearlite and thus the pearlite lamellae get narrower. This supports the notion that already trace amounts of copper delay phase transformation noticeably.

Nickel, on the contrary, does not seem to affect phase transformation at the given alloyed amounts. Neither in the 42CrMo4, nor in the 30MnVS6 modification significant influence has been observed.

Tin actually seems to have opposite effects for 30MnVS6 for which a little delay was measured and 42CrMo4 for which even a slight acceleration in phase transformation was observed. This leads to the suggestion that the amount of tin alloyed was actually too small to prompt change in phase transformation and that the observed small deviations have other reasons like slight fluctuations in various other alloying elements.

Both samples of 30MnVS6 that were alloyed with traces of molybdenum were not precisely quantifiable under the light microscope. Light microscope images as well as SEM BSE images and elemental mappings were widely consistent with those of Alloy 2-Cu0.50 which suggests that the same mechanisms were at play here. Considering that only 0.04 and 0.08 wt-% of molybdenum were alloyed to the samples, respectively, and that this was apparently enough to affect the steels' microstructure in this way, it can be concluded that even slightest amounts of molybdenum significantly delay phase transformation while cooling in medium-carbon steels.

5. Conclusion

Already trace amounts of copper and especially molybdenum seem to significantly delay phase transformation while cooling in medium-carbon steels so that the resulting microstructure is visibly different from unalloyed steel samples. Nickel's effect on phase transformation seems to be a lot less intense resulting in no noticeable influence of 0.20 wt-% nickel on the microstructure or cooling curves of the samples.

Tin was alloyed in roughly the same amounts as molybdenum but contrary to the molybdenum alloyed samples, no conclusive statements about tin's influence on phase transformation and thus the resulting microstructure can be made. This leads to the suggestion that tin's effect on the cooling behaviour of medium-carbon steels is less pronounced than for example molybdenum's and if further investigations are to be made, they should include higher amounts of tin in the steel.

Overall, the subject of secondary raw materials is a growing area of research and a lot more focus will be placed on the topic of tramp elements in steel.

Acknowledgments

The financial support from the Austrian Federal Ministry of Labour and Economy, the National Foundation for Research, Technology and Development, the Christian Doppler Research Association, and voestalpine Stahl GmbH is gratefully acknowledged.

6. References

- [1] IEA, International Energy Agency, Energy Technology Perspectives 2017.
- [2] The European Steel Association (EUROFER) AISBL, Making a success of the EU Green Deal, Brussels, 2020.
- [3] World Steel Association, Sustainability Indicators 2022: Sustainability performance Sustainability performance of the steel industry 2003-2021, 2022.
- [4] K. Daehn, Copper contamination in end-of-life steel recycling, developing a new strategy from million-tonnes to milligrams. Dissertation, 2019.
- [5] C. Broadbent, Steel's recyclability: demonstrating the benefits of recycling steel to achieve a circular economy, Int J Life Cycle Assess 21 (2016) 1658–1665.

- [6] J. Duan, D. Farrugia, C. Davis, Z. Li, Texture Development During Annealing in a Low-Carbon Formable Steel Containing Impurities from Increased Scrap Use, *Metall Mater Trans A* 54 (2023) 983–997.
- [7] V.L. J.C. Herman (Ed.), Influence of residual elements on steel processing and mechanical properties, 1996.
- [8] S. Bell, B. Davis, A. Javaid, E. Essadiqi, Final Report on Effect of Impurities in Steel: Report No. 2005-41(CF), Natural Resources Canada, 2006.
- [9] Y. KAWAMO, S. NAKASHIMA, K. TAKASHIMA, J. HARASE, Effect of Tin Addition and Condition of Inter-pass Aging in Cold Rolling on Secondary Recrystallization of Grain-oriented Electrical Steel, *Tetsu-to-Hagane* 79 (1993) 1197–1203.
- [10] S. NAKASHIMA, K. TAKASHIMA, J. HARASE, T. Kamijo, Effect of Tin Addition on Primary and Secondary Recrystallizations of Silicon Steel, *Mater. Trans., JIM* 37 (1996) 462–468.
- [11] J. Trzaska, Calculation of Critical Temperatures by Empirical Formulae, *Archives of Metallurgy and Materials* 61 (2016) 981–986.

Influence of Q & P-parameters and Al-content on the microstructural evolution of lean-medium-Mn-steels

K. Höger¹, S. Kaar-Schickinger², M. Wallner², R. Schneider¹

¹ University of Applied Sciences Upper Austria, School of Engineering, Stelzhamerstraße 23, 4600 Wels, Austria

² voestalpine Stahl GmbH, Research and Development Department, Business Unit Coil, voestalpine-Strasse 3, 4020 Linz, Austria

This report investigates the impact of different heat treatment parameters and varying Al-contents on the microstructure of Quenching & Partitioning (Q&P) steels. Therefore, three lean-medium-Mn-steels with Al-contents between 0.3 and 0.9 wt-% underwent heat treatments according to Q&P-regimes. For comparison, the steels were subjected to a TRIP-aided-bainitic-ferrite (TBF) process. In both cases, the samples were fully austenitized at 900 °C for 120s, using dilatometry. For the Q&P process, the quenching temperature (T_Q) ranged from 210 °C to 300 °C, while the TBF samples were cooled to 360 °C. Afterwards, the specimen were re-heated to the partitioning temperature (T_p) of 400 °C and isothermally held for partitioning times (t_p) of 40, 120 and 200 s. Subsequently, these steels were analyzed with regard to their phase fractions and hardness. The results indicated that in the Q&P process, the microstructure was primarily influenced by T_Q , while t_p played a minor role due to the time-independent martensitic transformation during quenching. In general, rising T_Q led to an increase in retained austenite (RA) fraction. In the TBF process, a substantial influence of t_p was found, which can be explained by the kinetics of the isothermal bainitic transformation. Regardless of the heat treatment concept, an increasing Al-content contributed to elevated RA contents.

Introduction

Advanced High Strength Steels (AHSS) draw high interest by the automotive industry due to increasing demands in fuel efficiency, CO₂-emissions and crash safety. AHSS stand out with their superior mechanical properties in terms of tensile strength and balanced formability when compared to conventional steels and are separated in three generations. The first generation contains dual-phase-(DP), complex-phase (CP), transformation induced plasticity (TRIP), martensitic and press hardened (PHS) steels. The second generation is dominated by the so-called twinning induced plasticity (TWIP) steels, which only play a minor role in today's automotive industry due to their economic inefficiencies. The third generation AHSS consists of medium-Mn, TRIP-assisted bainitic ferrite (TBF) and quenching and partitioning (Q&P) steels, of which the latter lie in the focus of this work. AHSS of the third generation excel in the mechanical properties of the first generation, without the usage of the high alloying contents of the second generation. [1–3]

To achieve a favorable combination of strength and formability, the microstructure of third generation AHSS typically consists of tempered martensite (α''), bainitic ferrite (α_B) and metastable retained austenite (RA). [2, 4] Based on the TRIP-effect, this metastable RA

transforms into martensite (α') during straining. [5, 6] For a sufficient stabilization of RA to room temperature both, chemical composition of the steel and specific annealing cycles are of great importance. RA is chemically stabilized by the austenite stabilizing elements C and Mn and indirectly by Si and Al. Although Si and Al are ferrite stabilizing elements, they suppress the formation of cementite (Fe_3C) during heat treating due to their low solubility in Fe_3C , which allows for the essential C-enrichment of RA. [7, 8]

The Q & P-annealing process starts with a full austenitization of the steel, followed by quenching to T_Q below the martensite start temperature (M_S), leading to a microstructure containing α' and untransformed austenite (γ). Subsequently, the so-called partitioning step takes place, during which C is redistributed from α' to γ . This leads to a matrix of α'' and ensures the chemical stabilization of RA to room temperature. A third phase that may be present in the microstructure of Q & P steels is α_B , which develops from γ during the partitioning step. The amount of α_B that can be formed is dependent on the amount of γ being present in the microstructure after the quenching step. [9–12] The final microstructure of Q & P steels is therefore composed of α'' , RA and small fractions of α_B .

When quenching is stopped above M_S the annealing cycle follows that of the TBF-process, in which RA is solely stabilized by C due to the formation of α_B , which develops from γ . Since the kinetics of the isothermal bainitic transformation plays an important role for this heat treatment, the progress of the microstructural evolution is significantly determined by the isothermal holding time. The microstructure of a fully austenitized TBF steel solely contains the two phases α_B and RA. [1, 13]

Material and experimental methods

Three different steels with varying Al-contents were investigated for this work. These steels were produced under laboratory conditions by voestalpine Stahl GmbH Linz, according to procedures described in [12]. The chemical composition of each steel is shown in Table 1. The Q & P heat treatment for the specimen of each steel is given in Figure 1. After a full austenitization at a temperature of 900°C for 120 s the steel is quenched to its quenching temperature T_Q and held for 10 s. The exact temperatures for T_Q are displayed in Figure 1. Afterwards, the partitioning-step was performed at a temperature of 400°C with three different partitioning times (t_p) of 40, 120 and 200 s. After the partitioning step, the steel is finally quenched to room temperature.

Table 1: chemical composition of the investigated steels in wt-%.

Steel	C	Mn	Si	Al
0.2C-3Mn-0.5Si-0.3Al	0.194	3.01	0.54	0.29
0.2C-3Mn-0.5Si-0.6Al	0.195	3.00	0.53	0.63
0.2C-3Mn-0.5Si-0.9Al	0.196	3.01	0.54	0.95

Dilatometry (BÄHR 805A/D) was used for the investigation of the first screening of the microstructural evolution during Q & P-treating. After heat treating, the RA-content was determined by saturation magnetization in a magnet yoke. The hardness was measured according to Vickers (HV1) and for the microstructural analysis the steels were etched with LePera and analyzed by means of light optical microscopy.

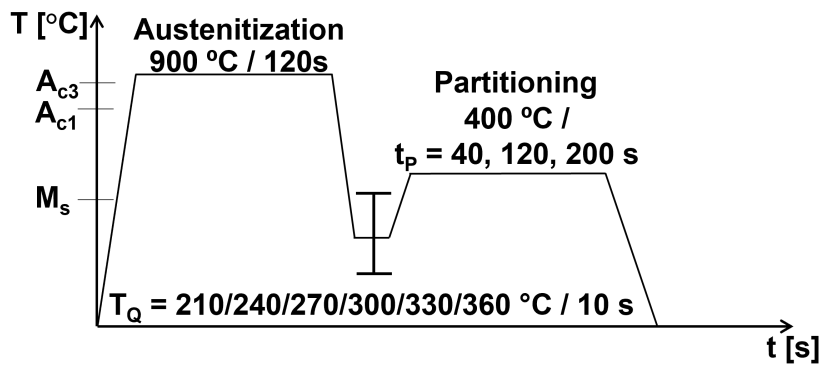


Figure 1: Time-temperature-cycles for Q & P heat treatment.

Results

Influence of the quenching temperature on the microstructural evolution and hardness

The influence of T_Q on the evolution of the microstructure and hardness is shown exemplarily for the steel 0,2C-3Mn-0,5Si-0,6Al at $t_p = 120$ s in Figure 2. When looking at the phase fractions, an increasing T_Q up to a temperature of 330 °C leads to a decrease in the portion of α'' , while both fractions of α_B and RA increase. Since a T_Q of 360 °C lies above M_S , no α' is formed during quenching, which means that this process is no longer a Q & P-cycle but a TBF one. The noticeable difference is shown in the appearance of α' . It is evident that with a rise in T_Q the hardness decreases up to the temperature of 330 °C, whereafter it increases at a temperature of 360 °C.

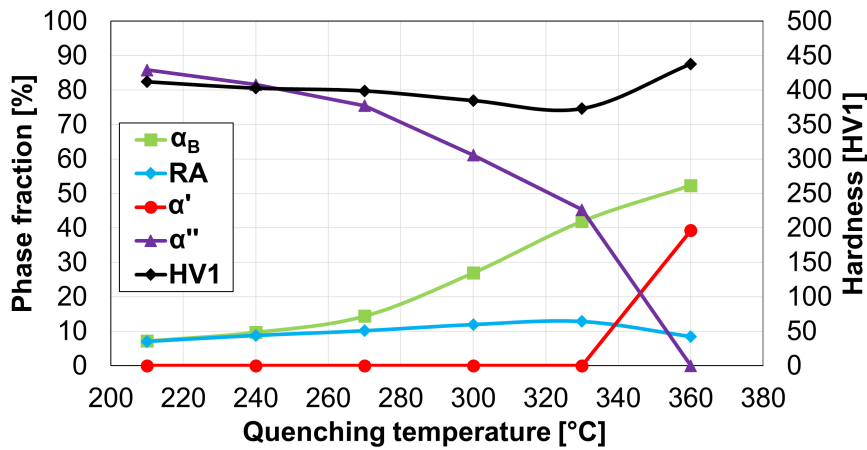


Figure 2: Phase fractions and hardness of the steel 0,2C-3Mn-0,5Si-0,6Al; $t_p = 120$ s.

Influence of the partitioning time on the microstructural evolution and hardness

For this investigation again the steel 0,2C-3Mn-0,5Si-0,6Al is used. The effect of t_p at different T_Q becomes evident when analyzing the microstructure (Figure 3 and Figure 4). For the Q & P process at $T_Q = 300$ °C and $t_p = 40$ s shown in Figure 3a), the microstructure mainly consists of α'' and α_B (blue/brown matrix) along with RA (white islands). The same appears to be the case for the microstructure of the steel that was partitioned for 200 s (Figure 3b)). Regarding the hardness of the two specimen, no significant influence of an elevated t_p is visible.

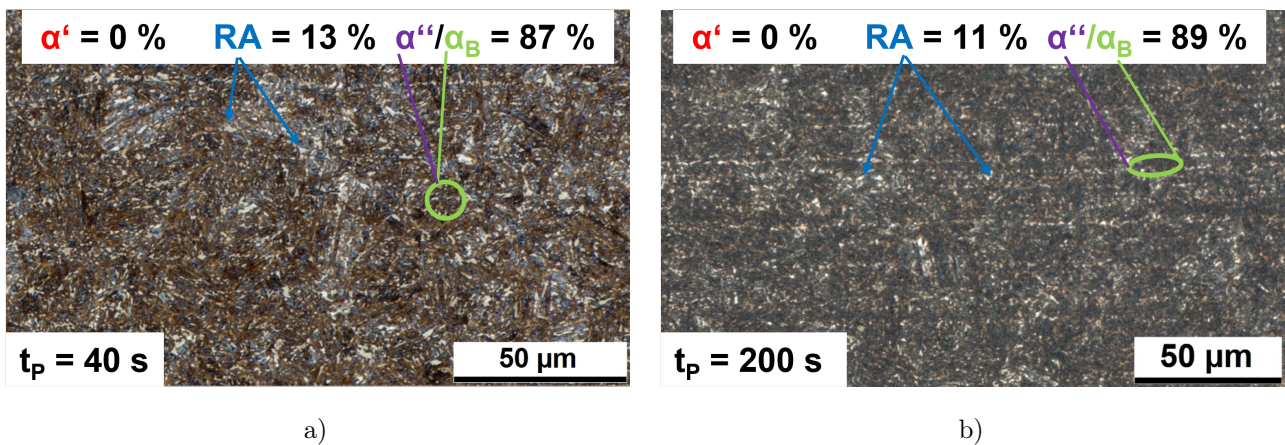


Figure 3: Influence of t_P for the steel 0,2C-3Mn-0,5Si-0,6Al for $T_Q = 300$ °C and $t_p =$ a) 40 s, b) 200 s.

The microstructural evolution for the TBF process at $T_Q = 360$ °C is shown in Figure 4a) and b). With shorter t_p , i.e. 40 s a large amount of α' (brown needles) is found after annealing as well as a small amount of RA (white islands), while the rest of the microstructure is composed of α_B (blue needles). By elevating t_p to 200 s the amount of α_B and RA increases while the amount of α' significantly declines, which is accompanied by a reduction in hardness.

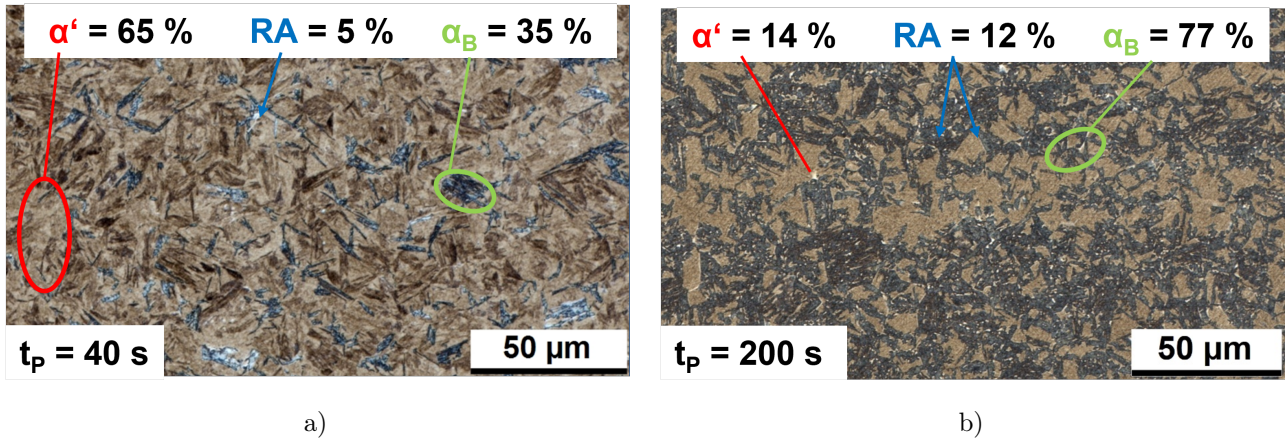


Figure 4: Influence of t_P for the steel 0,2C-3Mn-0,5Si-0,6Al for $T_Q = 360\text{ }^\circ\text{C}$ and $t_p =$ a) 40 s, b) 200 s.

Influence of the Al-content on the microstructural evolution and hardness

The effect of Al on the phase fractions is shown in Figure 5a) and b) for the steels 0,2C-3Mn-0,5Si-0,3Al and 0,9Al with $t_p = 120$ s, respectively. For both steels it appears that with rising T_Q the reduction of the α'' -fraction is accompanied by an increase of α_B and RA. For the steel containing 0.3 wt-% the results of the dilatometric study show that in case of a T_Q of $330\text{ }^\circ\text{C}$ a small portion of α' is formed during final cooling, which increases for a T_Q of $360\text{ }^\circ\text{C}$ (TBF-process). The steel with 0.9 wt-% Al does not show any α' formation during Q & P heat treating ($T_Q \leq 330\text{ }^\circ\text{C}$), whereas at the maximum T_Q of $360\text{ }^\circ\text{C}$ (TBF-process) α' is also present in the microstructure after heat treating.

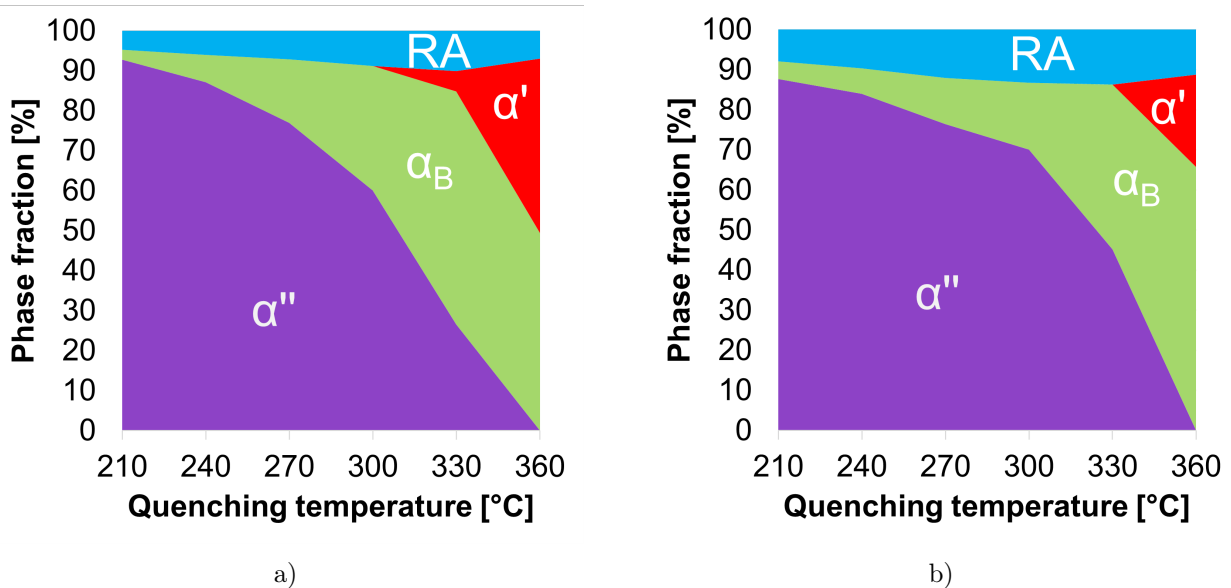


Figure 5: Phase fractions of a) 0,2C-3Mn-0,5Si-0,3Al, b) 0,2C-3Mn-0,5Si-0,9Al; $t_p = 120$ s.

Figure 6a) displays the RA-contents as a function of T_Q for the investigated steels with varying Al-content. In general, a slight increase in RA-fraction is visible when elevating the Al-content. Furthermore, all steel grades show a similar trend regarding the T_Q -influence. In particular, an increase in RA is observed when raising T_Q until a temperature of 330 °C. At 360 °C the RA-fraction decreases. The effect of the Al-content on the hardness of each steel is depicted in Figure 6b). All three steels show a loss in hardness when increasing T_Q up to 330 °C. The most pronounced difference is shown at $T_Q = 360$ °C, where the steels with 0,3 and 0.6 wt-% Al have a slightly higher hardness increase than the steel with 0.9 wt-% Al.

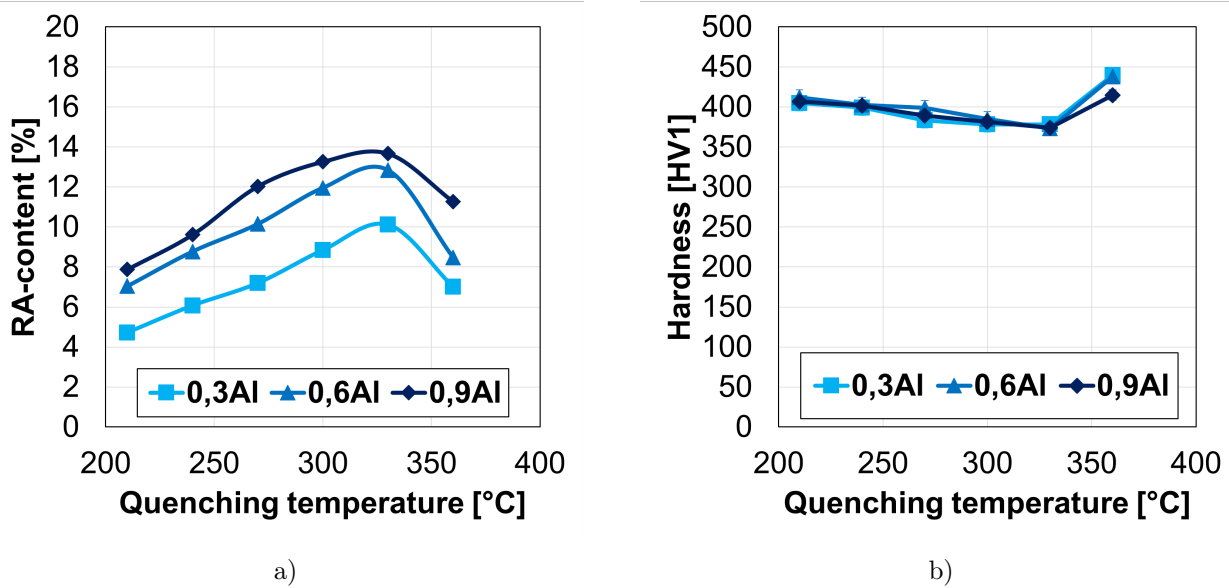


Figure 6: a) RA-content as a function of TQ for different Al-contents, b) Hardness as a function of TQ for different Al-contents; $t_p = 120$ s.

Discussion

In agreement with [10, 11, 13], the decreasing amount of α'' and increasing fractions of RA and α_B with rising T_Q are ascribed to the declining difference between T_Q and M_S . The smaller difference between these two temperatures leads to a smaller portion of α' and larger portion of untransformed austenite after quenching, which is then able to be stabilized via C-partitioning or transformed into α_B . The declining hardness can be explained by an increase of α_B and a decrease in the α'' -fraction for the Q & P-cycles with higher T_Q , which correlates with the results in [12]. There is no direct relation between the RA-fraction and the hardness of the steels, since otherwise there would be a difference in hardness between the three Al-alloyed different steels in their Q & P-cycles. The growth in hardness for $T_Q = 360$ °C is related to the formation of α' upon final cooling. Since the α' -fraction for the steel with 0.9 wt-% Al is the smallest at that temperature, it aligns with the lower hardness increase. On the contrary, the lower Al-alloyed steels reach the highest hardness due to the largest amounts of fresh martensite (α').

Comparing the different t_P of the Q & P-cycles, the results show that there is no noticeable influence of t_P in the investigated range between 40s and 200s on the overall phase fraction. The amount of RA is predominantly determined by T_Q , while the process of chemical RA stabilization is rapidly completed due to the short distances that C needs to diffuse from α' into γ , which is in agreement with the results from [9] and [13]. While t_P does not have a significant influence on the microstructural evolution during the Q & P-process, a pronounced effect can be seen for the TBF-process ($T_Q = 360^\circ\text{C}$), which can be related to the kinetics of the $\gamma \rightarrow \alpha_B$ transformation. With an increase in t_P the fraction of α_B and RA significantly increases, thus the amount of α' declines, which correlates with the results from [1] and [13]. Nonetheless the results show that a t_P of 200s does not suffice to fully stabilize the existing γ to room temperature and therefore avoid the development of α' in case of the TBF-process.

Summary

In this work the influence of varying Al-contents as well as two different heat treatment parameters in form of the T_Q and t_P for a Q & P-annealing cycle on the microstructural evolution and hardness were investigated. The following main conclusions were found:

- The final microstructure after Q & P processing is primarily determined by T_Q . The higher T_Q , the larger the RA and α_B fractions due to the decreasing α'' content. Higher T_Q lead to a reduced hardness of the steel.
- The t_P has no significant influence on the development of the microstructure in the Q & P-process, whereas it is of significant importance for steels gained through a TBF-process. In later case an elevated t_P leads to increased α_B and RA fractions and a reduced amount of α' , resulting in reduced hardness.
- An increasing Al-content shows its influence through the stabilization of a higher amount of RA after Q & P and TBF-annealing cycles. In the case of the TBF-cycles, a rise in Al furthermore contributed to lower fractions of α' , resulting in lower hardness values.

Acknowledgments

The authors sincerely acknowledge the support of the Austrian Research Promotion Agency (FFG) related to the frontrunner project No. 860188 'Upscaling of medium-Mn-TRIP-Steels'. The authors thank voestalpine Stahl GmbH in Linz for providing materials and the support of the research center. The support of the University of Applied, Faculty of Engineering and Applied Sciences in Wels is gratefully acknowledged.

References

- [1] N. Fonstein, *Advanced High Strength Steels // Advanced high strength sheet steels. Physical metallurgy, design, processing, and properties*, Springer, Cham, Heidelberg, New York, Dordrecht, London, 2015.
- [2] D. K. Matlock, J. G. Speer, *Processing Opportunities for New Advanced High-Strength Sheet Steels*, *Materials and Manufacturing Processes*, 25 (2010), 1-3, S. 7–13, DOI: 10.1080/10426910903158272.
- [3] D. Matlock, J. G. Speer, E. de Moor, P. J. Gibbs, *Recent developments in advanced high strength sheet steels for automotive applications: An overview*, *Jestech*, 15 (2012), 1, S. 1–12.
- [4] H. Y. Li, X. W. Lu, X. C. Wu, Y. A. Min, X. J. Jin, *Bainitic transformation during the two-step quenching and partitioning process in a medium carbon steel containing silicon*, *Materials Science and Engineering: A*, 527 (2010), 23, S. 6255–6259, DOI: 10.1016/j.msea.2010.06.045.
- [5] M. Soleimani, A. Kalhor, H. Mirzadeh, *Transformation-induced plasticity (TRIP) in advanced steels: A review*, *Materials Science and Engineering: A*, 795 (2020), 140023, DOI: 10.1016/j.msea.2020.140023.
- [6] W. Bleck, X. Guo, Y. Ma, *The TRIP Effect and its Application in Cold Formable Sheet Steels*, *Steel research international*, 88 (2017), 10, 1700218, DOI: 10.1002/srin.201700218.
- [7] H. Xue, T. N. Baker, *Influence of aluminium on carbide precipitation in low carbon microalloyed steels*, *Materials and Technology*, 9 (1993), 5, S. 424–429, DOI: 10.1179/mst.1993.9.5.424.
- [8] K. Zhu, H. Shi, h. Chen, C. Jung, *Effect of Al on martensite tempering: comparison with Si*, *Journal of Materials Science*, 53 (2018), 9, S. 6951–6967, DOI: 10.1007/s10853-018-2037-6.
- [9] S. Samanta, S. Das, D. Chakrabarti, I. Samajdar, S. B. Singh, A. Halder, *Development of Multiphase Microstructure with Bainite, Martensite, and Retained Austenite in a Co-Containing Steel Through Quenching and Partitioning (Q & P) Treatment*, *Metallurgical and Materials Transactions A*, 44 (2013), 13, S. 5653–5664, DOI: 10.1007/s11661-013-1929-y.
- [10] F. Peng, Y. Xu, D. Han, X. Gu, *Kinetic models of multiple-stage martensite transformation and subsequent isothermal bainite formation excluding ϵ -carbide precipitation in intercritical quenching and partitioning steels*, *Materials & Design*, 183 (2019), 24, 108183, DOI: 10.1016/j.matdes.2019.108183.

- [11] D. P. Koistinen, R. E. Marburger, A general equation prescribing the extent of the austenite-martensite transformation in pure iron-carbon alloys and plain carbon steels, *Acta Metallurgica*, 7 (1959), 1, S. 59–60, DOI: 10.1016/0001-6160(59)90170-1.
- [12] M. Wallner, K. Steineder, R. Schneider, C. Commenda, C. Sommitsch, Effect of galvannealing on the microstructural and mechanical properties of a Si and Al alloyed medium-Mn quenching and partitioning steels, *Materials Science and Engineering: A*, 841 (2022), 143067, DOI: 10.1016/j.msea.2022.143067.
- [13] S. Ebner, C. Suppan, R. Schnitzer, C. Hofer, Microstructure and mechanical properties of a low C steel subjected to bainitic or quenching and partitioning heat treatments, *Materials Science & Engineering: A*, 735 (2018), 26, S. 1–9, DOI: 10.1016/j.msea.2018.08.026.

Analysis of the impression die forging process of a forging model with elongated shape

Paulina Kała¹, Adrian Bednarczyk¹, Aneta Łukaszek – Sołek¹, Grzegorz Ficak^{1,2}

¹ Faculty of Metals Engineering and Industrial Computer Science, AGH University of Science and Technology

² GK FORGE SP Z O.O. ul. Przemysłowa 10, 43 – 400 Goleszów

The subject of the paper is the analysis of the forging process of a model elongated-shaped forging. The purpose of the work is to design the correct tool geometry resulting in an increase in tool life. The first part of the paper is devoted to literature analysis. The characteristics and division of die forging processes are presented taking into account the methods of filling blanks. Subsequently, the stages of designing elongated forgings are presented, among others methods of making elongated forgings as well as determining the dimensions of the starting material. At the end of the literature part, defects and the concept of durability of dies are discussed. The second part of the paper corresponds to conducted research. It begins with an analysis of the currently used technology in the forge. Maps of the distribution of effective stress, mean stress and elastic strain of tools were analyzed. Based on this, a new pre-cut geometry with better durability was proposed. The last part is devoted to the summary and conclusions.

Keywords: forging dies, die forging, tools, stress, durability

1. Introduction

A wide range of metalworking processes are widely used in the production of various everyday products. This field also includes the so-called ‘Deep processing of metal products’, which is used to manufacture products with specific functional properties such as sheets, forgings, bent profiles, stamped parts for car bodies, or household appliances [1]. Die forging is a traditional method of metal forming that has been used for centuries. This process has evolved with technological progress and continues to play a key role in the production of high-quality metal components. Forged parts are commonly used in various products such as machinery, tools, and everyday items. Among the various types of forged components, die forgings are particularly significant. Their share in production depends on the type of product, scale of production, and manufacturing method. It can range from 50 to 80 % [2].

The scope of the work included an analysis of the forging process of a modelled elongated shape, during which failure of the die impression occurred due to the formation of cracks. A solution to the problem was proposed in the form of a modified geometry of the preliminary die impression, which reduces stresses both in the preliminary and final die. As a result of the introduced changes, cracks ceased to form. Creating a geometric model of the forging based on the technical drawing and die models was carried out using the SolidWorks program. All variants of the

forging processes were performed in the QForm program, which allows to accurately predict phenomena's occurring during processes where plastic deformation is significant.

2. Research Part

2.1. Material

The material used for the forging is steel S235J0 in a normalized state. The utilized steel is non-alloy steel. Steel S235J0 is widely used in various engineering projects in both land and water engineering [3].

The material used for the dies is steel X37CrMoV51 (according to PN-EN ISO 4957:2004). This type of alloy steel is characterized by high hardenability, good resistance to thermal fatigue, tempering, and oxidation [4].

2.2. Research Methods

The forging model was created based on the technical documentation provided by the company. The model was created using the SolidWorks software.

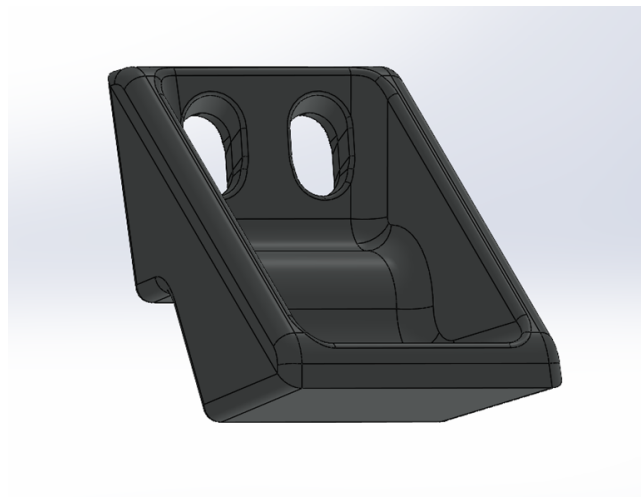


Figure 1: Forging model.

Next, the forging was prepared for the production of appropriate dies, i.e., the dimensions were scaled up by the thermal expansion value of the used material, in this case by 1.3%. Then, the holes were closed off and die impressions were made in both the upper and lower dies.

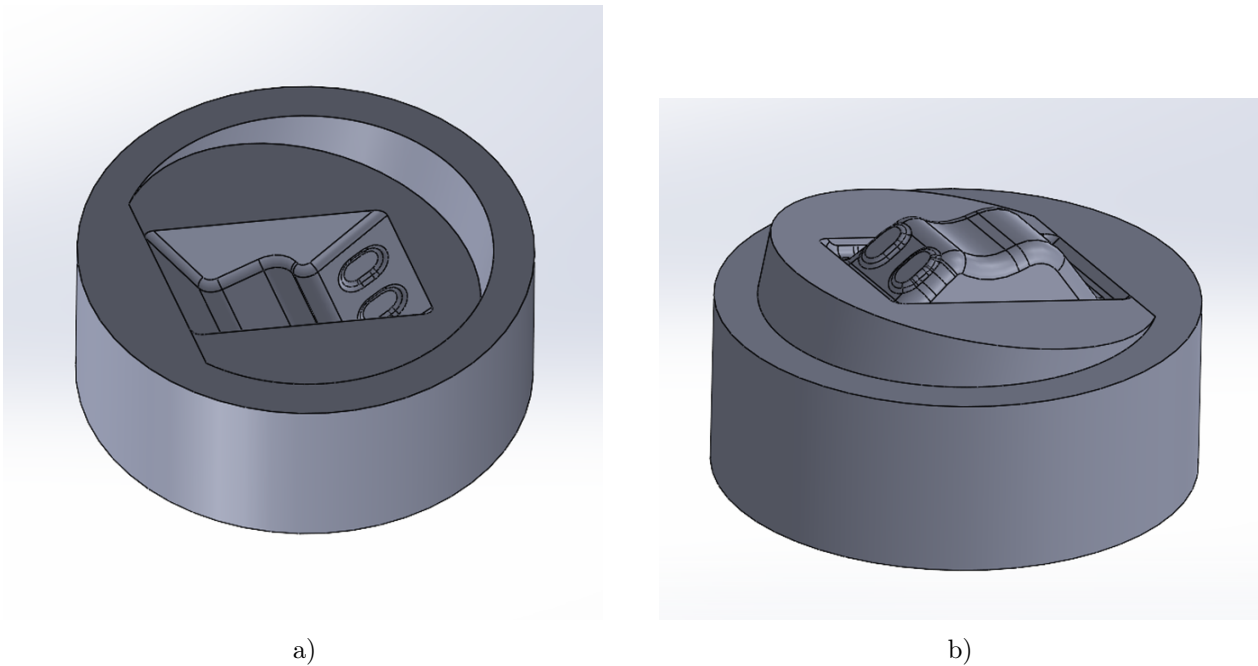


Figure 2: Die model: a) bottom die, b) top die.

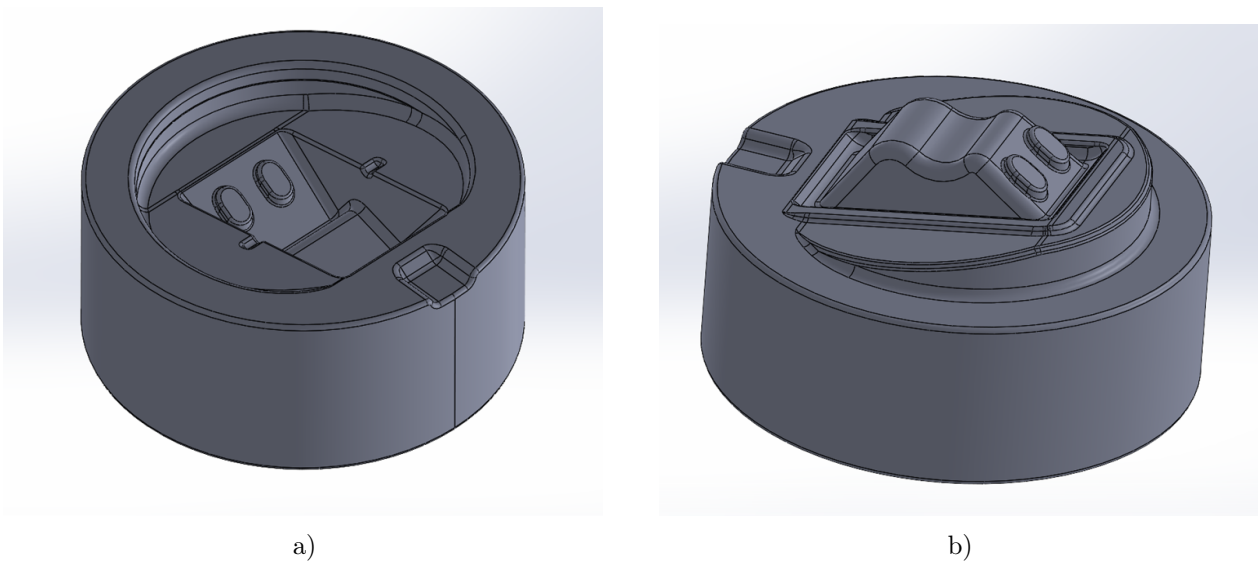


Figure 3: Die model: a) bottom die, b) top die.

Rounded edges, cutouts for tongs, and elements facilitating the leveling of the charge were added. The final dies were presented in Figure 3a) and 3b). All necessary parameters were determined using the SolidWorks software.

The first operation was swelling on the flat side surfaces of the dies to remove scale and prepare the semi-finished product for further plastic processing. Next procedure performed was flattening the material in the shaping dies. The purpose of this process was to preliminarily shape the billet to reduce stresses on both the preliminary and final dies. The dies and the billet presented in the drawings were made using the QForm 3D Qshape subprogram. The next step was the

preparation of preliminary dies. Several versions of these dies were made, however, in this work, one of them is presented, which met the project objectives.

2.2.1. Boundary Conditions

In the adopted model, the tool material was defined as X37CrMoV51 steel, and the material for the forgings as 235J0 steel. The initial temperature of the billet was set at 1050 °C. The die temperature was set at 300 °C to avoid cracking caused by too large temperature difference between tools and the billet. The forging process was carried out on a mechanical press with maximum load 16 MN, using a graphite-based emulsion lubricant with a friction coefficient of 0.4. Forging takes place without a protective atmosphere at a temperature of 20 °C. The end of forging was set at a height of 2 mm.

2.2.2. Analysis of Results

The presented results are for the final dies. All drawings analyzed are presented for the time instant at which the force exerted on the forging material is maximum. Analyzed the simulation results of the forging process employed in the forge. The first analyzed parameter was the mean stresses, which is the arithmetic mean of three principal stresses at a given point. This can be interpreted as their simplification allowing to calculate the stress tensor describing the hydrostatic state and the deviator stress tensor describing pure shear.

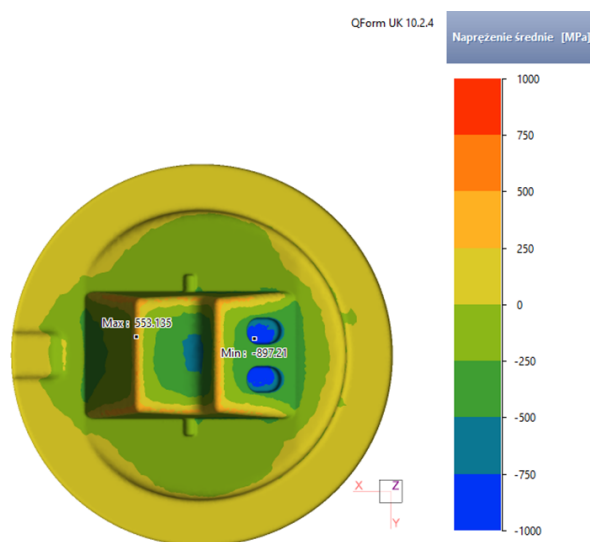


Figure 4: Mean stresses in the final die.

It was found that the highest values of mean stresses are within an acceptable range up to 1670 MPa, indicating that the die should not be damaged. They are located in areas of small fillets and slight wall inclinations.

Next, stress intensity was analyzed, i.e., the total effective stress, which can be defined as the uniaxial stress that causes the same material strain at a given point in the body as the combined stress state.

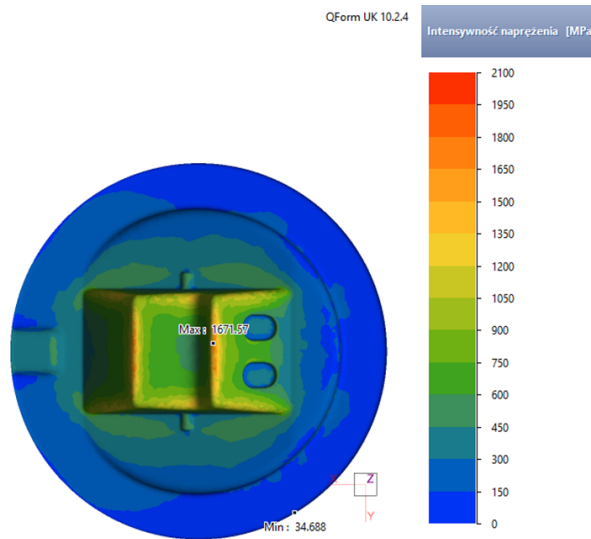


Figure 5: Effective stresses in the final die.

The results of effective stress exceeded the yield strength of the material. They occurred in the same locations as in the case of average stresses, and their magnitude could lead to the failure of the die.

Based on the obtained information, a different version of the preliminary die was designed. The radius of fillets were increased, which was believed to improve the flow kinematics of the material.

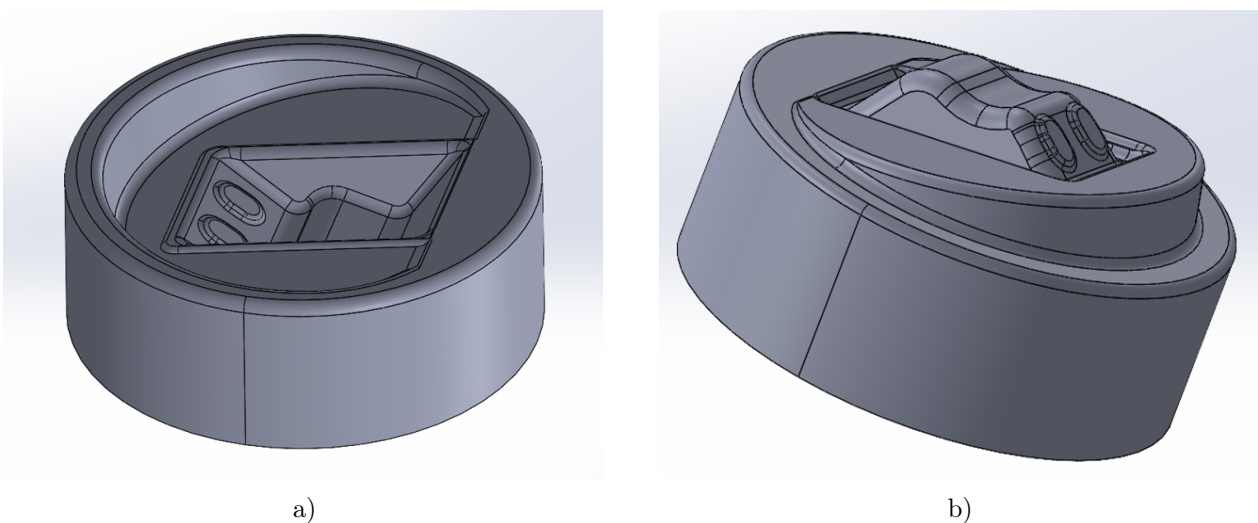


Figure 6: The preliminary die models created: a) bottom die, b) top die.

The geometry of the final die impression has not changed compared to the previous case, however, the shape of the input material has changed. The contour of the average stresses of the final die is shown in the drawing below. The maximum obtained values are below the limit value.

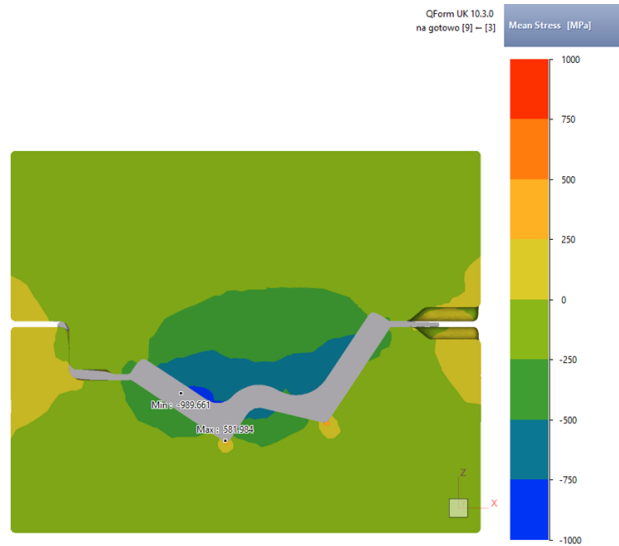


Figure 7: Mean stresses in the final die – after modification.

The modified geometry of the die impression reduced the values of stress intensity in the final die by 267 MPa, causing them to be below 1670 MPa.

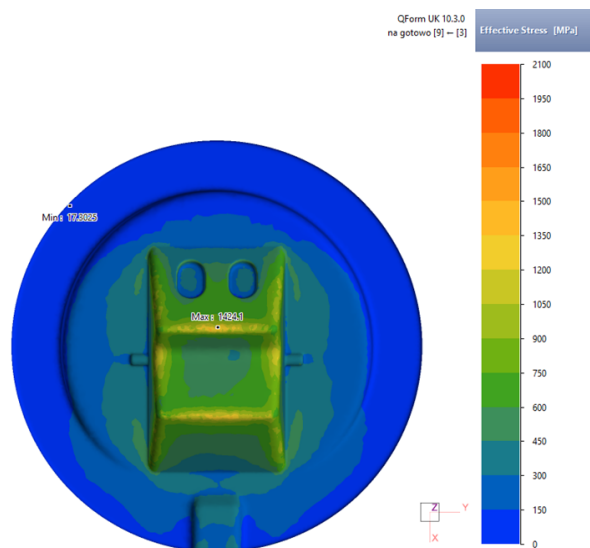


Figure 8: Effective stresses in the final die – after modification.

3. Summary

- The die impression which is fulfilling the project assumptions has been designed.
- Increasing the radius of fillets and inclining the of walls positively impacted the durability of the dies.
- Producing a preform with a shape more similar to the final product reduced stresses on the finishing die.

4. References

- [1] Sińczak J., Procesy Przeróbki Plastycznej, Wydawnictwo Naukowe AKAPIT, Kraków 2003, Praca zbiorowa pod redakcją Jana Sińczaka.
- [2] Wasiunyk P., Kucie matrycowe, Warszawa 1975.
- [3] M. Blicharski – Inżynieria materiałowa. Stal, WNT Warszawa 2010.
- [4] PN-EN ISO 4957:2004.

DAS HAT STEEL.
WEIL UNSERE LEIDENSCHAFT
MENSCHEN VERBINDET.

Lösungen für die grüne Zukunft der Stahlproduktion.



PRIMETALS
TECHNOLOGIES
**EIN ATTRAKTIVER
ARBEITGEBER**

Du suchst eine Herausforderung neben dem Studium und möchtest die erlernte Theorie in der Praxis anwenden? Dann bist Du bei uns genau richtig. Primetals Technologies bietet technologiebegeisterten Teamplayern viele Möglichkeiten: Spannende Aufgaben im internationalen Umfeld, gelebte Werte und Workshops zur Stärkung der Unternehmenskultur.

#pioneersforfuture



**Besuche uns
auf unserer
Karriereseite.**

meta.ls/ge-karriere

**Werde ein
Pioneer
at Heart.
Bewirb
dich jetzt!**

primetals.com

**MACHT
HEAVY METAL
DAS LEBEN LEICHTER?**

HIER PASSIERT'S!

Jetzt bewerben:
szag.com/karriere
#karrierevorwärts



SALZGITTERAG
Mensch, Stahl und Technologie

Single-point incremental forming of thin metallic sheets with the use of the robotic arm

Kosma Knap¹, Jan Źarski¹, Łukasz Lisiecki¹, Konrad Perzyński¹, Łukasz Madej¹

¹ Department of Applied Computer Science and Modeling, Faculty of Metals Engineering and Industrial Computer Science, AGH University of Krakow, Mickiewicza 30 av., 30-059 Krakow, Poland

The main objective of this work is to develop an automated robotic laboratory station for rapid prototyping and research on the development of forming technologies for low-batch production of sheet metal products. The research is based on the single-point incremental forming (SPIF) technology with the use of the Dobot M1 Pro robotic arm. The first part of this work presents the process of manufacturing the forming tools and adapting a robot tool holder to realize SPIF. Then, the development stages of algorithms to generate the toolpath and create a communication protocol between an implemented user-friendly software interface and the robotic arm are discussed. Finally, results from a series of operational tests on the developed stand, including forming different materials and shapes of final products, are shown and discussed. The work is summarized with the idea of transferring the created approach to an industrial robotic arm.

1. Introduction

With the rapid development of modern societies, the demand for non-standard metallic products is increasingly evident in various areas of everyday life. This is especially noticeable in the case of thin-walled products, often with very complex shapes, which are used in architecture, antique car industry, advertising industry, etc. Often, such products are unique or required in low batches. Thus, issues related to the economic aspects of manufacturing play a key role.

Standard sheet metal forming technologies, such as stamping, require the development of dedicated sets of two or more working tools (in the case of a standard stamping process - a bottom and a top die) with adequate durability [1]. The cost of these technologies is further raised by the mentioned very complex shape of the finished product to be obtained [2]. Those costs are justified for high-volume production, but for low-volume or unit production (e.g., components of individual medical prostheses), they are unacceptable. The solution for such low-volume production may be a single point incremental forming (SPIF) technology [3].

SPIF is a sheet metal forming technique that does not require any additional dies, as in the standard stamping. Instead, in the SPIF, a computer-controlled round-tipped tool incrementally deforms the sheet to create the final part shape. The SPIF technique is a cost-effective method dedicated to low-volume production and rapid prototyping. However, to make the process design stage even more time- and cost-effective, a scaled version of the SPIF was developed within the work based on the standard Dobot M1 Pro SCARA robot dedicated to lab applications. In this

case, the rotating mandrel installed on a robotic arm will plastically deform the material in a point-wise manner, forming it into any required shape.

The main aim of the work is to develop and implement algorithms for the proper control of a robot to run SPIF. The concept will be validated with a series of experiments conducted on thin 0.1 mm and 0.2 mm copper and brass sheet samples.

2. Design of SPIF robotic workstation

Dobot M1 Pro SCARA-type robot with 4 degrees of freedom was selected for the investigation (Figure 1). The robot's mobility is provided by four stepper motors J1-J4. The latter motor is responsible for the rotation of the forming stylus with defined velocity. The maximum operational extension of the arm is up to 400 mm, while the maximum load-carrying capacity is 1.5 kg. The exact range of motion of each motor and their maximum angular / linear velocities are shown in Table 1.

Table 1: Range of motion of each motor and their maximum angular / linear velocities.

Robotic arm	Range of motion	Maximum velocity
J1	$\pm 85^\circ$	$180^\circ/\text{s}$
J2	$\pm 135^\circ$	$180^\circ/\text{s}$
J3	5 mm – 245 mm	$1000 \text{ mm}/\text{s}$
J4	$\pm 360^\circ$	$1000^\circ/\text{s}$

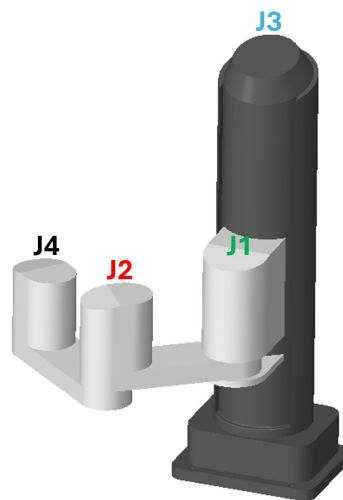


Figure 1: Coordinate system of the DOBOT SCARA M1 Pro.

The robotic system adaptation process to execute the SPIF process was composed of several steps. First, the dedicated forming tool holder often used in the CNC machines was acquired, as seen in Figure 2a, 2b. A brass forming tool (mandrel) was manufactured and placed in the

precision collet (Figure 2c). Precision collets make it possible to quickly change mandrels of different diameters, which is a practical solution for the process design stage.

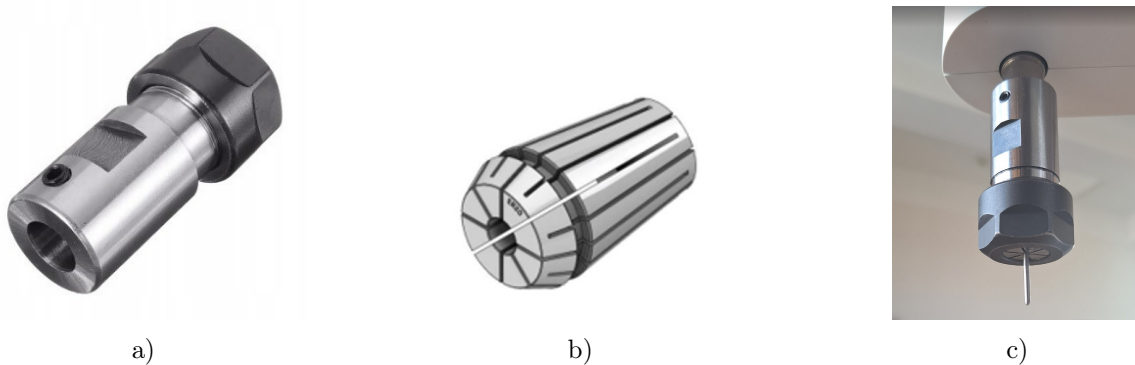


Figure 2: Forming tool holder compatible with robotic arm: a) robot-collet connection b) collet c) mandrel fixed in collet.

Then, in the second step, a sample fixture system was designed to allow stable clamping of the sheet during forming, as seen in Figure 3. The fixtures were manufactured with the use of 3D printing technology and PLA filament. A bottom part and a sheet holder were printed to allow a working area of 141 mm. The overall dimension of the fixture system is 197×197 mm.

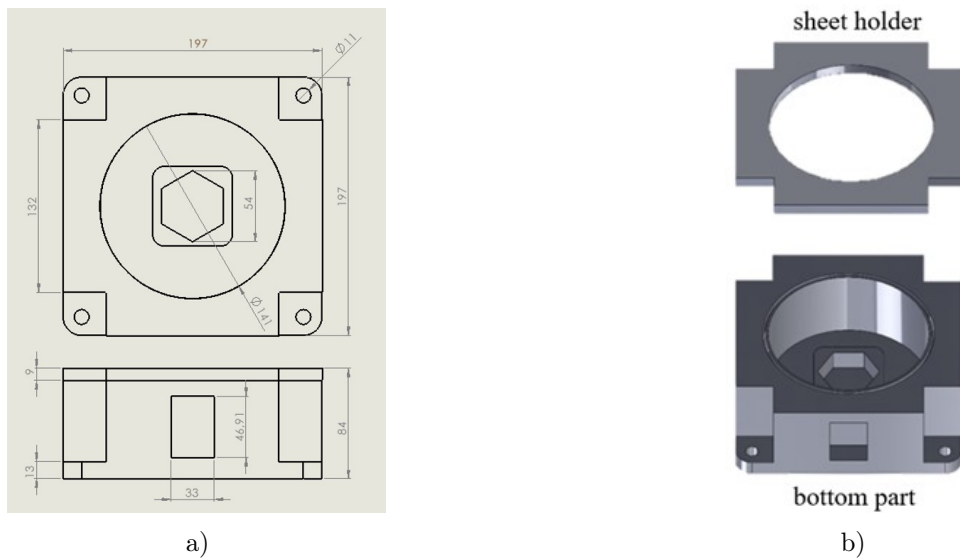


Figure 3: a) Dimensions of the fixture system and b) 3D views of the bottom part and sheet holder sections.

The sheet holder and bottom part of the fixture system are assembled using special clamps that apply load to the sheet sides during forming. Additionally, the bottom part features a notch that guides the sheet metal into a slit in the sheet holder resulting in stable sheet plate positioning.

Figure 4 shows the designed and assembled SPIF lab system. With such a setup, in the final step, the development and implementation of algorithms for the proper control of the SPIF system was realized.

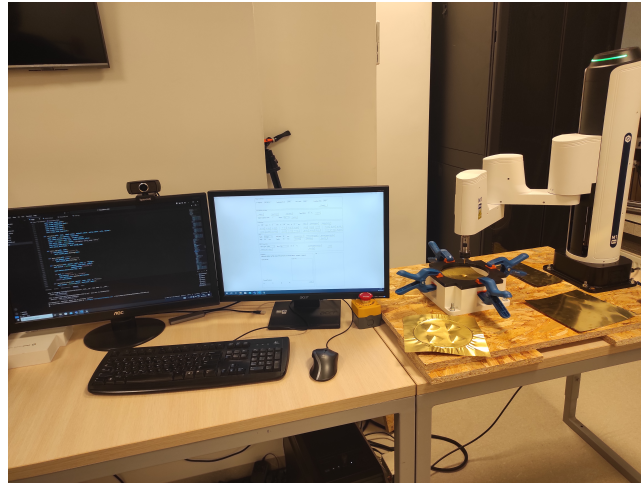
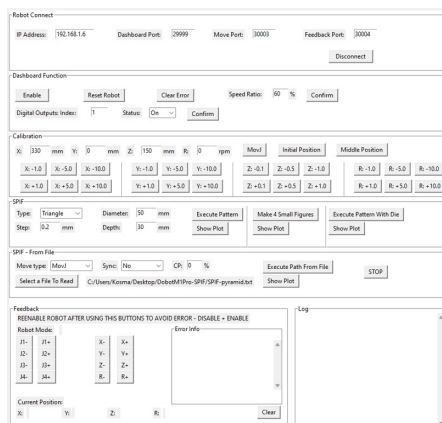


Figure 4: Developed lab system with a robotic arm with a holder, fixture system and the computer control unit.

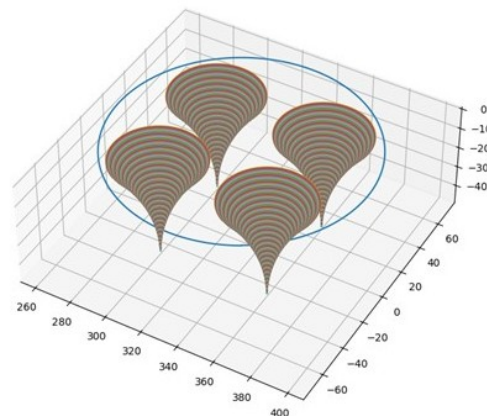
3. Software implementation

The developed software concept is based on two main parts: Back-end and front-end. In the front-end, the user defines process parameters, such as the robot arms' movement rate, the forming shape's diameter, and the forming depth, or selects the file with the predefined forming tool path. The back-end is responsible for all activities related to setting the robot's parameters, operating the robot, and displaying the current coordinates, error information, and event log. It also displays graphs representing tool movement paths.

The application was implemented using Python, a language that utilizes libraries provided by the Dobot company. The graphical user interface (GUI) was constructed with the TKinter library and is presented in Figure 5a. Figure 5b illustrates the forming tool paths designed directly in the GUI. The view of the tool path can be easily manipulated in 3D to check the exact path geometry.



a)



b)

Figure 5: a) Graphical user interface and b) visualization of the designed forming tool paths.

4. Establishing process limits

The developed SPIF lab system was tested with a series of forming operations. The 0.1 mm and 0.2 mm thickness copper and brass sheets were selected as case studies. An additional aim of the research was to determine the limiting forming parameters of the robotic arm. The following parameters were investigated: Type and thickness of the material, shape of the final component, diameter of the circle on which a shape is described, step size in the X, Y, and Z. The test setups and results of the conducted experiments are gathered in Table 2.

Table 2: Tests conducted using SPIF (H – hyperbolic cone, T – three side triangle pyramid, P – pyramid, 4T – four side triangle pyramid).

	Material type with thickness [mm]	Shape	Circle diameter [mm]	XY axis step [mm]	Planned forming depth [mm]	Z axis step [mm]	Reached forming depth [mm]
1	Copper 0.1	H	50	0.2	10	0.04	10
2	Copper 0.1	H	50	0.2	20	0.08	16.8
3	Copper 0.1	H	50	0.2	20	0.04	20
4	Copper 0.1	H	100	0.2	40	0.08	32
5	Brass 0.1	H	100	0.2	40	0.08	40
6	Copper 0.1	P	100	0.2	30	0.17	30
7	Brass 0.1	P	100	0.2	30	0.17	30
8	Copper 0.1	T	100	0.2	30	0.139	30
9	Copper 0.2	P	100	0.2	30	0.17	14.7
10	Copper 0.1	4T	50	0.2	10	0.09	10
11	Brass 0.1	4T	50	0.2	10	0.09	10

As presented in Table 2, most of the planned forming depth have been successfully achieved. However, some limitations of the developed system were identified:

- Test no. 2 failed to achieve the intended depth due to the clamping of the forming tool caused by improper sheet fixation in the holder.
- Test no. 4 result in sheet plate failure. The formability limit was reached for copper sheet with a thickness of 0.1 mm. Excessive thinning of the sheet walls led to material failure due to occurring stresses.
- Test no. 9 reached the formability limit of the Dobot M1 Pro robot. The process was stopped due to insufficient force to further deform the sheet.

Consequently, the SPIF process limit for the investigated robotic system was established. Examples of final SPIF-formed components are presented in the Figure 6.

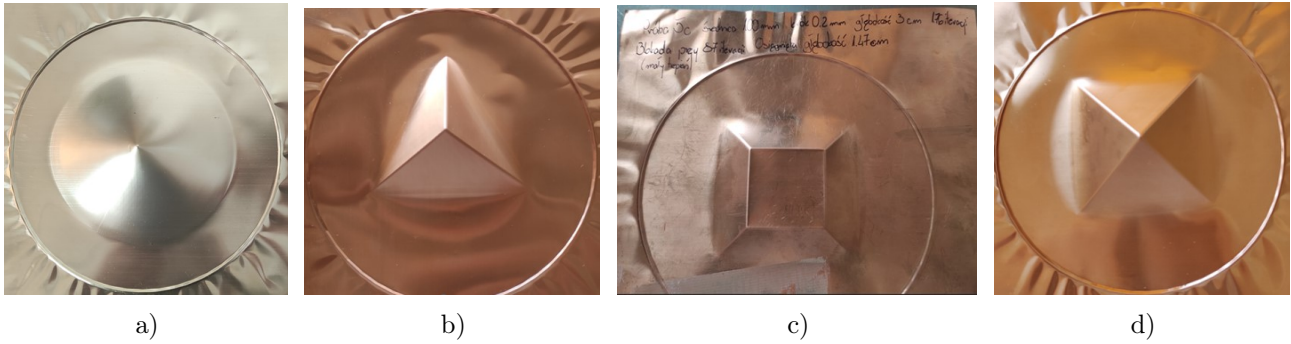


Figure 6: Examples of the effects of SPlF-formed components: a) hyperbolic cone, b) three side triangle pyramid, c) pyramid and d) four side triangle pyramid.

5. Summary and future research plan

The work presented an implementation of the robot control algorithms and the proper selection of the process parameters, which allow for the precise SPlF forming of thin copper and brass sheets. It was found that with an increase in the Z-axis step and an increase in the thickness of the sheet, formability decreases, which manifests in not reached planning forming depth and sheet failure. This phenomenon is particularly visible at larger thickness and Z-axis steps, confirming previous studies and literature [4, 5].

Future research will focus on adapting industrial robot to the incremental sheet forming process and expanding the range of investigated materials. The Kawasaki robotic arm (Figure 7a) available at the AGH University of Krakow will be adapted to enable forming using SPlF.

Figure 7b presents initial results of CAD assembly model of the proposed station for the robot that will be installed within its working area. The research will be conducted as part of the ROBOSPlF project funded under the AGH-IDUB activity.

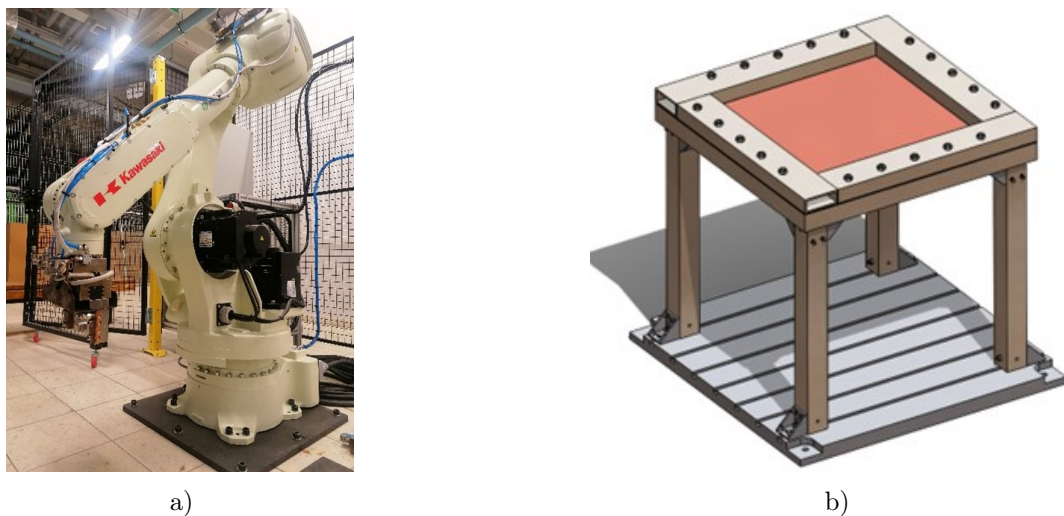


Figure 7: a) Kawasaki robotic arm located at the AGH University of Krakow b) CAD assembly model of SPlF station for robotic arm.

6. Acknowledgment

Research financed under the project 'ROBOSPIF project - single-point sheet metal forming using a robotic arm and 3D printing' (AGH-IDUB, activity: D12 - Integration of the educational process with scientific research, application no. 9027).

7. References

- [1] J. L. P. de Brito Câmara. Single Point Incremental Forming. Universidade Técnica de Lisboa, 2009.
- [2] T. Trzepieciński, B. Krasowski, A. Kubit, D. Wydrzyński. Possibilities of application of incremental sheet-forming technique in aircraft industry. Rzeszów: Oficyna Wydawnicza Politechniki Wrocławskiej, 2018, pp. 87-100.
- [3] A. Barsan, M. Crenganis, M. O. Popp, G.P. Rusu. Roboforming – investigations regarding forming forces in SPIF process. ACTA Universitatis Cibiniensis – Technical Series, 2020, 72.
- [4] M. Skjødt. Rapid prototyping by single point incremental forming of sheet metal. DTU Mechanical Engineering, 2008.
- [5] A. Barsan, S. G. Racz, R. Breaz. Incremental forming using KUKA KR210-2 industrial robot - research regarding design rules and process modeling. Lucian Blaga University of Sibiu, 2021.

Strain aging phenomena at mild steels produced by today's steel making technology

B. Kondas¹, V. Mertinger¹

¹ Institute of Physical Metallurgy Metalforming and Nanotechnology, University of Miskolc, H-3515 Miskolc, Hungary

The ageing of steel sheet grade DC01 from a European manufacturer was investigated by tensile testing of specimens taken in three directions. The mechanical material test was repeated after 3 days, 9 days, 2 weeks, 1 month and 6 weeks. No trend change indicative of ageing was detected after the determination of the standard metrics. On the basis of the literature data, it could be concluded that the steel does not show the ageing phenomenon. However, Erichsen cupping test and Nakajima test indicated a clear change in formability within the time interval studied. It is therefore concluded that the conventional mechanical tests are not sufficient to detect the ageing tendency of sheets made with modern steelmaking technology.

1. Introduction

Low carbon, unalloyed, cold-rolled, uncoated (LC) steel is the most widely used steel for cold forming in the manufacturing industry. This is commonly referred to in industry narrative as mild steel. The European standard grade for LC steels is the DC01 to 06 series. The basic grade DC01 is the grade where strain-aging occurs most rapidly, so its nature can also be most clearly observed in this grade. The strain-aging of steels has long been a well-known phenomenon and is, therefore, very well documented [1–4]. In this article, we will investigate the nature of strain-aging of DC01 sheets produced with current state-of-the-art technology and compare the results with those reported in the literature, and draw conclusions.

1.1. The causes and manifestations of strain-aging

Static strain-aging

Formational strain-aging is the result of a process of dislocation by movement and diffusion. During this process, the interstitial atoms (carbon and nitrogen) migrate to the end of the dislocation, where they cause less lattice strain. As time passes, the amounts of atoms reaching the dislocations increases, which makes the dislocations increasingly difficult to move. When the forming of sheets starts, the dislocations will come off from these atoms, which requires a higher stress value. Once the dislocations have left the atoms, even a small amount of stress is sufficient to move them further, reducing the measured force. This causes the appearance of the upper and lower yield strengths [5–7].

Dynamic strain-aging

The Portevin-Le Chatelier (PLC) effect (jerky flow) is caused by the dynamic interaction of moving dislocations and rapidly diffusing alloy atoms. In this case, the dislocation motion is not continuous but mostly intermittent. The process is characterized by the fluctuation of stress in the stress-strain curve [8, 9]. As a result of dynamic strain aging, the yield strength and tensile strength are increased, but the elongation is reduced and Lüders bands appear on the surface.

1.2. Developments in last decades in the production process of LC grades

The main factors influencing the aging of mild LC steels are their nitrogen content and dislocation density. The number of inclusions, the ferrite grain size and the second or third phase (cementite) in the microstructure can also have an indirect effect. Low nitrogen steel scrap and further input materials were successfully used to reduce the total nitrogen content in the melt. Due to ensure better formability and less aging tendency, the free nitrogen needs to be converted into the nitride. Aluminium cannot bind the total free nitrogen, so adding other nitride former elements like titanium, niobium or boron into the melt is necessary. The precise feeding is essential because the form and localization of the creating nitride determine the new grain size after annealing. Such measures are not fully enough to reduce the tendency of strain aging.

Further achievements were needed to improve the manufacturing technology as well. In the last decades, manufacturing technologies of LC steels have undergone significant development, resulting in an extraordinary improvement in the quality [10–12]. Since the 1950s, the most significant changes in the LC grade production have been as follows:

- Switch from Siemens-Martin to Linz Donawitz steel making technology
- General usage of 'full-killing' during steel production
- Optimization of batch dezoxidation (using Aluminium instead of Silicon)
- Improvement in the secondary metallurgy tools (desulphurization, argon stirring, vacuum treatment)
- Switch from block casting to continuous casting
- Optimization of slab reheating-, hot rolling- and coiling temperature during hot rolling
- Optimization of pass schedule at hot- and cold rolling
- Introduction and development of computer-supported speed control during hot-, cold and temper rolling
- Introduction and development of computer-supported temperature and time control during annealing

- Introduction of continuous annealing besides batch annealing
- General usage of temper rolling
- Continuous improvement in the product and process measurement methods and tools
- Development in the data collection and data evaluation in the steel production technologies [13–17]

1.3. Historical data from the technical literature regarding strain aging

The basic metallographic relationships of strain aging were established as early as in the 1930s and 1950s. Cold rolled sheet for deep drawing was a popular product of the post-World War II re-industrialization, so a great deal of scientific research on strain-aging was carried out in the 1960s and 1970s. The currently available literature predominantly concerns the results of products made with now obsolete technology. Many researchers have described findings as a result of their experiments. Remarkable are the results of Sylwestrowicz from the 50's, the US Steel experts from the 80's and Bhagat's research from 2008, who investigated materials what can be classified as DC01 grade today. Sylwestrowicz [18] defined a yield strength increase of about 70 MPa, US Steel experts measured 50 MPa increase in yield strength [19], while Bhagat [20] found a yield strength increase of about 18 MPa and a 0.6 % decrease in elongation in mild steel (Table 1) sheet after a fracture. All data were noted after a storage time of about 6 weeks at room temperature.

Table 1: Chemical composition of investigated sheets by Bhagat [20].

C %	Mn %	Si %	S %	Al %	N %
0.002	0.58	0.007	0.007	0.039	0.0015

2. Experimental

Based on the literature, it has been found that with strain-aging, the following changes in the properties of mild steels occur:

- Increasing yield strength and tensile strength
- Reduced elongation after fracture
- The upper and lower yield strength (static strain-aging) appears

Our research has, therefore, focused on identifying these four strain-aging effects.

2.1. Material

The effects of strain-aging were analyzed on standard cold rolled, annealed and temper-rolled samples of DC01 grade from an European manufacturer, using the results of tensile tests made 3 days, 9 days, 2 weeks, 1 month and 6 weeks after production. The production route and the chemical concentrations are shown in Figure 1 and Table 2, respectively.

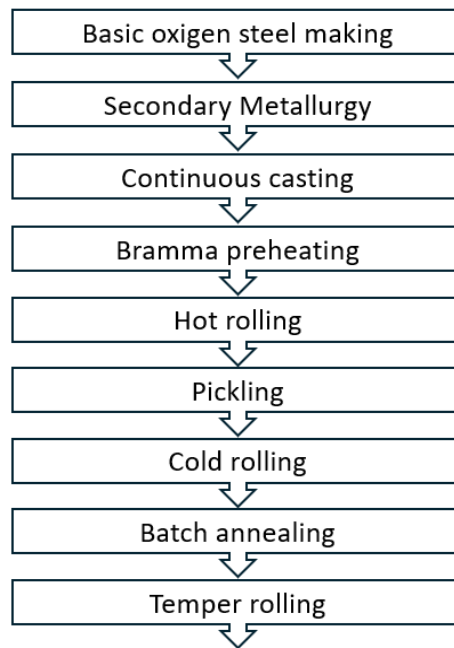


Figure 1: Production route of investigated steel sheets.

Table 2: Chemical composition of investigated sheets.

C %	Mn %	Si %	S %	Al %	N %
0.07	0.39	0.007	0.001	0.038	0.004

The time intervals of tests were determined according to the relevant product standards. The tensile test specimens were cut from $\frac{1}{4}$ of the width of the sheets from the third turn of the coil, closely spaced to each other, to keep the material's inhomogeneity as low as possible (Figure 2). Three specimens were tested per series (0, 45 and 90 degrees to the rolling direction). The tensile tests were performed on specimens of standard size (ISO 6892-1, Type B (20x80 mm)), prepared for testing by punching and grinding.

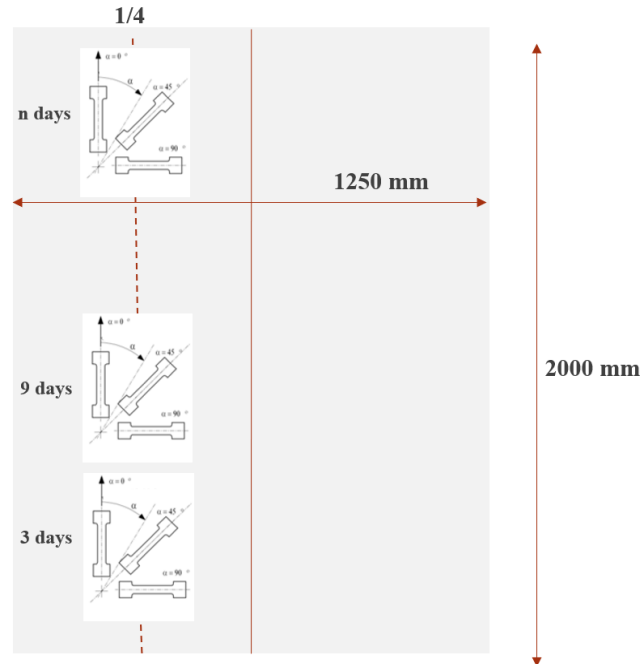


Figure 2: Sampling from the sheets.

2.2. Testing machine and method

The tensile tests were performed on a dual column floor model universal material tester type Instron 68FM-300. Measurement results were processed using the evaluation software type Bluehill 3. During the test, the elongation of the specimens was measured using an Aver Edge 32 video extensometer with a signal spacing of 80 mm longitudinally and 20 mm transversely. Additional parameters of the test; Load cell: 300 kN; Test temperature: room temperature (23 °C). The variation of the mechanical values ($R_{p0,2}$, R_{eH} , R_{eL} , R_m , A_{80}) was determined per series using the ISO 6892-1 Method B (stress rate control) on three test specimens per direction. The crosshead separation rate was uniformly 10 MPa/s up to the appearance of the yield point and 0.00671 s^{-1} after that. Additionally, static strain-aging was tested using the ISO 6892-1 Method A1 (strain-rate control) with a tension rate of 1-1 test per direction in three tests (0.002 s^{-1} ; 0.0002 s^{-1} ; 0.00002 s^{-1}). All main influencing factors were kept constant during the experiments. The bias of the measurement system was checked by testing certified standard specimens before each series of measurements.

3. Results and Discussion

The first tensile test was carried out on the 3rd day after production, where we confirmed the values on the manufacturer's test certificate of material supplied with the consignment. Figure 3, 4 and 5 show the variations in mechanical properties over time. The results show no clear trend

for yield strength, tensile strength or elongation after fracture over the tested interval could be detected. The changes were minor, corresponding to measurement uncertainty and material inhomogeneity. The most surprising result of the series of tests was that no lower or upper yield strengths could be determined for any of the 108 tests. Hence, no static strain-aging could be detected.

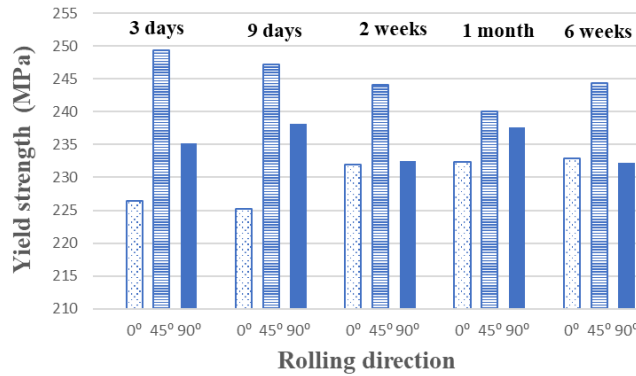


Figure 3: Variation of yield strength with time in different directions.

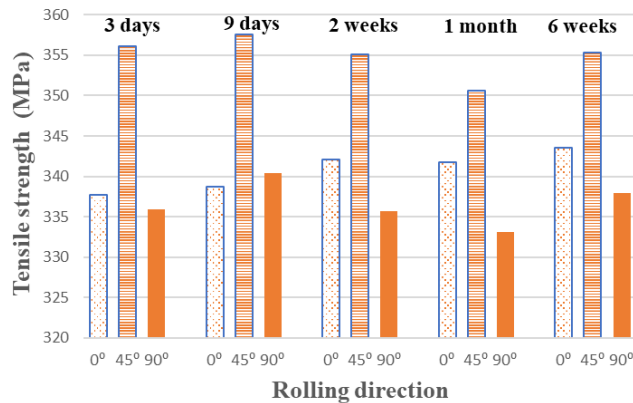


Figure 4: Tensile stress changes with time in different directions.

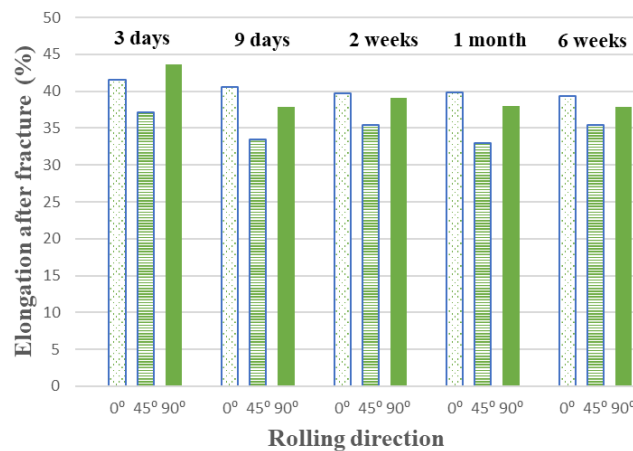


Figure 5: Change in elongation after fracture with time in different directions.

4. Conclusion

In this paper, the effects of strain-aging were tested as described in the literature on mild steel specimens produced with today's modern steelmaking technology. Based on the data of Sylwestrowicz, US Steel experts, and Bhagat, our research brings more moderate results. There has been a clear decreasing trend in history. In the 50's it was defined 70 MPa in the 80's; 50 MPa, in 2008 and 18 MPa increase in the yield strength due to the aging process, while, we cannot define any clear decreasing or increasing trend today. Based on the tensile tests of our experiments, we could not detect static strain-aging, i.e. the formation of upper and lower yield strengths, in the time interval investigated. Increases in yield strength and tensile strength values and decreases in elongation after fracture values were not observed in the tested specimens either. As it was seen, the degree of strain-aging described earlier in the literature is no longer present in mild steel products produced with today's technology.

It is worth analyzing the ageing phenomena because of the results of the technological tests. We performed the Erichsen cupping test and Nakajima test, which showed an evident degradation in the formability of tested sheets after a certain time. Developing a complex indicator(s) for determining strain-aging that can also be used conveniently by industry will be the next stage in our research.

5. References

- [1] S. Lou, D. O. Northwood 1993 Effect of Carbon and Nitrogen Content on Dynamic Strain Aging in Low Carbon Steels, *Canadian Metallurgical Quarterly* 33 243-249.
- [2] R. Rocha D. Alexandre C. Ximenes J. F. C. Lins 2020 The Effects of Manganese and Processing Technology on the Aging of Low Carbon Steels, *Journal of Materials Engineering and Performance*.
- [3] Sarkar B., Datta R., Chaudhuri S. K. 2009 Effect of Titan Nitrogen Ratio on Strain Aging and Plastic Anisotropy in Extra Deep Drawing Quality Steel, *Materials Science and Technology* 25 1408-1410.
- [4] De A. K., De Cooman B. C., Vandeputte S. 2001 Kinetics of Strain Aging in Bake Hardening Ultra Low Carbon Steel, *Journal of Materials Engineering and Performance* 10 567-575.
- [5] Cunningham S. 1999 Effect of substitutional elements on dynamic strain aging in steel, McGill University 101.
- [6] Cottrell A. H. and Bilby B. A. 1949 Dislocation Theory of Yielding and Strain Ageing of Iron, *Proceedings of the Physical Society Section A* 62 (1), 49–62.

- [7] Cottrell A. H. 1948 Report on the Strength of Solids, London Physical Society 30.
- [8] Penning P. 1972 Mathematics of the Portevin-Le Chatelier Effect, Acta Metallurgica, 20 1169–1175.
- [9] Campbell J. D. 1953 The Dynamic Yielding of Mild Steel, Acta Metallurgica 1.
- [10] K. Tsunoyama 1998 Metallurgy of Ultra Low C Interstitial Free Sheet Steel for Automotive Applications, phys.stat.sol. 167 427.
- [11] Gosh P., Ray R. K. 2017 Deep Drawable Steels Automotive Steels, Design, Metallurgy, Processing and Applications, 113-143.
- [12] S. Satoh 1985 A New Process for Manufacturing Deep Drawing Cold Rolled Steel Sheets from Extra Low Carbon Steels, Kawasaki Steel Technical Report. 12 36-44.
- [13] F. Oeters 1989 Metallurgie der Stahlherstellung, Verlag Stahleisen Düsseldorf.
- [14] G. Stolte 2007 Secondary Metallurgy, Verlag Stahleisen Düsseldorf.
- [15] M. Degner 2012 Moderne warmbandproduktion, Verlag Stahleisen Düsseldorf.
- [16] Jähniche at al. 1984 Werkstoffkunde Stahl Band 1, Verlag Stahleisen Düsseldorf.
- [17] Jähniche at al. 1985 Werkstoffkunde Stahl Band 2, Verlag Stahleisen Düsseldorf.
- [18] Sylwestrowicz W. and Hall E. O. 1951 The Deformation and Aging of Mild Steels, Proc. Phys. Soc. B 64 742.
- [19] William T. Lankford 1985 The Making, Shaping and Treating of Steel, Tenth Edition, Association of Iron and Steel Engineers, 1286-1287.
- [20] Bhagat A. N., Baek S. J. and Lee H. C. 2008 A Simple Method for Prediction of Shelf Life of Bake Hardening Steels, Material Science Engineerings 48 1781-1787.

Influencing parameters on reduction rate during hydrogen-based reduction of iron ore pellets

Oleksandr Kovtun^{1*}, Mykyta Levchenko¹, Christos G. Aneziris², Olena Volkova¹

¹ TU Bergakademie Freiberg, Institute of Iron and Steel Technology (IEST), Leipziger Strasse 34, 09599 Freiberg, Germany

² TU Bergakademie Freiberg, Institute of Ceramic, Glass and Construction Materials, Agricolastrasse 17, 09599 Freiberg, Germany

* Corresponding author: oleksandr.kovtun.iest@gmail.com

Hydrogen-based direct reduction process offers a promising avenue for significantly mitigating emissions. With the current focus on hydrogen reduction, it becomes imperative to some parameters such as temperature, chemical composition, and porosity. This study specifically investigates the influence of chemical composition and porosity at temperatures between 700 °C and 800 °C on the reduction of iron ore pellets using hydrogen. Porosity was evaluated using a mercury intrusion porosimeter, while the microstructure of the reduced pellets was analyzed via scanning electron microscopy. Remarkably, an increase in the temperatures resulted in increased pore size and overall porosity. Even lower gangue content may decrease the reduction rate. Investigating these characteristics can present their importance in reaching the optimal conditions of the direct reduction process and advancing technologies conducive to eco-friendly steel production.

Keywords: hydrogen; iron ore pellets; porosity; temperature; direct reduction.

Introduction

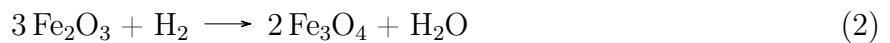
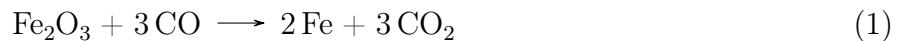
Conventional iron and steel production methods typically involve the use of a blast furnace (BF) in conjunction with a basic oxygen furnace (BOF). The operation of blast furnaces results in significant emissions of CO₂. Consequently, the total CO₂ emissions from steel manufacturing accounted for around 7–9 % of global anthropogenic CO₂ emissions in 2020 [1].

To mitigate CO₂ emissions, German steel producers as ArcelorMittal Europe, Thyssenkrupp Steel Europe, among others, are strategizing to manufacture ‘green steel’ using hydrogen [2–7]. Substituting hydrogen for coke as a reducing agent holds the potential to significantly diminish carbon dioxide levels. The direct reduced iron (DRI) process involves the primary conversion to metallic iron in the solid state without reaching the melting point. Existing steelmaking practices already incorporate direct reduction processes for iron ore pellets using natural gas or an H₂ / CO mixture, such as Midrex technology [8, 9], HyL / Energiron [10], Circored [11], and others [12–15].

Due to the slow reaction rate, natural gas is not used directly and the decomposition of natural gas occurs at high temperature with formation carbon and hydrogen. Hence, it has to be reformed into CO and H₂ and this mixture can be used directly for reduction process. However,

the CO₂ emissions are also produced. Their amount is lower compared with primary reaction of ironmaking using BF process [16, 17].

Thus, the primary reaction of ironmaking using reducing agent CO (reaction 1) can be replaced with pure H₂ for the achievement of CO₂-zero emissions using DRI technology. Additionally, the reduction of hematite does not immediately occur to metallic iron but is reduced stepwise to a lower iron oxide depending on a temperature as hematite → magnetite → wüstite → metallic iron (reactions 2–4) [16, 18–20]:



Concerning the kinetics of hydrogen reduction, the first two reactions (reaction 2 and 3) proceed at a quicker rate compared to the third (reaction 4). Consequently, the kinetics are primarily governed by the FeO-Fe reaction. Alongside kinetics, the reduction rate of iron ore pellets can be controlled by temperature, composition of the reducing gas, material porosity, grain size of iron oxide, form material (pellets, briquettes, etc.) and gangue content. These factors can affect the pellet reduction rate and have been studied by numerous researchers. El-Geassy et al. [21] studied the influence of porosity and grain size variations in hematite compacts at varying temperatures on the hydrogen reduction rate. Their findings suggested that as porosity increased or grain size decreased, and with higher temperatures, the reduction rate intensified. Similarly, Bahgat and Khedr [22] observed an escalation in the reduction rate when the reaction temperature was raised from 900 °C to 1100 °C.

Recent studies have delved into examining the gas composition's impact on the reduction of iron ore pellets, focusing on the reducing agents like carbon monoxide, hydrogen, or their mixtures. In 2005, Bonalde et al. [23] illustrated the reduction rate of hematite at 850 °C using hydrogen-carbon monoxide blends, revealing a significantly higher reduction rate with hydrogen alone. Specifically, the reduction rate under a hydrogen atmosphere reached 100 %, while it was only 50 % in a CO atmosphere.

Additionally, Turkdogan and Vinters [24] investigated the reducibility of iron ore pellets and the effects of lime and silica additions. They noted that reduction in a hydrogen atmosphere resulted in shorter reduction times compared to a carbon monoxide atmosphere, consequently leading to a higher reduction rate in the hydrogen environment. Investigations by Wang and Sohn [25],

revealed that a low SiO_2 content coupled with a high CaO content in the iron oxide compact resulted in an enhanced reduction rate. Another study [26] demonstrated an enhancement in reducibility with the addition of CaCO_3 to hematite iron ore briquettes. However, at elevated reduction temperatures, the reducibility decreased with increasing lime content compared to the original briquettes containing 1 % CaCO_3 . The influence of calcium oxide on reducibility was further expounded by its interaction with temperature, porosity, and the formation of compounds with other elements present in iron ore pellets or briquettes [24, 26–29]. Substituting CaO with MgO in dolomite form resulted in a marginal reduction in reducibility. When MgO was introduced to the iron ore concentrate, it stabilized magnetite, decreasing the Fe_2O_3 content and, consequently, the reduction index [30, 31]. The study by Kapelyushin et al. [32, 33] demonstrated Al_2O_3 diffusion from FeO into the hercynite-rich Fe_3O_4 - FeAl_2O_4 solution during the reduction process, negatively impacted the reduction rate and thereby reduced the reducibility of Fe_3O_4 to FeO . Zeng et al. [34] similarly observed the adverse influence of Al_2O_3 on iron ore reduction.

The motivation for this study lies in investigating the parameters influencing on the H_2 -based reduction of iron ore pellets used in blast furnaces. Specifically, the influence of temperature, gangue content and porosity on the direct reduction degree of blast furnace pellets, and also scrutinize the microstructural changes are considered. Therefore, the findings of this investigation contribute to the existing knowledge regarding the parameters controlling direct reduction in a hydrogen atmosphere, potentially influencing the economic viability of the process.

Experimental procedures

Materials

Two types of fired industrial hematite pellets intended for ironmaking production due to blast furnaces were used for the experimental part of this research. The chemical composition is presented in Table 1 [35]. The pellet size was approx. 12–16 mm in diameter.

Table 1: The chemical composition of fired iron ore pellets (wt. %) [35].

	Fe_{met}	FeO	CaO	SiO_2	MgO	Al_2O_3	MnO	Na_2O	P_2O_5	Porosity, %
P1	65.0	0.5	1.3	3.6	0.6	0.5	0.06	0.04	0.04	22.15
P2	66.6	0.1	0.8	2.1	0.4	0.4	0.32	0.02	0.03	27.19

P2 had a higher iron oxide content and lower gangue content than those of P1. Additionally, the porosity for P2 was higher by approximately 5 % compared to P1. The different results of the reduction rate were expected according to Table 1.

Experimental equipment

Experiments on the reduction of pellets by hydrogen were carried out in a heat-resistant steel retort using a resistance furnace for heating. The retort is shown schematically in Figure 1. The experimental conditions and methodology were the same as in the recent study of results of hydrogen reduction of iron ore pellets at different temperatures by Kovtun et al. [36].

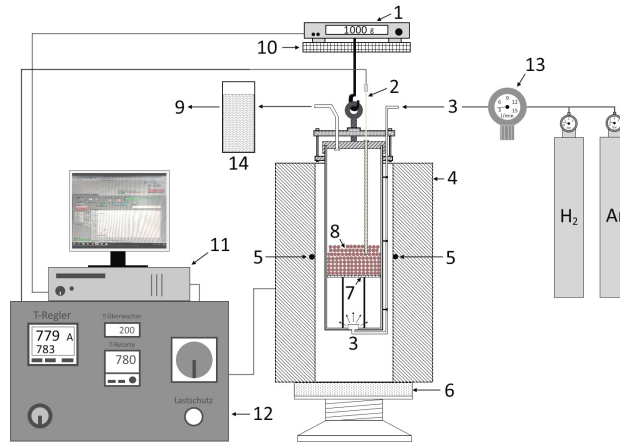


Figure 1: The scheme of the retort: 1 – weight measuring system; 2 – B-type thermocouple for sample temperature; 3 – gas inlet (Ar, H₂); 4 – resistance furnace; 5 – N-type thermocouple for resistance furnace; 6 – closed bottom cover; 7 – base with holes on stand; 8 – pellets; 9 – gas outlet (Ar, H₂O); 10 – water-cooled copper stand; 11 – personal computer; 12 – generator with the temperature controller; 13 – gas flow rate meter; 14 – container with water

Considering the mass change during the experiment, the reduction degree (RD), was calculated according to the standard of ISO 4695:2015(E) using the following equation:

$$RD = \frac{0.111 * w_1}{0.430 * w_2} + \frac{\Delta m_t}{m_0 * 0.430 * w_2} * 100 \quad (5)$$

where m_0 is the mass of test portion, in grams [g]; Δm_t is the mass loss of test portion after reduction time t , in grams [g]; w_1 is the iron(II) oxide content of the test sample prior to the test, in percentage by mass [wt. %]; w_2 is the total iron content (Fe_{met}) of the test portion to the test, percentage by mass [wt. %].

The cooled reduced pellets underwent embedding in epoxy, subsequent drying, halving, polishing, and subsequent analysis utilizing a Scanning Electron Microscope (SEM) Ultra55. This instrument was outfitted with Energy-Dispersive X-ray Spectroscopy (EDX), Wavelength-Dispersive X-ray Spectroscopy (WDX), Electron Backscatter Diffraction (EBSD), and Scanning Transmission Electron Microscopy (STEM) (Zeiss NTS GmbH).

The distribution of pore sizes was assessed employing mercury intrusion porosimetry with an AutoPore V 9600 porosimeter and the MicroActive software (Micromeritics®). This involved incrementally increasing the applied pressure from 0.0007 to 420.5802 MPa. At a contact angle of 140°, the diameters of pore openings, through which mercury penetrated, varied from approximately 290 μm to 3.5 nm.

Results and discussion

Effect of temperature on reduction degree during H₂ reduction

The completion of the reduction of the iron ore pellets is indicated by the plateau, while the degree of reduction should be maximum. The time to reach the plateau was different at 700 °C and 800 °C. The results of the reduction degree with time as a function of temperature during the reduction process are shown in Figure 2.

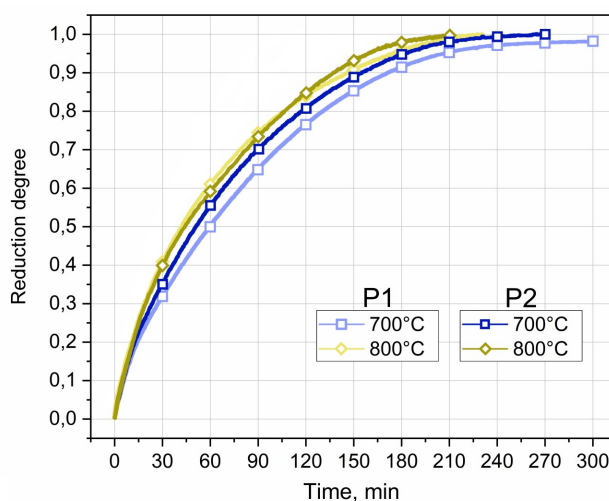


Figure 2: The effect of different temperatures on reduction degree for P1 and P2

As seen from Figure 2, the reduction rate increased with increasing temperature. Additionally, P2 reached the plateau more rapidly than P1. Thus, the reduction process at 700 °C was completed in 300 and 270 minutes for P1 and P2, respectively. P1 reached the plateau in approximately 230 min of reduction at 800 °C, since P2 in 210 min. A significant effect of temperature on the reduction rate in the H₂ atmosphere was also reported by many researchers [16, 18–21, 36–38].

Porosimeter results

In Figure 3, the size distribution of open pores has changed during hydrogen reduction at different temperatures is presented compared with the porosity of the initial P1 and P2.

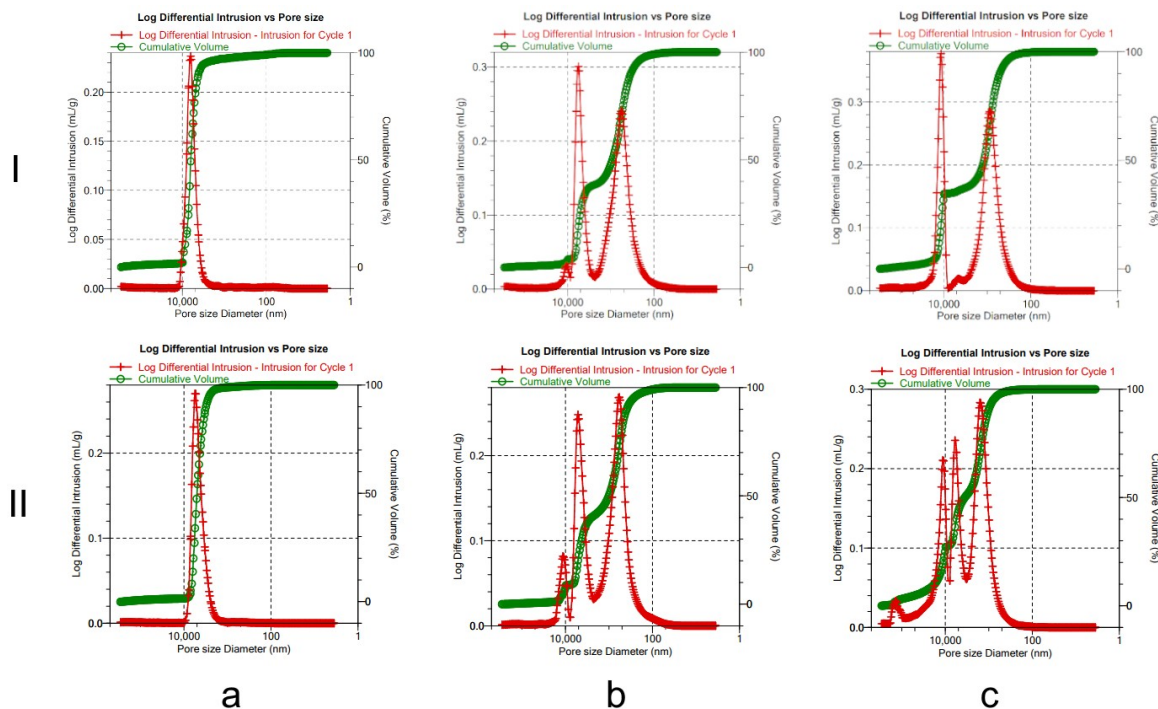


Figure 3: Pore size distribution of initial P1 (I,a) and P2 (II,a) and reduced at 700 °C (b) and 800 °C (c)

The result of mercury intrusion porosimetry of the initial pellets indicated the presence of a porous structure. The apparent porosity was 22.15 % for P1 and 27.2% for P2, respectively. The mercury intrusion porosimetry results of reduced pellets at different temperatures indicated the progress of porosity by increasing reduction temperatures. The cumulative curve (as shown in green in Figure 3) at 700 °C and 800 °C showed the development of three distinct pore-size populations. A large population was in small and medium-sized pores and a smaller population in pores larger than 10 μm at 700 °C. A shift in the cumulative volume curve towards the formation of large pores was detected at 800 °C.

Thus, the cumulative volume of pores larger than 10 μm increased. The apparent porosity of reduced P1 at 700 °C and 800 °C was 48.13 % and 51.45 %, and it was 50.19 % and 55.43 % for P2, respectively. Moreover, the tendency of open pore formation during the reduction process of P1 at 700 °C was identical to P2. However, an increase in temperature led to a shift in the formation of pores of more than 10 μm in samples P2 compared with P1. These results are in accordance with the reduction degree results and with apparent porosity.

Recent studies also showed that porosity increased with temperature increasing [39–41]. This can be attributed to the faster reduction process with increasing the temperature. The formation

of small and medium-sized pores is in accordance with the results of El-Geassy and Nasr [21]. Based on a study [35], the pore formation behavior can also be characterized by the so-called reduction swelling index (RSI), which represents the volumetric expansion of the pellet during the reduction time and has a critical value when it is more than 20 %.

Effect of gangue on reduction degree during H₂ reduction

The temperature exerted an influence on the reduction degree and rate. The reduction degree in 120 minutes was 0.77 at 700 °C and 0.84 at 800 °C for P1. The RD for P2 was 0.79 at 700 °C and 0.85 at 800 °C. Despite the temperature effect, gangue can influence the RD [27, 29, 42, 43]. The effect of gangue on the RD in this work was also observed in P1. Thus, the values of RD during reduction time were different, but this difference was insignificant (Figure 2). However, gangue contenting in P1 and P2 was also insignificantly different (Table 1).

The cross-sections for P1 and P2 at different temperatures were investigated due to SEM / EDX analysis to detect the gangue effect. The results are presented in Figure 4.

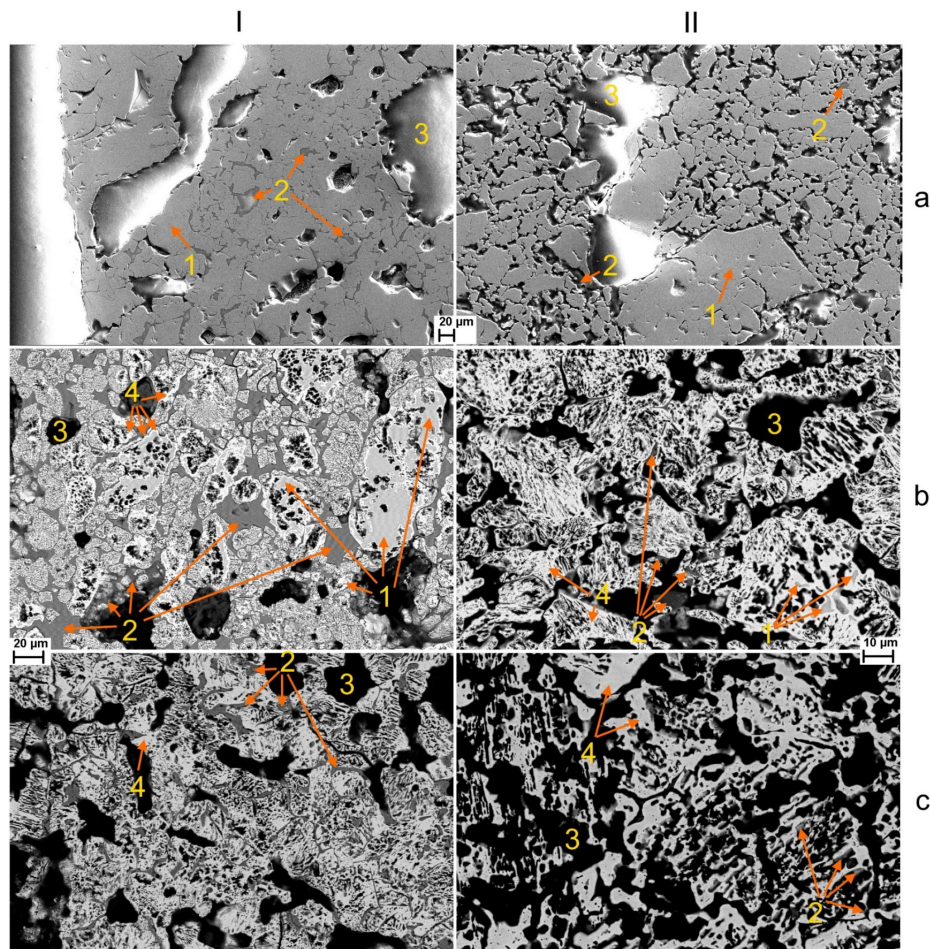


Figure 4: SEM / EDX analysis of initial P1 (I,a) and P2 (II,a) and reduced at 700 °C (b) and 800 °C (c), where 1 – iron oxide, 2 – gangue, 3 – pores and 4 – metallic iron

The results obtained from SEM /EDX fully confirmed the previous findings in the present study. Thus, despite the complete reduction occurring at 700 °C, iron oxide was observed in the reduced pellets. Specifically, pellets P1 exhibited a significantly higher amount of unreduced iron compared to P2. Iron oxide particles began to be reduced at the edges, while the center remained completely unreduced. It was not observed at 800 °C. Furthermore, the visible porosity observed in the SEM results correlated with the porosity measurements obtained from the porosimeter; notably, samples P2 exhibited higher porosity in both the initial and reduced states compared to P1. This underscores the significant influence of gangue content, as the voids were predominantly concentrated at the edges of the iron oxide and in the open pores places, hindering or slowing down the reduction process. Additionally, the gangue prevented the occurrence of pore formation and swelling. These results are consistent with those obtained from the porosimeter. The gangue is primarily expressed in CaO and SiO₂, as comparable in Table 1.

Conclusion

The reduction of two types of iron ore pellets was analyzed through experiments on retort at temperatures of 700 °C and 800 °C in the H₂ atmosphere. The following conclusion can be drawn:

- Increasing the temperature from 700 °C to 800 °C resulted in a faster reduction rate and higher reduction degree. Additionally, unreduced iron oxide was observed at 700 °C.
- The reduced samples exhibited an apparent porosity measured by mercury intrusion porosimetry ranging from approximately 48 % to 55 %. This increase was approximately 2.3 times for P1 and 2 times for P2 compared with an initial porosity.
- Gangue content affects both the reduction rate, initial porosity and pore formations. Despite the higher ratio of increased porosity between reduced sample P1 compared to the initial (2.3 times) and reduced sample P2 compared to the initial (2 times), the reduction rate is lower by the reduction of sample P1. So, gangue influences the initial porosity, which further impacts the reducibility.
- The effect of gangue and porosity at higher temperatures can be and has to be investigated in detail by further additional studies.

Acknowledgement

The authors are thankful to the Free State of Saxony for the financial support through the Saxony State Scholarship.

Declaration of Competing Interest

The authors declare that they have no known competing financial interests or personal relationships that could have influenced the work reported in this study.

Funding sources

This research did not receive any specific grants from funding agencies in the public, commercial, or not-for-profit sectors.

References

- [1] Climate change policy paper. WorldsteelOrg n.d. <https://worldsteel.org/publications/policy-papers/climate-change-policy-paper/> (accessed February 23, 2024).
- [2] ArcelorMittal plans major investment in German sites, to accelerate CO₂ emissions reduction strategy and leverage the hydrogen grid | ArcelorMittal 2021. <https://corporate.arcelormittal.com/media/news-articles/arcelormittal-plans-major-investment-in-german-sites-to-accelerate-co2-emissions-reduction-strategy-and-leverage-the-hydrogen-grid/> (accessed February 23, 2024).
- [3] ArcelorMittal Europe to produce ‘green steel’ starting in 2020 | ArcelorMittal 2020. <https://corporate.arcelormittal.com/media/news-articles/arcelormittal-europe-to-produce-green-steel-starting-in-2020/> (accessed February 23, 2024).
- [4] Weltpremiere in Duisburg: NRW-Wirtschaftsminister Pinkwart startet bei thyssenkrupp Versuchsreihe zum erstmaligen Einsatz von Wasserstoff im Hochofen. thyssenkrupp n.d. <https://www.thyssenkrupp-steel.com/de/newsroom/pressemitteilungen/weltpremiere-in-duisburg.html> (accessed February 23, 2024).
- [5] SIP-Technologie (Sequence Impulse Process) n.d. <https://www.primetals.com/de/landing-pages/weniger-betriebskosten-im-hochofen> (accessed February 23, 2024).
- [6] SALCOS. SALCOS® n.d. <https://salcos.salzgitter-ag.com/de/index.html> (accessed February 23, 2024).

- [7] GrInHy2.0. SALCOS® n.d. <https://salcos.salzgitter-ag.com/de/grinhy-20.html> (accessed February 23, 2024).
- [8] Atsushi M, Uemura H, Sakaguchi T. MIDREX processes. *Kobelco Technol Rev* 2010;29.
- [9] Sarkar S, Bhattacharya R, Roy GG, Sen PK. Modeling MIDREX Based Process Configurations for Energy and Emission Analysis. *Steel Research Int* 2018;89:1700248. <https://doi.org/10.1002/srin.201700248>.
- [10] Zugliano A, Primavera A, Pignattone D, Martinis A. Online modelling of energiron direct reduction shaft furnaces. *IFAC Proceedings Volumes* 2013;46:346–51.
- [11] Nuber D, Eichberger H, Rollinger B. Circored fine ore direct reduction. *Stahl Eisen* 2006;126.
- [12] Burke PD, Gul S. HIs melt—the alternative ironmaking technology. *Proceedings of International Conference on Smelting Reduction for Ironmaking*, Jouhari, AK, Galgali, RK, Misra, VN, Eds, 2002, p. 61–71.
- [13] Hillisch W, Zirngast J. Status of Finmet plant operation at BHP DRI, Australia. *Steel Times International* 2001;25:20.
- [14] Meijer K, Guenther C, Dry RJ. HIsarna pilot plant project. *Proc. 1st Int. Conf. on Energy Efficiency and CO2 Reduction in the Steel Industry*, 2011.
- [15] Schenk JL. Recent status of fluidized bed technologies for producing iron input materials for steelmaking. *Particuology* 2011;9:14–23.
- [16] Dutta SK, Sah R. Direct reduced iron: Production. *Encyclopedia of Iron, Steel, and Their Alloys* 2016:1082–108.
- [17] Monazam ER, Breault RW, Siriwardane R, Richards G, Carpenter S. Kinetics of the reduction of hematite (Fe_2O_3) by methane (CH_4) during chemical looping combustion: A global mechanism. *Chemical Engineering Journal* 2013;232:478–87. <https://doi.org/10.1016/j.cej.2013.07.091>.
- [18] Patisson F, Mirgaux O. Hydrogen ironmaking: How it works. *Metals* 2020;10:922.
- [19] Spreitzer D, Schenk J. Reduction of Iron Oxides with Hydrogen—A Review. *Steel Research Int* 2019;90:1900108. <https://doi.org/10.1002/srin.201900108>.
- [20] Battle T, Srivastava U, Kopfle J, Hunter R, McClelland J. The direct reduction of iron. *Treatise on process metallurgy*, Elsevier; 2014, p. 89–176.
- [21] El-Geassy AA, Nasr MI. Influence of the original structure on the kinetics of hydrogen reduction of hematite compacts. *Transactions of the Iron and Steel Institute of Japan* 1988;28:650–8.

- [22] Bahgat M, Khedr MH. Reduction kinetics, magnetic behavior and morphological changes during reduction of magnetite single crystal. *Materials Science and Engineering: B* 2007;138:251–8.
- [23] Bonalde A, Henriquez A, Manrique M. Kinetic analysis of the iron oxide reduction using hydrogen-carbon monoxide mixtures as reducing agent. *ISIJ International* 2005;45:1255–60.
- [24] Turkdogan ET, Vinters JV. Reducibility of iron ore pellets and effect of additions. *Canadian Metallurgical Quarterly* 1973;12:9–21. <https://doi.org/10.1179/cmq.1973.12.1.9>.
- [25] Wang HT, Sohn HY. Effect of CaO and SiO₂ on swelling and iron whisker formation during reduction of iron oxide compact. *Ironmaking & Steelmaking* 2011;38:447–52. <https://doi.org/10.1179/1743281211Y.0000000022>.
- [26] Strangway PK, Ross HU. The Effect of Calcium Carbonate on the Reducibility of Iron-Oxide Agglomerates. *Canadian Metallurgical Quarterly* 1965;4:97–111. <https://doi.org/10.1179/cmq.1965.4.1.97>.
- [27] Kim W-H, Lee Y-S, Suh I-K, Min D-J. Influence of CaO and SiO₂ on the reducibility of wüstite using H₂ and CO gas. *ISIJ International* 2012;52:1463–71.
- [28] Seth BBL, Ross HU. The Effect of Lime on The Reducibility of Iron-Oxide Agglomerates. *Canadian Metallurgical Quarterly* 1963;2:15–30. <https://doi.org/10.1179/cmq.1963.2.1.15>.
- [29] Basumallick A. Influence of CaO and Na₂CO₃ as additive on the reduction of hematite-lignite mixed pellets. *ISIJ International* 1995;35:1050–3.
- [30] Panigrahy SC, Rigaud MAJ, Dilewijns J. The effect of dolomite addition on the properties of sinters produced from a high aluminous iron ore. *Steel Research* 1985;56:35–41. <https://doi.org/10.1002/srin.198500593>.
- [31] Cores A, Babich A, Muñiz M, Ferreira S, Mochon J. The influence of different iron ores mixtures composition on the quality of sinter. *ISIJ International* 2010;50:1089–98.
- [32] Kapelyushin Y, Xing X, Zhang J, Jeong S, Sasaki Y, Ostrovski O. Effect of Alumina on the Gaseous Reduction of Magnetite in CO/CO₂ Gas Mixtures. *Metall Mater Trans B* 2015;46:1175–85. <https://doi.org/10.1007/s11663-015-0316-z>.
- [33] Kapelyushin Y, Sasaki Y, Zhang J, Jeong S, Ostrovski O. Formation of a Network Structure in the Gaseous Reduction of Magnetite Doped with Alumina. *Metall Mater Trans B* 2017;48:889–99. <https://doi.org/10.1007/s11663-016-0897-1>.
- [34] Zeng R, Li W, Wang N, Fu G, Chu M, Zhu M. Effect of Al₂O₃ on the gas-based direct reduction behavior of Hongge vanadium titanomagnetite pellet under simulated shaft furnace atmosphere. *Powder Technology* 2020;376:342–50.

- [35] Kovtun O, Levchenko M, Oldinski E, Gräbner M, Volkova O. Swelling Behavior of Iron Ore Pellets during Reduction in H₂ and N₂ /H₂ Atmospheres at Different Temperatures. *Steel Research Int* 2023;94:2300140. <https://doi.org/10.1002/srin.202300140>.
- [36] Kovtun O, Levchenko M, Ilatovskaia MO, Aneziris CG, Volkova O. Results of Hydrogen Reduction of Iron Ore Pellets at Different Temperatures. *Steel Research Int* 2024:2300707. <https://doi.org/10.1002/srin.202300707>.
- [37] Wagner D, Devisme O, Patisson F, Ablitzer D. *A Laboratory Study of the Reduction of Iron Oxides by Hydrogen* 2008.
- [38] Korobeinikov Y, Meshram A, Harris C, Kovtun O, Govro J, O'Malley RJ, et al. Reduction of Iron-Ore Pellets Using Different Gas Mixtures and Temperatures. *Steel Research Int* 2023;94:2300066. <https://doi.org/10.1002/srin.202300066>.
- [39] Turkdogan ET, Vinters JV. Gaseous reduction of iron oxides: Part III. Reduction-oxidation of porous and dense iron oxides and iron. *Metall Trans* 1972;3:1561–74. <https://doi.org/10.1007/BF02643047>.
- [40] Turkdogan ET, Olsson RG, Vinters JV. Gaseous reduction of iron oxides: Part II. Pore characteristics of iron reduced from hematite in hydrogen. *Metall Trans* 1971;2:3189–96. <https://doi.org/10.1007/BF02814971>.
- [41] Scharm C, Küster F, Laabs M, Huang Q, Volkova O, Reinmöller M, et al. Direct reduction of iron ore pellets by H₂ and CO: In-situ investigation of the structural transformation and reduction progression caused by atmosphere and temperature. *Minerals Engineering* 2022;180:107459.
- [42] Sharma T, Gupta RC, Prakash B. Effect of gangue content on the swelling behaviour of iron ore pellets. *Minerals Engineering* 1990;3:509–16.
- [43] El-Geassy AA, Nasr MI, Hessien MM. Effect of reducing gas on the volume change during reduction of iron oxide compacts. *ISIJ International* 1996;36:640–9.

#nextgenerationsteel

Der perfekte Werkstoff für deine Karriere: unser Stahl.

Wir, das sind rund 26.000 Mitarbeitende an 19 Produktionsstandorten, sind als Deutschlands größter Stahlhersteller nicht nur Ausgangspunkt vieler industrieller Wertschöpfungsketten und Innovationen, sondern auch Wegbereiter der grünen Transformation. Mit unserem Premiumstahl als Basiswerkstoff für die Energie- & Mobilitätswende und vieler weiterer Branchen, gestalten wir aktiv den Wandel in eine nachhaltige Zukunft. Die Leidenschaft und Kompetenz unseres Stahlteams sind dabei unsere besondere Stärke und das Herzstück unsers Unternehmens. Ja – Stahlexperten sind wir schon seit über 200 Jahren. Und wir gehen mit der Zeit und sind wandlungsfähig. Gestalte mit uns den technologischen Wendepunkt hin zur klimaneutralen Stahlproduktion.



engineering.tomorrow.together.



thyssenkrupp

Mechanical properties of steel reinforcing bars

Zoltán Endre Magyari¹

¹ University of Miskolc, Faculty of Material Engineering

The objective of the project was to enhance the mechanical properties of steel reinforcing bars, commonly known as rebars. The main focus among the mechanical properties was on the $A_5\%$ elongation at fracture. The $A_5\%$ stands for the percent elongation for proportional samples with length L_0 equal to five times the diameter. The reason for this project was to make it suitable for higher grades of steel. For this purpose, data was collected, the chemical composition of the billets, the various temperatures, and the cooling parameters, a.k.a. the rolling properties, and lastly, the mechanical properties of the samples taken. Three samples were taken from each batch. Among these samples, microscopic examination was implemented. There were multiple changes during the monitored time frame, in the smelting phase, and in the rolling phase as well, with the intention of achieving this goal. Along with the implementation of each change, trial productions were concluded before the finalization of the changes. I compiled the collected data into various sheets, and analyzed them using academic knowledge, and hands-on experience to find correlations between the rolling properties, chemical composition, and the resulting mechanical properties. All in the hope of coming up with further changes, and solutions for more improvement.

Definitions

Manganese (Mn) A deoxidizer and degasifier and reacts with sulfur to improve forgeability. It increases tensile strength, hardness, hardenability and resistance to wear. It decreases tendency toward scaling and distortion. It increases the rate of carbon-penetration in carburizing.

Carbon (C) The most important constituent of steel. It raises tensile strength, hardness, and resistance to wear and abrasion. It lowers ductility, toughness and machinability.

Sulfur (S) Improves machinability in free-cutting steels, but without sufficient manganese it produces brittleness at red heat. It decreases weldability, impact toughness and ductility.

Phosphorus (P) Increases strength and hardness and improves machinability. However, it adds marked brittleness or cold-shortness to steel.

Silicon (Si) A deoxidizer and degasifier. It increases tensile and yield strength, hardness, forgeability and magnetic permeability.

Copper (Cu) In significant amounts is detrimental to hot-working steels. Copper negatively affects forge welding, but does not seriously affect arc or oxyacetylene welding. Copper can be detrimental to surface quality. Copper is beneficial to atmospheric corrosion resistance when present in amounts exceeding 0.20%. Weathering steels are sold having greater than 0.20% Copper.

These are the main elements that make up the rebars, that are made at ÓAM Kft. and the table below contains the main mechanical properties that are measured during the rolling.

Table 1: Mechanical parameters

Magnitude	Symbol	Measurement unit	Description
Tensile strength	R_m	MPa (N/mm ²)	It is the ratio between the maximum applied force and the original cross-sectional area of the specimen
Upper yield strength	R_s	MPa (N/mm ²)	It is detectable only when the material has the yield phenomenon (it doesn't exist for the cold drawn and the stainless steels)
Yield point	R_p	MPa (N/mm ²)	It is detectable on cold drawn and stainless steel, in place of R_s
	$R_{p0.2}$	MPa (N/mm ²)	Load corresponding to a no proportional charge equal to a 0.2% of length L
	$R_{p1.0}$	MPa (N/mm ²)	Load corresponding to a no proportional charge equal to a 1% of length L
Flow stress	R_{eH}	MPa (N/mm ²)	Is the defined as the instantaneous value of stress required to continue plastically deforming a material - to keep it flowing
Elongation	A_{gt}	%	Permanent elongation of length L_0 , expressed in per cent of length L_0
	A_5	%	Permanent elongation for proportional specimens with length L_0 equal to 5 times diameter
	A_4	%	Permanent elongation for proportional specimens with length L_0 equal to 4 times diameter
	A_0	%	Permanent elongation for proportional specimens with length L_0 equal to 100 mm (used for diameter lower than 4 mm)

Production

First, in the EAF (Electric Arc Furnace) the scrap metals are melted, and alloyed primarily. After 60 minutes of melting, the molten steel is tapped into another cauldron, and then moved to the fine alloying, and deoxidizing station. From there, it is moved to the FAM (Continuous

Steel Casting), where it is casted into 130x130 mm 10 to 12 meter long billets. One process produces roughly 55 tons of steel, and one billet is around 1,2 tons.

Then the billets are loaded into the pushing furnace, and the rolling phase begins. The rolling mill consists of 18 rolls, numbered from 0 to 17, and is capable of producing rebar diameters between 8 mm and 40 mm. In this study my main focus is on the larger diameters, namely the 20, 25, 28, 32, and 40 millimeter ones.

Sampling

The sampling process of this project spanned over a year, and consisted of taking 3 samples from one rolling batch, that consisted of around 45 billets. The samples were taken at the beginning of the batch, the middle, and the end. The production parameters were recorded at each sample. The cooling parameters included:

- Furnace temperature
- Billet temperature before cooling
- Product temperature after cooling
- Water amount
- Water pressure
- Water temperature
- Rolling speed
- Opened nozzles

At the melting phase the chemical composition was also measured, and the main elements recorded were:

- C – carbon
- Mn – manganese
- Cu – copper
- P – Phosphorus
- S – Sulfur
- Si – Silicone
- The CE (equivalent carbon content)

Trials

During the initial trials, approximately two months, which contained two production campaigns. From these data we have concluded, that the most influential factors regarding the mechanical properties of our steel rebars are the following:

- CE, which raises the tensile strength, but negatively affects the elongation, the higher it is.
- The temperature after cooling, which raises the elongation, but negatively affects the tensile strength, the higher it is.
- The water amount used for cooling, which also raised the tensile strength, and yield strength, but lowered the elongation.

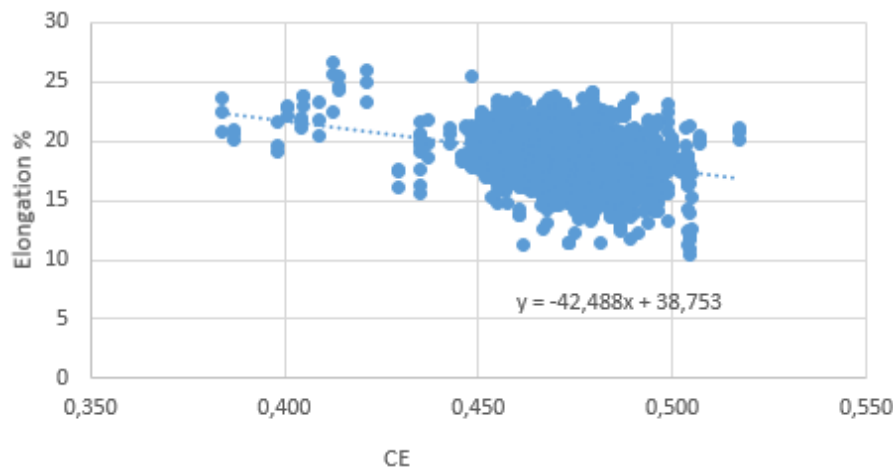


Figure 1: A₅ – CE.

After these conclusions, the the second trial followed, with changes made to the following parameters: Lowered the CE, fixated the water amount, to ensure a more constant cooled temperature in hopes of stabilizing the fluctuation of the mechanical parameters.

We also perceived relations regarding the diameters, because at the 32 mm diameter, the average elongation was 18.13 %, and the smaller the diameter got, the higher the average went, up to 19.01 %. This showed to be a relation with the cooling pad, because the higher diameters are harder to cool evenly throughout the whole piece of rebar.

The following trials in correspondence of the changes shown improvements, the dispersion mostly remained the same, but the average improved both in elongation, and tensile strength.

We also perceived relation between R_{eH} and A₅ elongation, which requires further investigation.

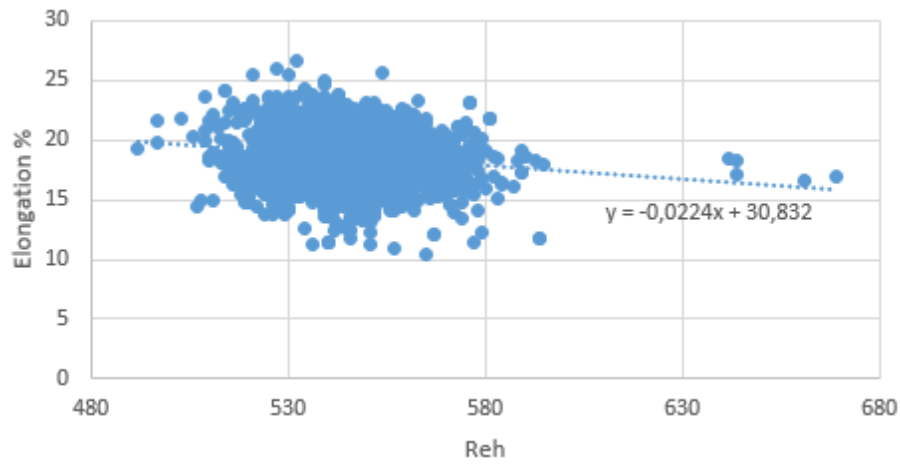


Figure 2: $A_5 - R_{eH}$.

Microscopic analysis

The microscopic analysis has shown, that the rim and the core of the samples are easily distinguished, separated from each other, with the core showing a fine ferrite-perlite structure, and the rim showing martensite.

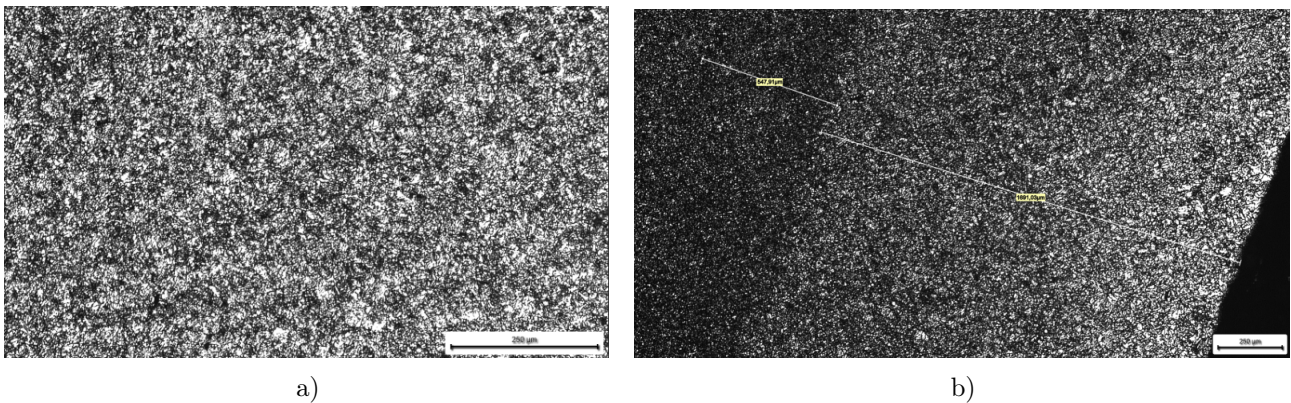


Figure 3: Microstructure a) core, b) rim.

During the microscopic analyses, we also conducted hardness test. The method was the Vickers hardness test, and it shown us, that the most optimal mechanical parameters were achieved, when the hardnes of the rim was greater with approximately 110 HV than the core.

Table 2: Mechanical properties

Sample	Diameter [mm]	F_{eH} [kN]	F_m [kN]	R_{eH} [MPa]	R_m [MPa]	A_{gt} [%]	Flux weight difference [%]	R_m / R_{eH}	A_5 [%]
P19	28	346.0	420.0	562.0	682.0	10.0	0.8	1.2	20.7
P20	28	336.0	412.0	546.0	669.0	12.4	-0.3	1.2	22.4

Table 3: Hardness results

Sample	Point of measurement	Diameter (mm)	Hardness (HV30)	Difference (HV)
P19	Rim	0.473	294,0	110.1
	in-between	0.500	222.5	
	Core	0.550	183.9	
P19	Rim	0.440	287,0	115.8
	in-between	0.490	231.7	
	Core	0.570	171.2	

Conclusion and further trials

The conclusion of the project for now is, that the most crucial factors regarding our rebars is the chemical composition, we will keep recording, and adjusting. In the rolling mill, another cooling pad will be installed around the middle of the process for a two-step cooling effect, in hopes of further improving the quality. We also have to find the optimal point for the flow stress, because it has the highest impact on the elongation, but we also need to keep in mind the tensile strength, and the ductility.

Microstructural transformations of DC01 carbon steel via cross-rolling process

Jawhara Marouani¹, Laszlo S. Toth^{1,2}, Máté Szűcs¹

¹ Institute of Physical Metallurgy, Metal Forming & Nanotechnology, University of Miskolc

² Université de Lorraine, CNRS, Arts et Métiers ParisTech, LEM3, F-57000 Metz, France

The rolled low-carbon steel DC01 sheets were manufactured by cross-rolling with five, ten, and thirteen passes in this study. The improvement of multi-cross-rolling on the microstructure of DC01 steel was investigated by optical microscopy (OM). The results indicate that the samples after rolling show how cross-rolling significantly affects both the arrangement of grains and mechanical properties. This influence leads to improve uniformity in the material's texture, reducing the reliance on specific directions for its mechanical properties.

Keywords: multi-pass Cross rolling, DC01 carbon steel, Microstructure.

1. Introduction

The properties of a material, both chemical and physical, are determined by its crystal structure [1]. Usually, the characteristics of the structure of single-phase materials [2], determine, in particular, the geometrical features of the component phases, such as grain shape and size, which significantly affect the properties of the material [3]. However, most of the studies have focused on high or medium-carbon steels. Low-carbon steels are also a type of widely used steels in industry. Therefore, from an application point of view, it is of great interest to synchronously obtain fine microstructures and excellent mechanical properties for low-carbon steels. Moreover, cross-rolling (CR) is one of the processes which are not very practical in current production environments [2].

Rolling is a method of reducing the thickness of a metal workpiece by passing it over two revolving rollers with a spacing smaller than the present workpiece thickness [1, 3]. Cross-cold rolling is used for steels to enhance hardness and strength, making it suitable for applications requiring high mechanical performance [2, 4]. The benefits of this process include reduced material waste, refined grain structure, and high-quality surface textures, making it an effective way to create metal sheets and strips with various desirable qualities [5]. Considering the above information, different starting microstructures have been subjected to cross-cold-rolling, instead of ferrite–pearlite structures to develop ferrite grain. The microstructure of such sheets depends strongly on the manufacturing conditions. Thus, it is necessary to establish a method of microstructural control by optimizing the manufacturing process [6]. Xin-jun Shen et al. [7] investigate how the initial microstructure affects the transformation and mechanical properties of critically rolled low-carbon steel plates. It investigates the relationship between the initial

microstructural condition and the resultant characteristics, providing information on the elements that influence the material's behavior throughout the rolling process. Shen et al. [8] investigate that the cross-rolling (CR) process can significantly improve the anisotropy of the rolled sheet, and the anisotropy improvement is better with an increasing number of passes and multi-pass rolling can effectively refine the grain size. Hamad et al. [9] showed that the number of grains with ultrafine sizes increased with increasing the amount of deformation introduced during rolling processing.

This work investigated the microstructural evolution of low-carbon steel DC01 during multi-pass cross-rolling. The samples underwent a 90° rotation around the normal direction (ND) between each rolling pass. This rotation causes the previous rolling pass' transverse direction (TD) to become the new rolling direction (RD) for the current pass.

2. Materials and Method

The low carbon rolled Steel DC01 thick sheets were used in this study. To obtain proper experimental materials, the rolled sheets were cut into the dimensions of 50 mm (RD1) × 50 mm (RD2) × 6 mm (ND) and then rolled on a Von-Roll symmetric rolling machine. The roll diameter was 220 mm, and the rolling speed was 14 m/min. The chemical composition examined by X-ray fluorescence (X-MET 8000 Expert) is detailed in Table 1.

Table 1: The chemical composition of DC01(wt. %).

Alloy	C	Mn	Al	Si	S	Pb	P
DC01	0.12	0.49	0.25	0.19	0.10	0.05	0.03

To obtain an optimal surface quality for microstructure characterization and enhance the indexation, specimens for Optical Microscopy (AXIO IMAGER M1M) observation were ground, polished, and finally chemically etched. The schematic diagram shown in Figure 1 illustrates the process of multi-cross-rolling.

The cross-rolling process is as follows: For each pass, the plate is rotated 90° around the normal direction, and then is reversely rotated 90° in the next pass. The two plates have been rolled for 13 passes, with a total reduction of 75.50% as shown in Table 2.

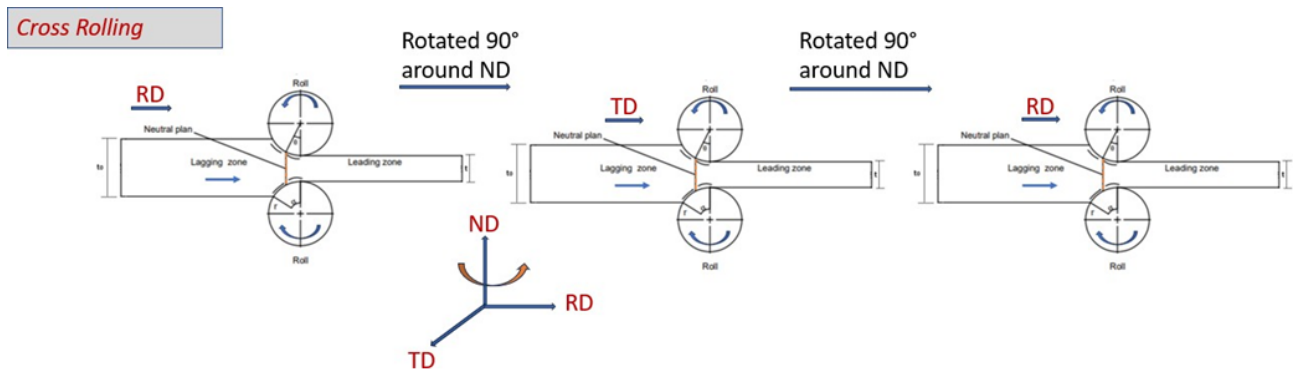


Figure 1: The schematic diagram of multi cross-rolling.

Table 2: Detailed process parameters in cross-rolling.

Passes	Thickness reduction		Total thickness reduction (%)
	Entry (mm)	Exit (mm)	
1	6.00	5.80	3.33
2	5.80	5.46	9.00
3	5.46	5.06	15.66
4	5.06	4.64	22.66
5	4.64	4.16	30.66
6	4.16	3.74	37.66
7	3.74	3.29	45.16
8	3.29	2.87	52.16
9	2.87	2.50	58.33
10	2.50	1.96	67.33
11	1.96	1.77	70.50
12	1.77	1.60	73.33
13	1.60	1.47	75.50

3. Results

3.1 Initial microstructure

Previous studies examined the effects of the height reduction per pass on the microstructure homogeneity of steel samples [10]. Figure 2 shows the initial microstructure of the low-carbon steel. The mean grain size was found using optical microscopy and was found to be 200 μm . The results of the OM photo indicate that except largely ferritic-pearlitic, which is a frequent property in low-carbon steels. Ferrite, with its soft and ductile qualities, serves as the structure's foundation, while pearlite, a lamellar arrangement of alternating ferrite and cementite layers, increases the steel's strength and hardness.

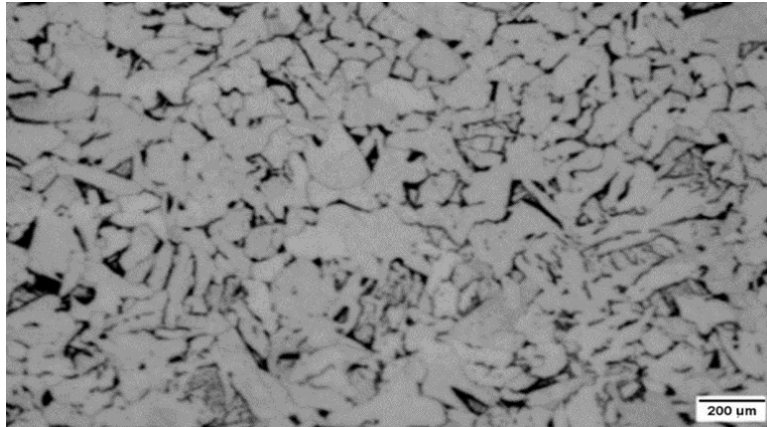


Figure 2: Initial microstructure of low carbon Steel.

3.2 Microstructure of cross rolling

Figure 3, 4 present optical microscope (OM) images taken from the RD1–RD2 plane of the CR rolled samples after a total height reduction of 75.5 % regarding the deformation level. After CR processing at a deformation level of 30 % (Figure 3a, Figure 4a), the deformed gains were elongated along the rolling direction and a set of parallel bands (deformation band) formed along the rolling direction of the steel processed by CR. With the increase of the deformation level imposed on the steel samples during CR process, the deformation bands became thinner, indicating that large plastic deformation occurred homogeneously during CR processing. The microstructure changes further a deformation level of 65 % (Figure 3b, Figure 4b), and exhibits grain alignment along the rolling direction with higher quantities of pearlite. Pearlite’s layered structure, which consists of alternating ferrite and cementite phases, adds to its high strength and hardness. After 75.5 % thickness reduction, the microstructure continues to grow (Figure 3c, Figure 4c). These modifications alter the mechanical characteristics of the steel.

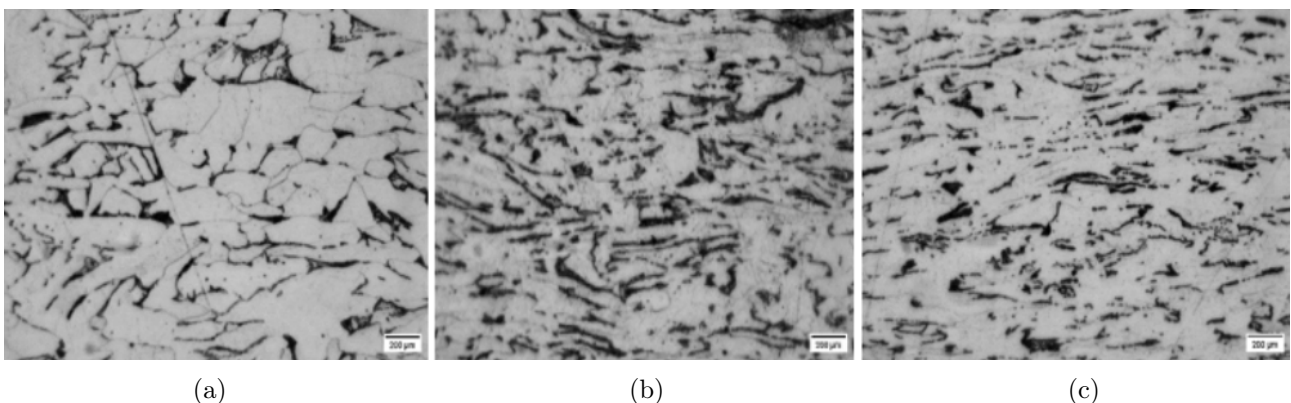


Figure 3: Effect of rolling reduction on the final microstructure of cross rolled steel RD1 according to Table 1 (a) 5pass, (b) 10pass, (c) 13pass.

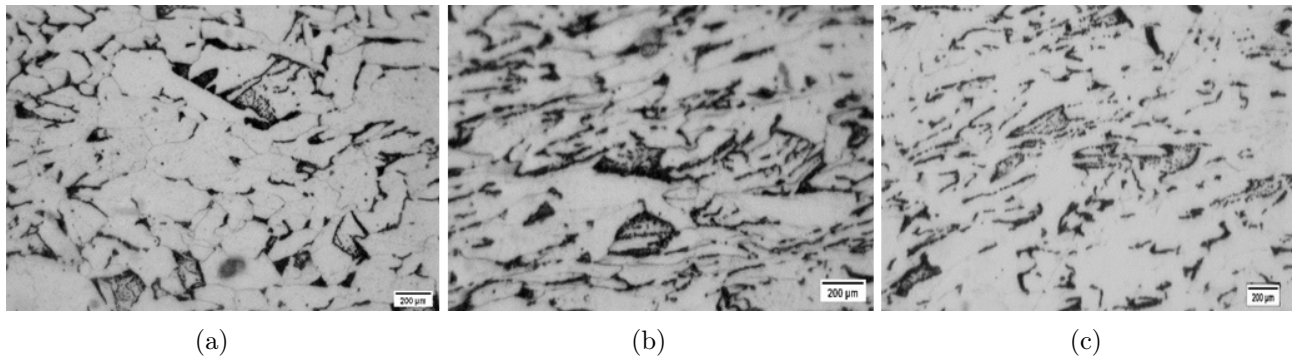


Figure 4: Effect of rolling reduction on the final microstructure of cross rolled steel RD2 according to Table 1 (a) 5pass, (b) 10pass, (c) 13pass.

4. Conclusion

In this work, the low carbon steel DC01 sheets were prepared by cross-rolling (CR). The effects of these methods on the microstructure and mechanical properties of the steel were investigated in detail. The result is concluded as follows: CR deformation level has a significant effect on the grain refinement evolution of steel. After a total height reduction level of 75.5 %, significant microstructural changes occur after and lead to grain alignment in different directions which could contribute to better isotropic mechanical properties.

5. References

- [1] K. Kowalczyk, M. B. Jabłońska, M. Tkocz, R. Chulist, I. Bednarczyk, and T. Rzychoń, ‘Effect of the number of passes on grain refinement, texture and properties of DC01 steel strip processed by the novel hybrid SPD method’, *Archiv.Civ.Mech.Eng.*, vol. 22, no. 3, p. 115, Apr. 2022, doi: 10.1007/s43452-022-00432-6.
- [2] Y. Xiong et al., ‘Effect of warm cross-wedge rolling on microstructure and mechanical property of high carbon steel rods’, *Materials Science and Engineering: A*, vol. 431, no. 1, pp. 152–157, Sep. 2006, doi: 10.1016/j.msea.2006.05.148.
- [3] K. J. Kim, D. Y. Yang, and J. W. Yoon, ‘Microstructural evolution and its effect on mechanical properties of commercially pure aluminum deformed by ECAE (Equal Channel Angular Extrusion) via routes A and C’, *Materials Science and Engineering: A*, vol. 527, no. 29, pp. 7927–7930, Nov. 2010, doi: 10.1016/j.msea.2010.08.084.
- [4] S. Dutta and M. Kaiser, ‘EFFECT OF ASYMMETRIC ROLLING ON FORMABILITY OF PURE ALUMINIUM’, *Journal of Mechanical Engineering*, vol. 44, p. 94, Jan. 2015, doi: 10.3329/jme.v44i2.21432.

- [5] S. Biswas, D.-I. Kim, and S. Suwas, ‘Asymmetric and symmetric rolling of magnesium: Evolution of microstructure, texture and mechanical properties’, *Materials Science and Engineering: A*, vol. 550, pp. 19–30, Jul. 2012, doi: 10.1016/j.msea.2012.03.099.
- [6] T. Ogawa, H. Dannoshita, K. Maruoka, and K. Ushioda, ‘Microstructural Evolution During Cold Rolling and Subsequent Annealing in Low-Carbon Steel with Different Initial Microstructures’, *J. of Materi Eng and Perform*, vol. 26, no. 8, pp. 3821–3830, Aug. 2017, doi: 10.1007/s11665-017-2849-6.
- [7] X. Shen, D. Li, J. Chen, S. Tang, and G. Wang, ‘The Effect of Initial Microstructure on Microstructure Evolution and Mechanical Properties of Intercritically Rolled Low-Carbon Microalloyed Steel Plates’, *steel research int.*, vol. 90, no. 11, p. 1900237, Nov. 2019, doi: 10.1002/srin.201900237.
- [8] T. Shen et al., ‘The improvement on mechanical anisotropy of AZ31 magnesium alloy sheets by multi cross-rolling process’, *Journal of Alloys and Compounds*, vol. 963, p. 171252, Nov. 2023, doi: 10.1016/j.jallcom.2023.171252.
- [9] K. Hamad, R. B. Megantoro, and Y. G. Ko, ‘Microstructure and texture evolution in low carbon steel deformed by differential speed rolling (DSR) method’, *J Mater Sci*, vol. 49, no. 19, pp. 6608–6619, Oct. 2014, doi: 10.1007/s10853-014-8280-6.
- [10] K. Hamad, B. K. Chung, and Y. G. Ko, ‘Effect of deformation path on microstructure, microhardness and texture evolution of interstitial free steel fabricated by differential speed rolling’, *Materials Characterization*, vol. 94, pp. 203–214, Aug. 2014, doi: 10.1016/j.matchar.2014.05.019.

Anodizing Challenges in High-Silicon Aluminum Alloy AlSi12Cu1(Fe): Microstructural Impact and Thickness Variation under Different Surface Conditions and Power Modes

Razzouk Emel^{1*}, Dániel Koncz-Horváth², and Tamás I. Török³

¹ PhD student, University of Miskolc, Institute of Chemical Metallurgy and Foundry Engineering

² Senior Research Fellow, University of Miskolc, Institute of Physical Metallurgy, Metal Forming and Nanotechnology

³ Professor Emeritus, University of Miskolc, Institute of Chemical Metallurgy and Foundry Engineering

* Corresponding author: razzoukemel@gmail.com

This study investigates the effects of anodizing on die-cast aluminum-silicon alloy AlSi12Cu1(Fe). The primary focus is on revealing surface modifications influenced by the as-cast microstructure and assessing how different surface conditions (as-cast, removal of 0.1 mm, 0.5 mm, and 1 mm) impact the thickness of the anodic layer. Furthermore, the study delves into the influence of varying power modes, such as steady-state voltage and steady-state current on both the anodic layer thickness and microstructure. The milled surface is associated with increasing the anodic layer thickness, and this increase was higher under the steady-state current mode. The microstructure and the anodic layer composition were closely similar in the two modes, where the composition plays a vital role in determining the anodic layer thickness and structure.

Keywords: diecast Al-Si-Cu alloy, Anodizing, Anodic layer, Microstructure.

1. Introduction

Die casting is a flexible method used to create complex metal components. Since the primary component that dissolves during anode corrosion is aluminium, all aluminum alloys will undergo anodization. Nevertheless, practical knowledge suggests that the anodization process of the substrate is affected by the presence of alloying elements, and the level of difficulty rises as the alloy becomes more intricate. Taking this into account, it is intriguing to observe that cast alloys are considerably more intricate than wrought alloy [1, 2]. Nevertheless, the cast type Al-Si alloys due to their favorable characteristics such as excellent castability, low shrinkage, and high specific strength [3, 4], are still widely utilized in the production of mechanical components occasionally having anodized surface finish as well. In recent times, certain eutectic or near-eutectic Al-Si alloys like AlSi12 and AlSi10Mg have emerged as highly promising materials for additive manufacturing of Al alloy products [5, 6]. However, the relatively low hardness and inadequate corrosion and abrasion resistance properties impose significant limitations on the durability of such Al-Si alloy products [7, 8]. Consequently, various surface technologies including

anodizing [9], laser remelting [10], plasma electrolytic oxidation (PEO) [11], and cathode plasma electrolytic deposition [12] have been employed to address these concerns.

2. Materials and methods

2.1. Materials

Samples of AlSi12Cu1(Fe) die-cast alloy were tested. The tested samples were cut from the original cast product as small specimens with a total surface area of 20 cm². The samples underwent polishing to remove varying amounts of material (0.1, 0.5, and 1 mm). Subsequently, the samples were affixed to a holder and positioned between two cathodes, situated at a distance of 7 mm. Both the sample holder and the cathodes were constructed from titanium. The sample numbers employed in the experiments are detailed in Table 1.

Table 1: Description the anodizing process parameters for tested samples.

Sample	Surface condition / flat surface	Anodizing state	Anodizing duration (min)	Theoretical current density _{max} (A * dm ⁻²)	Apparent charge (A * s)
V1	As-cast	SSV (35 V)	60	1.6	48
V2	Milled (-0.1 mm)	SSV (35 V)	60	2.3	56
V3	Milled (-0.5 mm)	SSV (35 V)	60	2.4	58
V4	Milled (-1 mm)	SSV (35 V)	60	2.8	74
C1	As-cast	SSC	60	1.6	90
C2	Milled (-0.1 mm)	SSC	60	1.6	90
C3	Milled (-0.5 mm)	SSC	60	1.6	90
C4	Milled (-1 mm)	SSC	60	1.6	90

2.2. Anodizing process

The first stage in the pre-treatment step is the degreasing process. Degreasing is a vital pre-processing step aimed at achieving optimal wetting characteristics, thereby promoting uniformity in subsequent processing steps on the substrate surface [13]. The degreasing solution used contained phosphates, borates, potassium hydroxide, moderately alkaline, and free of silicon compounds. The samples were immersed in this degreasing solution using an ultrasonic cleaning device for 10 min at 65 °C. After degreasing, the samples were rinsed in distilled water. The last stage in the pre-treatment was pickling, when the samples were immersed in the pickling solution containing 181.4 gl⁻¹ sulfuric acid, 8.1 gl⁻¹ Al, and 7 gl⁻¹ hydrogen peroxide for 15 seconds. Anodic layers were fabricated in the electrolyte contained 181.4 gl⁻¹ sulfuric acid, 10.6 gl⁻¹ Al,

and 7.1 gl^{-1} oxalic acid as well. A DC power supply unit (QPX600 Dual 600Watt) was used. The electrolyte was in continuous agitation and maintained at a temperature of 18°C .

3. Results and discussion

3.1. The anodic layer thicknesses

The scanning electron microscopy (SEM) technique is utilized for the measurement of the anodic layer thickness. Many measurements of the anodic layer thickness were conducted at various points. This was done due to the heterogeneous microstructure of the alloy and the potential defects present in the casting alloy. By applying a steady-state voltage (SSV) of 35 V, it is associated with a maximum current density of $1.6 \text{ A} \cdot \text{dm}^{-2}$. The anodizing power mode plays a crucial role in determining the anodizing thickness as demonstrated in Figure 1. The mode transition to steady-state current (SSC), while maintaining the same current density observed in the SSV experiment results in a higher anodic layer thickness compared to the anodic layer thickness produced under SSV for the as-cast surface, as depicted in Figure 1. Due to the fact that the anodizing process depends on the current density and the anodizing duration, we can expect a higher anodic layer thickness when the SSC mode is applied.

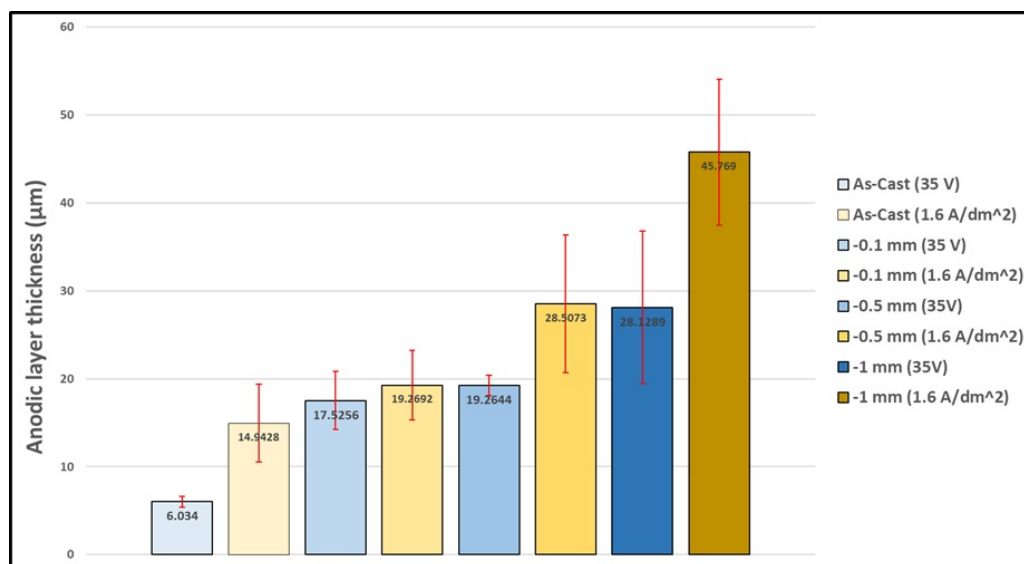


Figure 1: Variation of oxide layer thickness in the different experimental configurations.

In the case of the Al-Si cast alloy, the cooling rate significantly influences the microstructure of the surface region, particularly where there is a higher cooling rate than the bulk material. To investigate the impact of the skin layer on the behavior and growth of the anodic layer, some samples underwent milling to remove varying material depths (0.1, 0.5, and 1 mm). Subsequently, a SSV was applied in the anodizing process and some samples underwent SSC. Figure 6 illustrates

the anodic layer thickness across all scenarios. The anodic layer thickness increased with greater material removal through milling as shown in Figure 8. The data in Table 1 clearly show a link between the total applied charge to the samples and the thickness of the anodic layer. Under the SSV condition, a consistent rise in charge was observed when material was incrementally removed from the surface. This divergence stems from disparities in surface roughness and the composition of the alloy. These differences in surface characteristics contribute significantly to the observed variations in charge accumulation during the process, underscoring the impact of surface conditions on the overall electrochemical behavior. Different surface states could need different amounts of activation energy or starting charge to start the anodizing process; this is especially noticeable when comparing polished and as-cast surfaces.

3.2. The anodic layer composition

This alloy demonstrated in Figure 2 has a heterogeneous microstructure consisting of, eutectic, aluminium and intermetallic compounds. These microstructural differences cause the anodic layer growth rate to change. Furthermore, Figure 5 illustrates the variations in structural phase sizes in comparison to the bulk material. Thus, the removal of the surface region that has a finer structure is responsible for the observed rise in the anodic thickness. This phenomenon arises from rapid solidification compared to the bulk alloy.

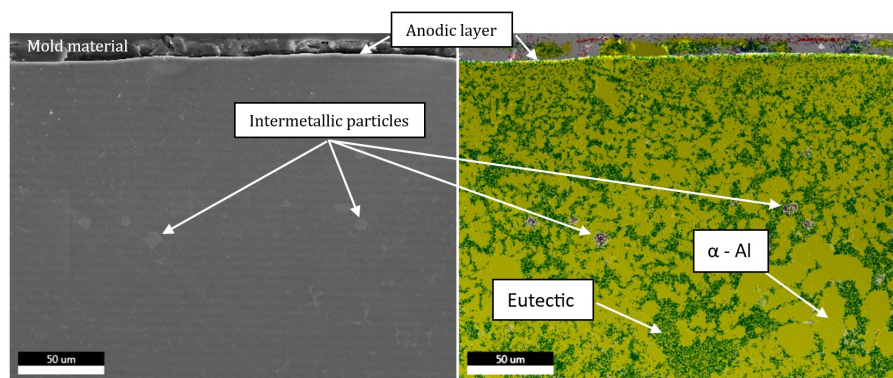


Figure 2: SEM-EDS map micrographs of the cross-section of the as-cast anodized sample under SSV mode using 20 V, the anodic layer thickness is 3 μm.

Figure 3 displays the EDS analysis of sample V3, highlighting key elements. Upon performing line analysis passing by darker region, a distinct silicon peak becomes evident compared to uniformly colored areas. At the interface, there's a decrease in oxygen and sulphur, while aluminium content increases. This observed behavior aligns with the typical formation of an oxide layer. Carbon can also be found in the anodic layer due to the use of an electrolyte that contains oxalic acid and from the preparation process prior to the SEM-EDS test. The distribution of carbon is shown in Figure 4. It is primarily found in the black areas of the

anodic layer that correspond to the cavities. Although minor amounts of carbon are detected throughout the cross-section.

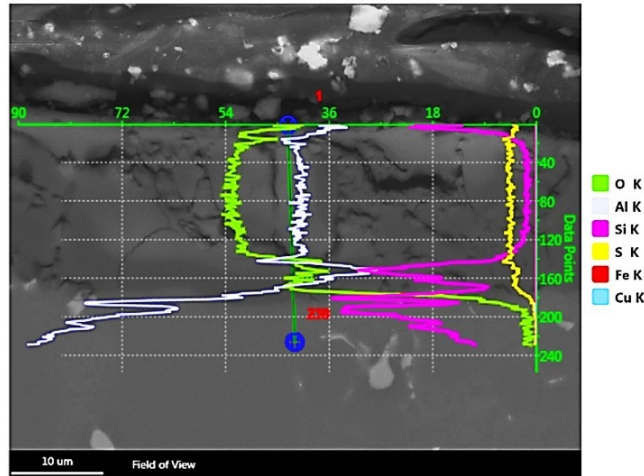


Figure 3: Element profile plot of the alloying elements for sample V3.

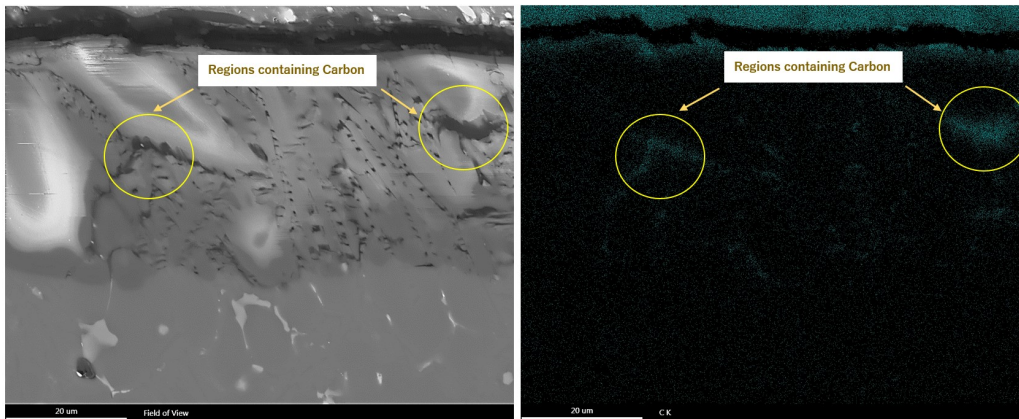


Figure 4: Carbon distribution in the cross section of sample V3.

3.3. The anodic layer composition

The anodization process of cast aluminum alloys leads to the formation of oxidized surfaces characterized by lower quality, primarily due to elevated levels of silicon (Si) and other elements like iron (Fe) and copper (Cu) [14]. The presence of surface defects, intermetallic, eutectic segregation, and surface liquid segregation (SLS), which are typical in die castings, induces alterations in the growth, composition, and microstructure of the porous anodic film [15]. In the case of SSV mode using 35 V, the as-cast surface, owing to its finer structure reveals smaller converted aluminium regions, whereas the removal of 0.5 mm of material exposes larger converted Al phase regions accompanied by cavity formation as shown in Figure 5. These cavities linked to the presence of eutectic silicon particles, manifest as larger in Figure 5b compared to 5a because they relate to the eutectic silicon particles, which are much finer in the as-cast surface.

Concurrently, cracks emerge in the converted Al phase. The structure of anodized samples in SSC mode exhibits the same characteristics. The anodic layer structure resulting from the as-cast surface and after removing 0.5 mm and 1 mm of material, respectively, is shown in Figure 6. Along with homogeneous sections—the converted aluminium—the structure also has inhomogeneous regions and black regions with varying lengths and widths.

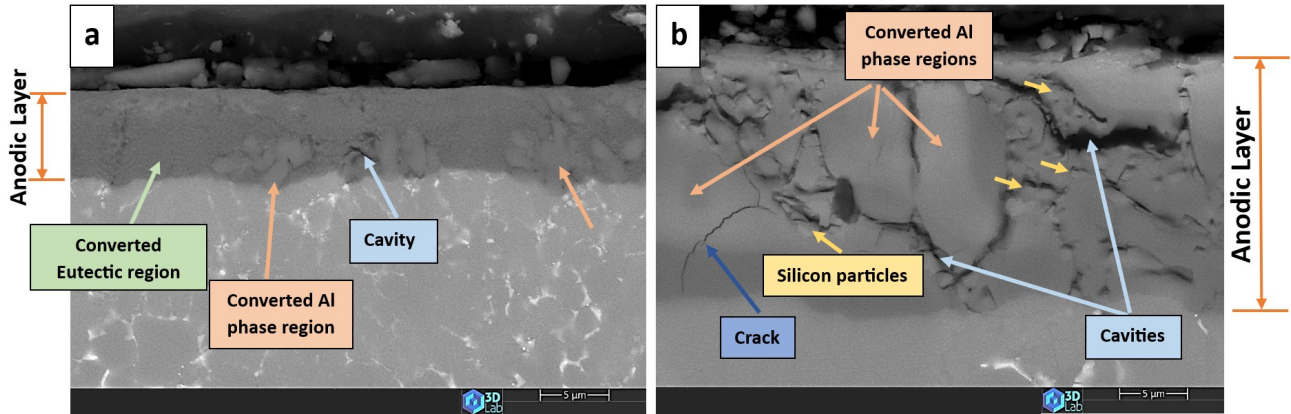


Figure 5: The anodized layer structure obtained under a steady-state voltage of 35 V. a) the as-diecast surface, sample V1. b) the milled surface, removing 0.5 mm of material, sample V3.

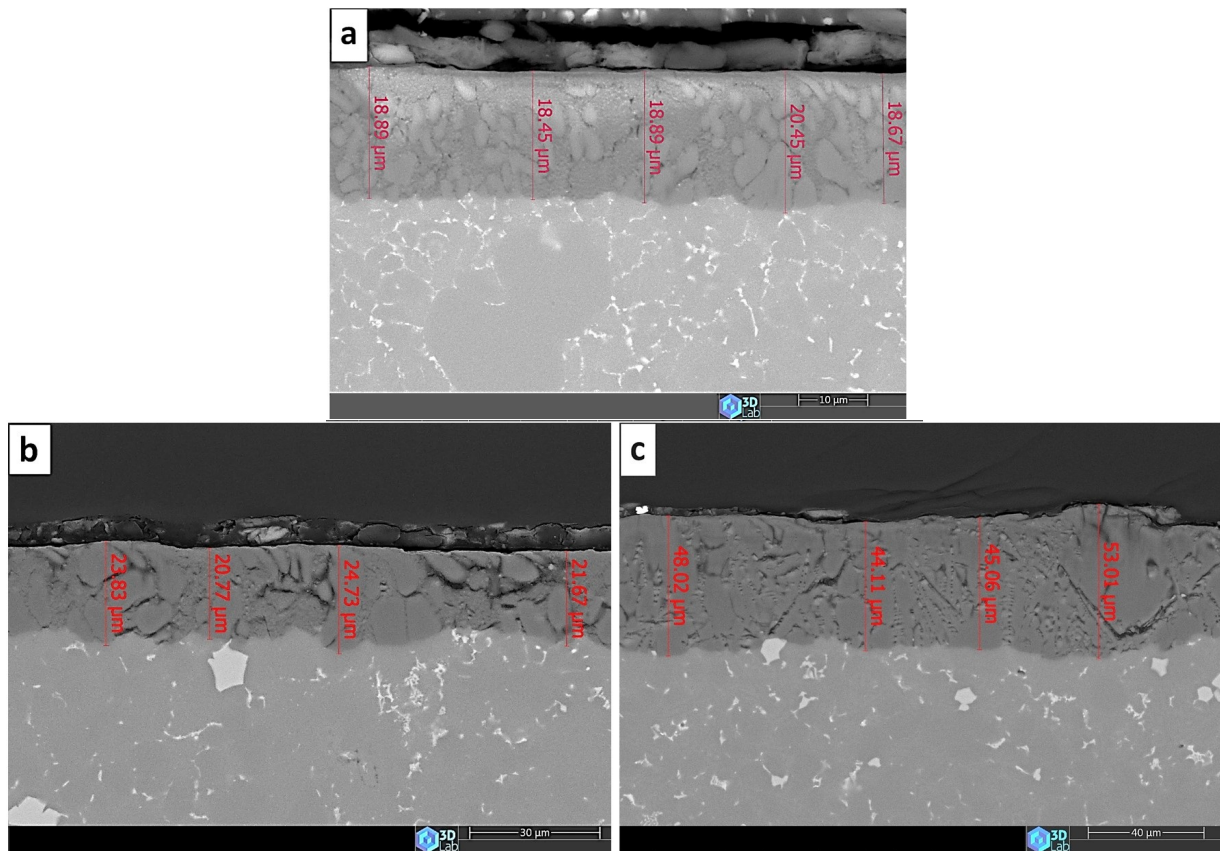


Figure 6: The anodized layer structure obtained under a steady-state current of 1.6 A/dm^2 for a) the as-cast surface, sample C1. b) the milled surface, removing 0.5 mm of material, sample C3. c) the milled surface, removing 1 mm of material, sample C4.

4. Conclusions

1. For the studied die-cast Al-Si alloy the anodic layer thickness increased following material removal by milling before anodizing. The amount of material removed up to one millimeter is directly correlated with the anodic layer thickness increase.
2. For die-cast Al-Si alloy, anodizing under steady-state current mode ($1.6 \text{ A} \cdot \text{dm}^{-2}$) resulted in a thicker anodic layer formation than anodizing under steady-state voltage mode (35 V, $1.6 \text{ A} \cdot \text{dm}^{-2}$ max) in all initial surface states (as-cast, milled) studied. These findings were substantiated by recording the total charge in both scenarios showcasing a direct proportionality between the anodic layer thickness and the total charge.
3. The alterations observed in the anodic layer thickness after surface milling can be attributed to shifts in the alloy composition.
4. Surface milling operations before the anodizing process result in larger cavity sizes and lengths. This phenomenon is directly linked to variations in the microstructure composition and the size of the forming phases.

5. References

- [1] Runge, J. M. (2018). The metallurgy of anodizing aluminum. Cham: Springer International Publishing.
- [2] Török, T. I. (2023). Anodizing surface treatments of aluminium alloys - Challenges and solutions (in Hungarian), BKL Bányászati és Kohászati Lapok, 156(1), 46-50.
- [3] Chen, J., Wen, F., Liu, C., Li, W., Zhou, Q., Zhu, W., ... & Guan, R. (2021). The microstructure and property of Al-Si alloy improved by the Sc-microalloying and Y₂O₃ nano-particles. Science and Technology of Advanced Materials, 22(1), 205-217.
- [4] Huang, J. M., Zhao, H. D., & Chen, Z. M. (2019). Microstructure and properties of A356 alloy wheels fabricated by low-pressure die casting with local squeeze. Journal of Materials Engineering and Performance, 28, 2137-2146.
- [5] Martin, J. H., Yahata, B. D., Hundley, J. M., Mayer, J. A., Schaedler, T. A., & Pollock, T. M. (2017). 3D printing of high-strength aluminium alloys. Nature, 549(7672), 365-369.
- [6] Cabrini, M., Lorenzi, S., Pastore, T., Testa, C., Manfredi, D., Lorusso, M., ... & Andreatta, F. (2019). Corrosion behavior of AlSi10Mg alloy produced by laser powder bed fusion under chloride exposure. Corrosion Science, 152, 101-108.

- [7] Rogov, A. B., Lyu, H., Matthews, A., & Yerokhin, A. (2020). AC plasma electrolytic oxidation of additively manufactured and cast AlSi12 alloys. *Surface and Coatings Technology*, 399, 126116.
- [8] Pezzato, L., Dabalà, M., Gross, S., & Brunelli, K. (2020). Effect of microstructure and porosity of AlSi10Mg alloy produced by selective laser melting on the corrosion properties of plasma electrolytic oxidation coatings. *Surface and Coatings Technology*, 404, 126477.
- [9] Zhu, B., & Zanella, C. (2019). Hardness and corrosion behaviour of anodised Al-Si produced by rheocasting. *Materials & Design*, 173, 107764.
- [10] Lien, H. H., Mazumder, J., Wang, J., & Misra, A. (2020). Microstructure evolution and high density of nanotwinned ultrafine Si in hypereutectic Al-Si alloy by laser surface remelting. *Materials Characterization*, 161, 110147.
- [11] Mora-Sanchez, H., Del Olmo, R., Rams, J., Torres, B., Mohedano, M., Matykina, E., & Arrabal, R. (2021). Hard anodizing and plasma electrolytic oxidation of an additively manufactured Al-Si alloy. *Surface and Coatings Technology*, 420, 127339.
- [12] Wang, P., Ma, Q., Yuwen, Q., & Li, J. (2019). The differences in the formation mechanism of PEO and CPED composited ceramic coatings on Al-12Si alloy. *Journal of Alloys and Compounds*, 788, 61-66.
- [13] S. Abrahami, 'Cr(VI)-free pre-treatments for adhesive bonding of aerospace aluminium alloys', doi: 10.4233/uuid:d5850b96-ec5b-4639-aac0-e05f81681800.
- [14] Zhu, B., Seifeddine, S., Persson, P. O., Jarfors, A. E., Leisner, P., & Zanella, C. (2016). A study of formation and growth of the anodised surface layer on cast Al-Si alloys based on different analytical techniques. *Materials & design*, 101, 254-262.
- [15] Tsangaraki-Kaplanoglou, I., Theohari, S., Dimogerontakis, T., Wang, Y. M., Kuo, H. H. H., & Kia, S. (2006). Effect of alloy types on the anodizing process of aluminium. *Surface and Coatings Technology*, 200(8), 2634-2641.



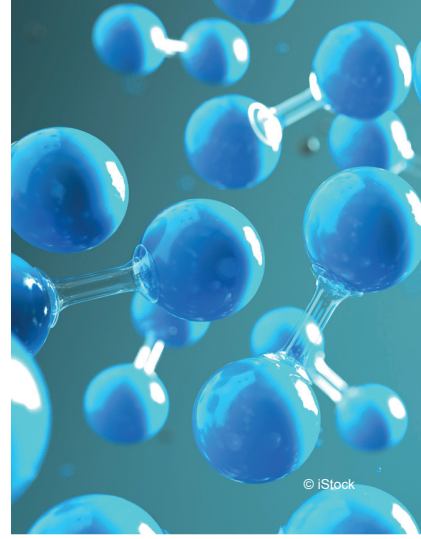
Stahl

Steel Institute VDEh
Commitment to Steel

www.vdeh.de

www.study-metallurgy.vdeh.de

© SMS



© iStock



© TKSE



© MU Leoben



greentec
steel

greentec steel
UNSER WEG IN EINE GRÜNE ZUKUNFT

Innovationen für die Stahlerzeugung von morgen.

www.voestalpine.com/greentecsteel

voestalpine
ONE STEP AHEAD.

Comparative study of inclusion modification with calcium for structural steel grade S235JR + N

Ramóna Veszprémi¹, Miklós Palkovics², Gábor Szabó¹

¹ University of Miskolc, Institute of Metallurgy and Foundry Engineering, 3515 Miskolc Egyetemváros, Hungary

² Liberty Dunaújváros, Department of Technology, 2400 Dunaújváros Vasmű tér 1-3, Hungary

I investigated the effect of calcium treatment on the inclusion morphology of secondary metallurgy. Furthermore, I included a batch produced according to a common steelmaking technology in my research, which made it possible to compare the inclusion contents of the two batches

Keywords: inclusion, calcium, inclusion content, mechanics, technology

1. Introduction

In our present day, the demand for steel is on the rise again. Both the European Union and Hungary's steel usage is increasing, however, the European Union's increasingly strict environmental directives require manufacturers to reduce their specific emission values to a lower level. One possible way to reduce specific CO₂ is to reduce our own waste (scrap ratio) generated during production, and shift production not towards quantity, but towards quality products. Since the formation of inclusions is inevitable during steel production, it is important at what phase and at what point in production these inclusions are identified, that is, the sooner an inclusion (and thus a possible downgrade) can be identified, the further processing (e.g., re-rolling) and the amount of energy required for it (indirectly CO₂ emissions) becomes unnecessary.

The hard inclusions, such as certain oxides and nitrides, significantly degrade resistance to fatigue. While most sulfide inclusions are ductile, which can be advantageous for fatigue resistance. However, the malleable sulfides elongate longitudinally during rolling, resulting in an anisotropic property. This means that different directions in space exhibit different physical parameters, such as hardness and conductivity. The effect of inclusions depends not only on their type but also on their size, spatial distribution, and quantity.

During my research, I examined the effect of calcium treatment used during secondary metallurgy on the morphology of inclusions. Furthermore, I also included a batch produced according to a common steel production technology in my research, which allowed me to compare the inclusion content of the two batches.

Structural steel grades S235JR + N according to EN 10025-2:2019 standard, produced by both calcium treatment and conventional steelmaking technology, were compared. Consequently, I

plan to perform mechanical and inclusion tests on samples taken from various production phases of ISD Dunafer Zrt., from which I intend to determine the effect of calcium treatment on the steel's inclusion content and the mechanical properties of the finished product.

The examined batch treated with calcium received coil number E31766, while the batch produced according to the conventional technology received coil number E31769. Subsequently, I intend to identify each batch by indicating the coil number.

2. Comparison of the inclusion content of steels produced according to conventional technology and treated with calcium

In the case of both coils, samples were extracted from the beginning, middle, and end for testing. For inclusion analysis, one sample was cut from each test specimen.

For easier comparison of the inclusion content of the examined coils, I have depicted on a common diagram (Figure 1) the inclusion content, types, and degree numbers of the two coils.

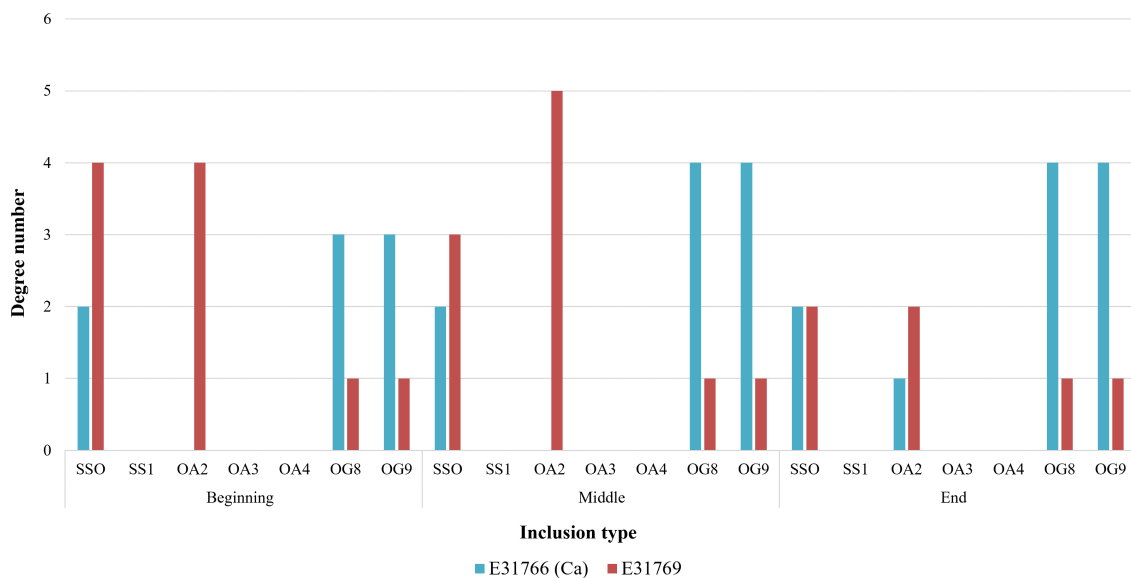


Figure 1: Comparison of the inclusion content of the two coils.

It can be observed in Figure 1 that the coil manufactured according to the conventional technology (E31769) typically contains spherical oxide inclusions (OG8-OG9) of degree 1, as well as linearly arranged sulfide inclusions (SS) of degrees 2, 3, and 4. In addition, the samples mainly contained aluminium oxide (OA2) inclusions of degrees 2, 4, and 5, which were arranged in rows due to the hot forming process. In contrast, no aluminium oxide inclusions were found in the inclusion samples of the coil treated with calcium (E31766), and we typically detected spherical oxide inclusions of degrees 3 and 4. According to the literature, the modification of

inclusions with calcium can be considered successful if there are no separate aluminium oxide inclusions in the steel, and if the degree of the inclusions does not exceed 3. Since we did not find any separate aluminium oxide inclusions in the coil treated with calcium, the treatment can be considered successful from this aspect. However, the spherical oxide inclusions of degree 4 detected in the steel treated with calcium exceed the recommendation of the literature, so a clear success - regarding the calcium treatment - cannot be concluded. According to the relevant literature, the success of the calcium treatment can also be judged by the mechanical tests of the sheets, namely, the values of the longitudinal and transverse impact work should be almost identical, so I also performed additional mechanical tests to decide on the success of the calcium treatment.

3. Evaluation of mechanical results

In both coils, the test plates were cut out from the beginning, the middle, and the end. From each test plate (beginning, middle, end), 2 longitudinal and transverse tensile samples were cut out from the operator side, the middle of the plate, and also from the drive side, along with 1 longitudinal and transverse sample necessary for impact testing.

The EN 10025–2:2019 standard states that for the S235JR + N structural steel specification, the values of the upper yield point, tensile strength, and elongation at break are qualifying for the transverse samples, while for the impact test, the values of the longitudinal samples are qualifying.

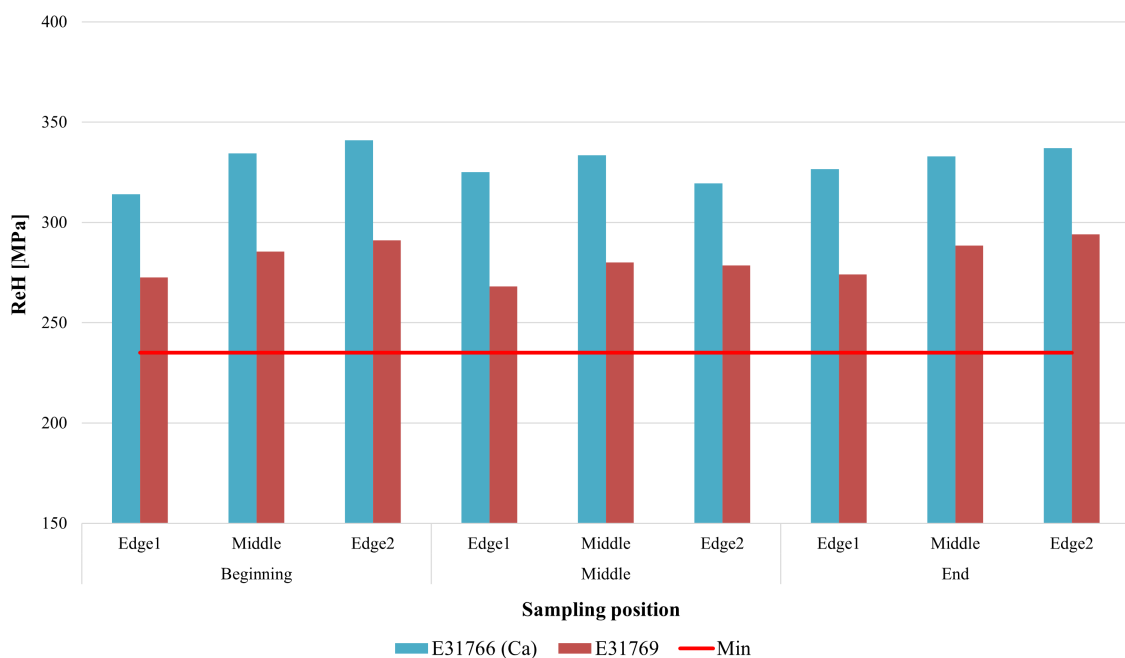


Figure 2: Comparison of upper yield strength – transverse direction.

In Figure 2, the upper yield strength values of the calcium-treated E31766 and the conventionally produced E31769 coils are compared along the width and length of the strip. The standard lower tolerance limit (235 MPa) is indicated on the diagram.

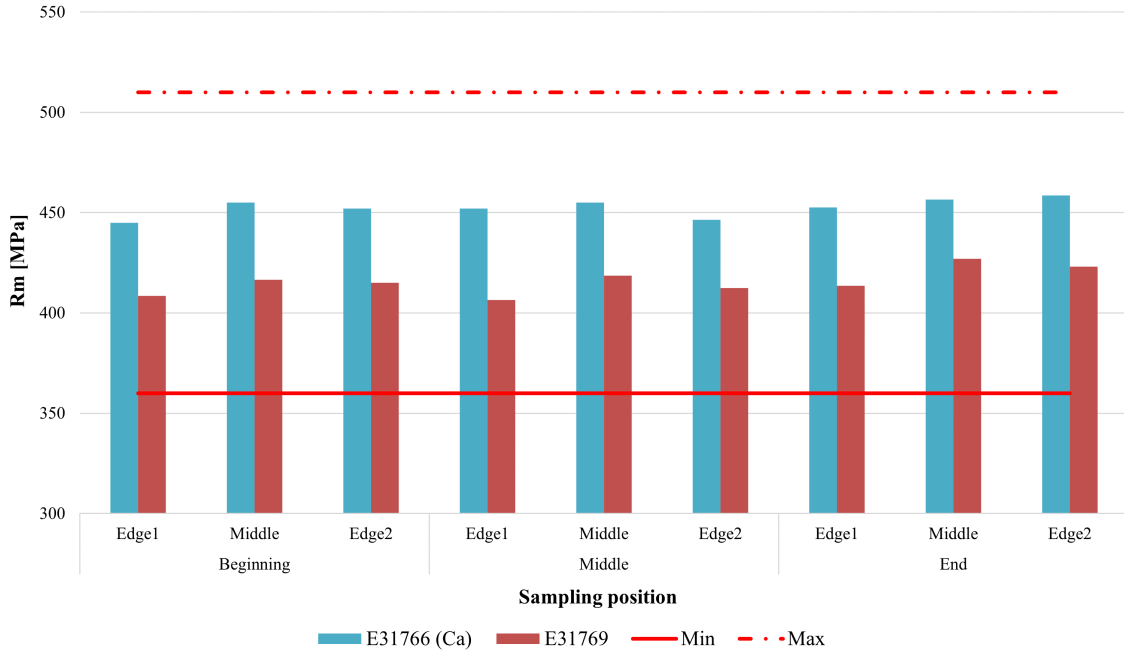


Figure 3: Comparison of tensile strength – transverse direction.

In Figure 3, the values of tensile strength are displayed along the width and length of the strip, indicating the minimum (Min) and maximum (Max) values prescribed by the standard (360 – 510 MPa).

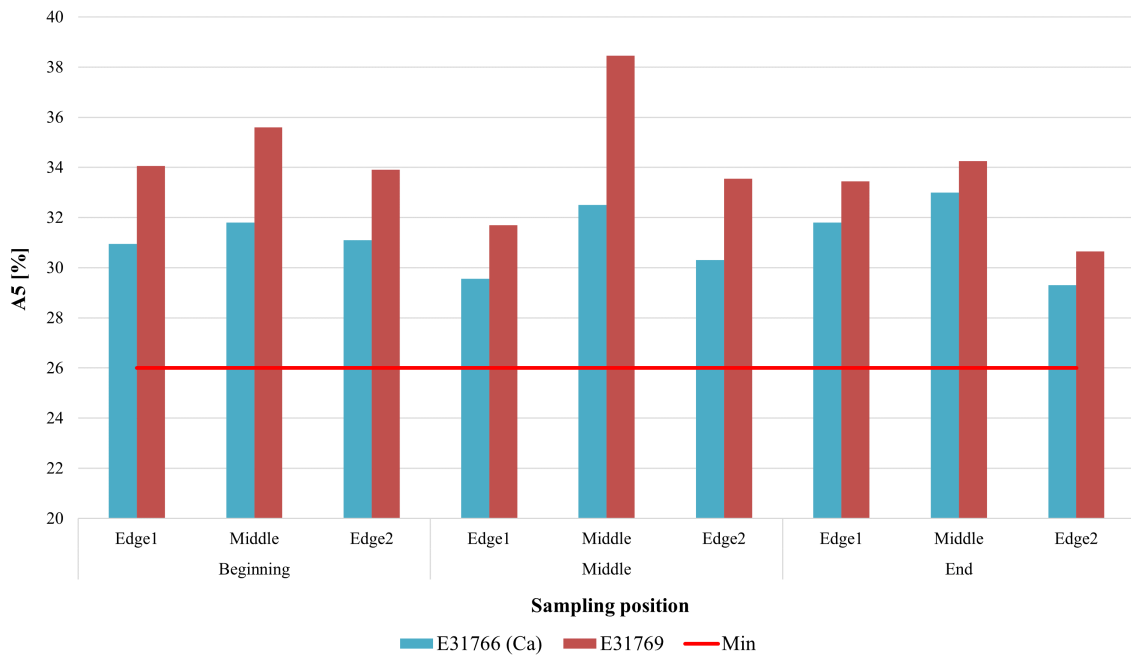


Figure 4: Elongation at break comparison – transverse direction.

The comparison of the elongation at break values of the coils produced according to the conventional technology and treated with calcium is shown in Figure 4, along with the lower tolerance limit (26 %) prescribed by the standard.

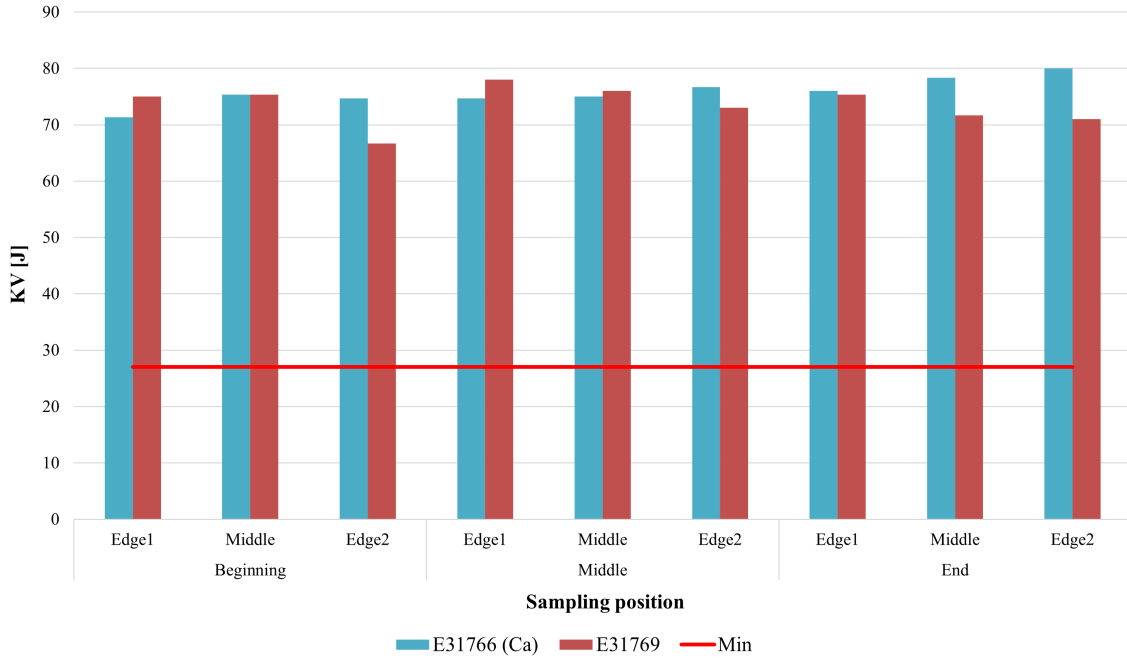


Figure 5: Comparison of impact test values –longitudinal direction

In Figure 5, the comparison of impact test values can be observed, with the minimum value (27 J) according to the standard indicated.

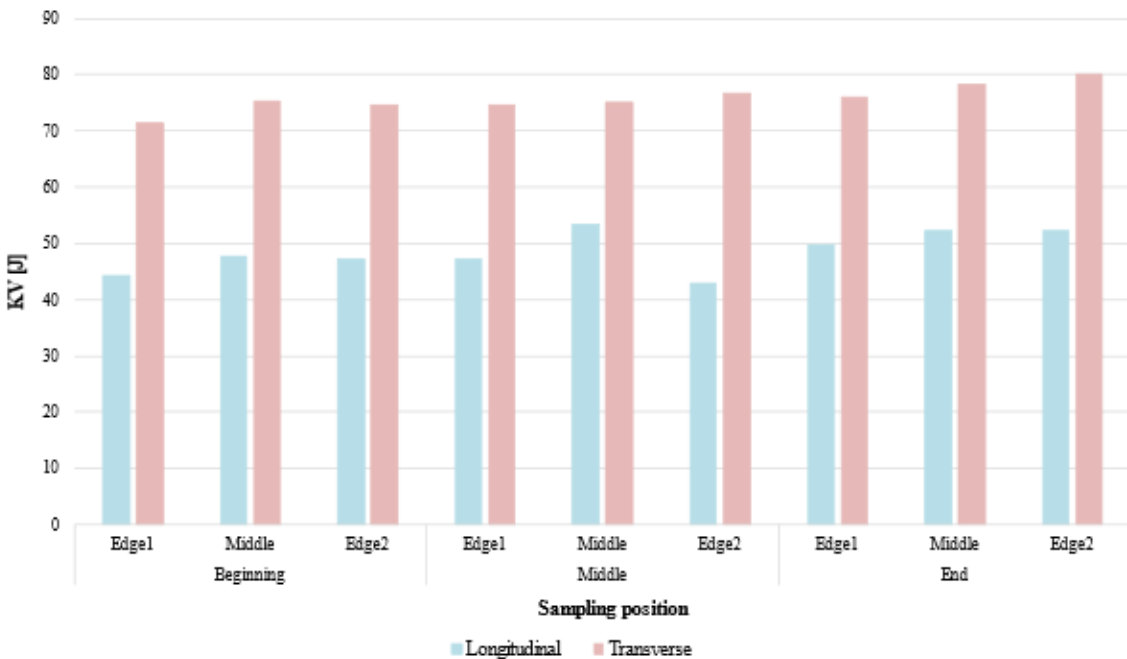


Figure 6: Comparison of the cross and longitudinal impact test values of coil number E31766

It is clearly evident that the strength properties of the calcium-treated samples are significantly higher than the results obtained from samples taken from coils produced using conventional technology. The calcium-treated samples exhibit approximately 30–50 MPa higher upper yield strength (Figure 2) and 20–40 MPa higher tensile strength values (Figure 3). Meanwhile, a clear decrease in toughness properties (elongation at break) is observed (4–8 %) in parallel with the increase in strength characteristics. The reason for this is not the calcium treatment but the different thicknesses of the two coils, as well as the temperature gradient due to the different thickness group classifications (I and II thickness groups) of the two coils in the continuous annealing furnace. The only difference in the temperature gradient between the I and II thickness groups is in the coiling temperature, where there is a marginal difference of 70 °C. The calcium-treated coil with a thickness of 6.00 mm was coiled at 573 °C, while the conventionally produced coil with a thickness of 7.00 mm was coiled at 647 °C.

There was no significant difference observed in terms of impact toughness between the two coils (Figure 5). According to the literature, I compared the longitudinal and transverse impact test values in Figure 6, as the literature formulated the success of calcium treatment by stating that the values of longitudinal and transverse impact toughness should be close. However, in Figure 6, a considerable difference was evident between the longitudinal and transverse impact test values, differing by approximately 20–30 J. Based on these research findings, I could not support the literature's thesis in this regard.

4. Summary and Conclusion

My research topic involves investigating the impact of calcium treatment on the inclusion morphology during secondary metallurgy. In my thesis, I compared structural steel grades S235JR + N, treated with calcium, and those produced according to the conventional steelmaking technology specified in the EN 10025–2:2019 standard.

In the case of the calcium-treated batch, an additional cost was incurred during secondary metallurgy treatment. A total of 314 kg of CaFe wire was used for the calcium-treated batch, with an average cost of 909,000 HUF/ton for the CaFe wire over the 1-8 month period. Consequently, the production of the calcium-treated batch resulted in an additional cost of 285,426 HUF compared to the production of the normal S235JR + N batch.

Based on my research, during secondary metallurgy treatment, when the appropriate ratio of Ca-Al oxides is achieved, calcium effectively modifies Al_2O_3 inclusions. This is supported by the fact that in the coil produced from the calcium-treated batch, we did not detect Al_2O_3 inclusions; however, a higher grade of spherical oxide inclusions was observed compared to the coil produced using conventional technology. Additionally, in the calcium-treated coil, we found

a lower grade of sulfide inclusions than in the coil produced with normal technology. Since Ca modified Al_2O_3 inclusions into spherical oxide inclusions, which exhibit favorable properties during hot forming compared to Al_2O_3 inclusions, despite limited available data, it can be concluded that calcium treatment is considered successful.

In the coil produced by conventional technology, inclusions of Al_2O_3 with grades ranging from 2 to 5 were observed. However, despite this, no differences or deviations were found in the measured production technological parameters between the coils rolled and cut from the two batches. Both literature and practical experience indicate that among the non-metallic inclusions remaining in the steel, brittle Al_2O_3 inclusions break up and align during hot rolling, while ductile manganese sulfide inclusions form into flakes or threads. Both types of inclusions are extremely hazardous to the final product, causing mechanical anisotropy and surface cracking during bending of the steel sheet. Therefore, considering these facts, introducing calcium-charged CaFe wire during secondary metallurgy treatment is advantageous. However, due to the additional cost, it should be applied by the company only in cases where the customer subjects the manufactured product to complex forming operations.

It would have been advisable to further investigate the formability of the finished products produced by conventional technology and those treated with calcium in terms of the developed inclusion morphology. Through additional research, it could be systematically and purposefully established in the respective Vertical Manufacturing Instructions which VGYU's require calcium treatment. An example of such direction could be in the case of steel grades intended for automotive applications or those intended for complex forming purposes, where the application of calcium treatment might be justified.

Rolling Process Variation Estimation Using a Monte-Carlo Method

WEINER Max^{1,a*}, RENZING Christoph^{1,b}, SCHMIDTCHEN Matthias^{1,c}, PRAHL Ulrich^{1,d}

¹ Institute of Metal Forming, TU Bergakademie Freiberg, Germany

^a max.weiner@imf.tu-freiberg.de, ^b christoph.renzing@imf.tu-freiberg.de

^c matthias.schmidtchen@imf.tu-freiberg.de, ^d ulrich.prahl@imf.tu-freiberg.de


No technical process is totally certain, but subjected to uncertainties. They may originate in the process itself or in the input materials and determine the precision of the product. Two questions are here especially of interest: 1) How do variations in the input workpiece evolve within the process? 2) Which process steps are crucial to influence this behavior? Answers to these questions can be obtained by analyzing production data or by numerical methods. The usage of Monte-Carlo-methods for estimation of variations and tolerances is a well proven approach in some fields, but was first applied by the authors to rolling processes. The inputs are all varied at once by drawing random samples from given distributions, so cross-dependencies are included in the analysis. The method has the favor of general applicability, i.e. the simulation procedure can be regarded as black box. So, the method is generally agnostic to the used simulation core, but needs a large number of simulation evaluations, so fast simulation models are favorable.

Keywords: Rolling, Simulation, Monte Carlo, Precision, Tolerance, PyRoLL.

Introduction

The term Monte Carlo Method (MCM) generally refers to a class of methods, which are characterized by the use of random numbers. These methods are rather diverse and serve different purposes. Here, the term shall be used for the concept of drawing random numbers as input for a function and analyzing the results of several evaluations of this function, with different random inputs, with statistical methods. A detailed overview on this type of Monte Carlo methods is given by [1]. The nature of the function can be complex, even of a black-box type, where nothing about the internals of the function is known but the input and output interfaces. In this case, Monte Carlo methods can provide valuable information about the behavior of the function while altering inputs.

Here, the function equals the simulation procedure, so it is generally known, but complex. For example, it is generally not possible, to compute derivatives of the outputs in dependence on the inputs in an analytical way. Even numerical derivation is hard, due to the multi-dimensional nature of most natural or technical systems.

 Content from this work may be used under the terms of the Creative Commons Attribution 3.0 license. Any further distribution of this work must maintain attribution to the author(s) and the title of the work, journal citation and DOI. Published under license by Materials Research Forum LLC.

The use of Monte Carlo methods for the analysis of variations in technical processes was reported before in the field of assembly of complex structures, like in mechanical engineering and building construction (f.e. [2–7]). The authors have previously used a similar approach to model powder morphology influences in sintering processes [8, 9]. In [10] the authors showed the difference between variations originating in the input workpiece and within the process. Were the first tend to vanish along the process, the latter tend to accumulate. Here, the efficiency of input variation elimination shall be regarded more detailed to help identifying crucial points to act on in the process regarding variational behavior.

Rolling simulation is currently dominated by the use of finite element (FE) based models. These are offering high accuracy and high-resolution results at the expense of high computational resource usage. So, these methods are inconvenient for the current need, as a Monte Carlo based analysis of a rolling process needs hundreds to thousands of simulation runs, depending on the count and variance of inputs, as well as the sensitivity of the process. Therefore, one-dimensional approaches shall be used here. These offer less accuracy and limited resolution, but are computable within fractions of seconds on typical personal computer systems. The current work uses the open-source rolling simulation framework PyRoLL [11] as simulation core, which is developed by the authors. PyRoLL is a fast, open and flexible software package mainly aimed at groove rolling in reduction passes. The models used for the different parts of the problem can be exchanged and extended with low effort to the users' needs.

Methods

The Institute of Metal Forming operates a semi-continuous pilot rolling plant, which is the object of the current investigation. It consists of a two-high reversing roughing stand and four continuous finishing stands. The pass schedule of the current work consists of 10 oval-round reversing passes followed by 4 oval-round continuous finishing passes. A 50 mm round workpiece made of a mild structural steel is rolled down to 8 mm diameter. The detailed properties of the schedule are of minor importance for the statements of this work and are therefore left out here.

Monte Carlo Approach. The basic idea of the approach shown here is to simulate the rolling process several times with different input values, which are drawn by a random number generator according to predefined statistical distributions. Afterwards, the distribution of the results can be analyzed by classic methods of descriptive statistics to obtain information about the process' variational behavior. The principle is shown in Figure 1. This approach provides information about the overall variational behavior of the process. If a single source of variation is introduced in the input, the reaction of the process on this variable can be analyzed. If needed, several input variables can be varied at once to regard their combined influence. The tracing back

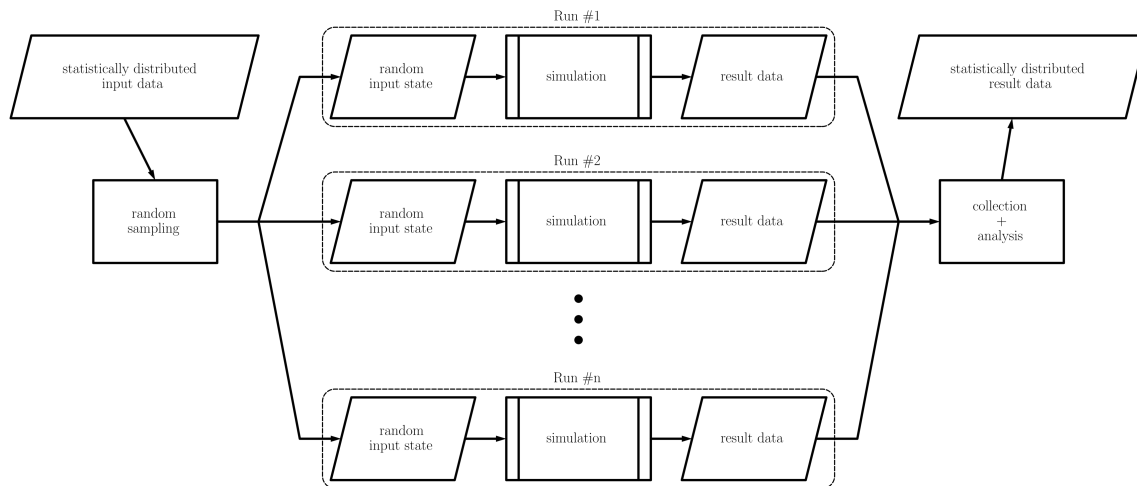


Figure 1: Chart of the Concept of Variation Estimation Using Monte Carlo Techniques.

of result variations to the input can be done using classic correlation methods of descriptive statistics, however, with the same typical caveats. The main benefit of the approach is, that no information about the internals of the simulation procedure is needed for variational analysis, especially there is no need for derivatives of result values in dependence on the input. The simulation procedure can generally be treated as black box with defined input and output interfaces.

Core Simulation Procedure. In the current work, the open-source rolling simulation framework PyRoLL [11] was used to simulate the rolling process. PyRoLL provides a large library of model approaches to the partial problems of a rolling process. Here, models combining empirical approaches with simplified analytical solutions were used, because of their low computational effort. The simulation was done with the basic configuration of PyRoLL, which includes the empirical roll force and torque model of Hensel and Spittel [12], an integral thermal model approach according to Hensel and Poluchin [13], contact area estimation according to Zouhar [14] and roll flattening according to Hitchcock [15]. Spreading was simulated using the equivalent flat pass method according to Lendl [16–18] in conjunction with the spreading equation of Wusatowski [19]. These models are well known and proven approximate approaches to the simulation of elongation passes. Details of software construction and model equations are provided in the documentation of PyRoLL [20].

Results and Discussion

Depending on the regarded varied input values, proving the validity of absolute variances calculated by this method in comparison with experimental results is quite hard, since one has to include all major variation sources and describe them by appropriate probability distribution functions. One attempt to this was made in [10] by modelling uncertain inter-pass durations due to manual handling. Here, the inter-pass durations are taken as certain and the sole variations applied are in the input workpiece to trace their evolution through the process line.

A commonly found statement from practical experience is, that the variation in the input workpiece is equalized after 3 to 4 passes. To prove this statement, several amounts of input workpiece variation in diameter and temperature were used to simulate the variational behavior with the Monte Carlo approach. The distributions of input diameter and temperature were assumed as normal with standard deviations chosen to be 1%, 2%, 5%, and 10% of the mean input value.

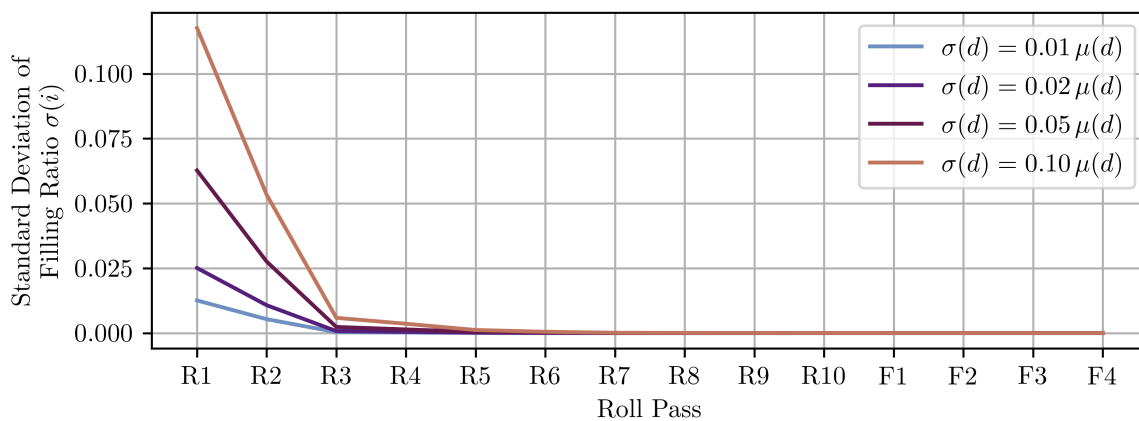


Figure 2: Evolution of Filling Ratio Deviation with Different Initial Standard Deviations of Diameter.

The variation of input diameter was investigated by regard on the filling ratio (the ratio of current profile width to usable/nominal width of the groove) in each pass as shown in Figure 2. The figure shows the standard deviation of filling ratio at the output of each pass. One will notice that the standard deviation of the filling ratio decreases rapidly in the first passes and is almost equalized after the third pass, no matter which initial deviation was used. So, for the matters of shape the initial hypothesis can be confirmed. Regarding the workpiece temperature the case is different. Figure 3 shows the standard deviations of workpiece temperatures before and after each pass. The deviation of workpiece temperature also decreases with each pass, but less rapidly. Different initial deviations are not equalized within the process, high input variations remain remarkable till the end of the process. Note, that deviations in workpiece temperature highly influence the evolution of the microstructure and therefore the product material properties. It can be stated, that shape deviations in input are of minor importance,

because they are efficiently equalized in the rolling process. However, deviations in temperature tend to be still remarkable in the output workpiece.

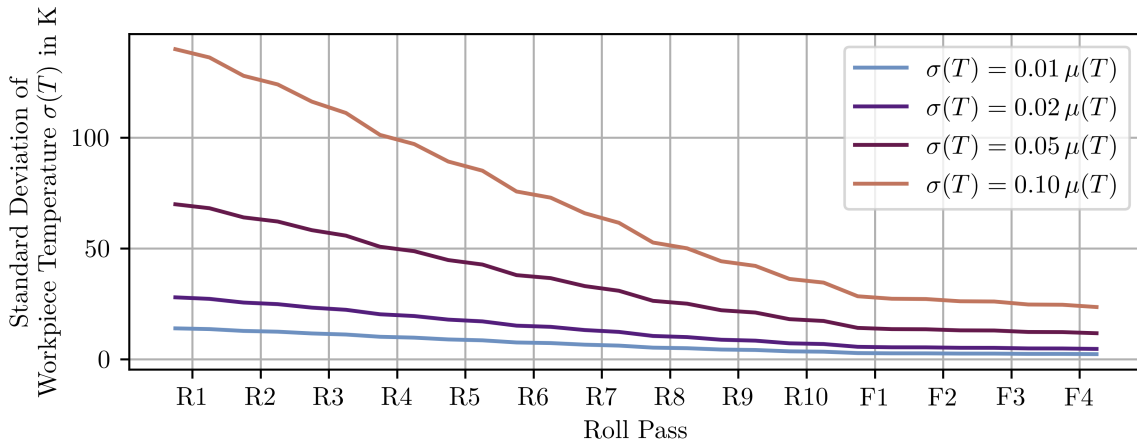


Figure 3: Evolution of Workpiece Temperature Deviation with Different Initial Standard Deviations of Temperature.

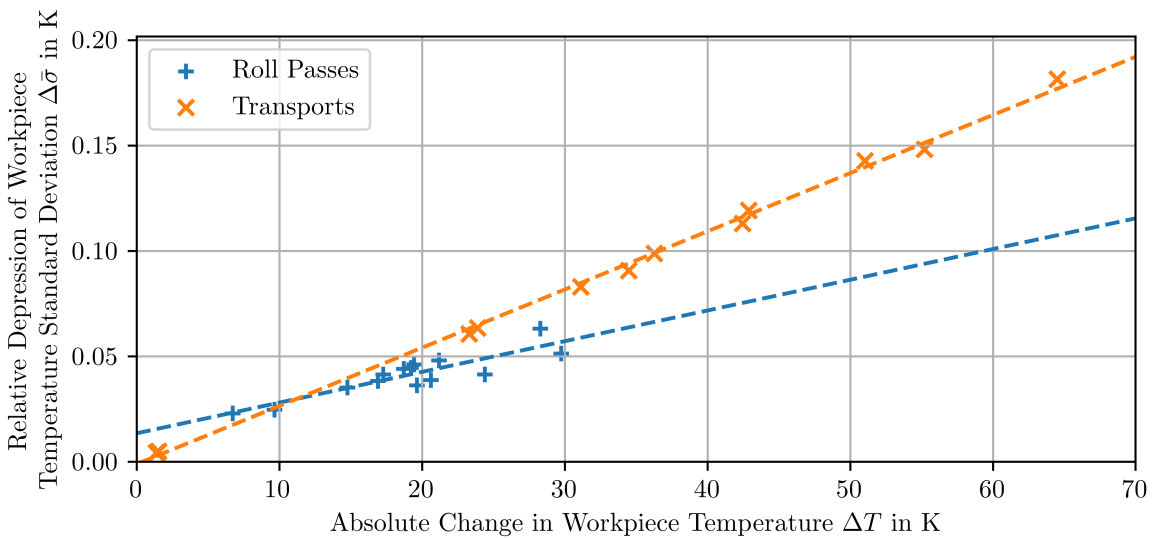


Figure 4: Correlation Between Temperature Change and Variation Elimination.

Also, it can be observed in Figure 3, that the distinct roll passes and inter-pass ranges differ in their influence on the elimination of temperature deviation. It was supposed that the depression of variance could be correlated with the temperature change in the respective pass or inter-pass range. Figure 4 shows the dependence of the relative change in temperature standard deviation, which is the absolute change in standard variation normed on the current standard deviation, in dependence on the absolute change in temperature within a pass or transport (inter-pass range). Approximately, linear correlations can be observed if roll passes and transport are regarded separately. The linear regression of the transports goes approximately through the origin, which seems natural, since no change in temperature will effect no change in temperature deviation as well. The case is different for the roll passes, where a zero temperature change does nevertheless effect a decrease of deviation. This is explained by counteracting temperature influences in roll

passes. A zero temperature change in transports means that no heat flows occur, since usually there is no significant heat generation present (aside possible phase transformations, which were neglected here). However, in roll passes, zero temperature change means that heat generation by deformation is in equilibrium with heat loss by roll contact. This could also explain the higher scatter of the roll pass observations around the linear regression.

Summary and Conclusion

A Monte Carlo method was applied to investigate the variational behavior of a rolling process regarding shape and temperature evolution. Variations were found to tend to vanish along the process line. Shape deviations were found to vanish rapidly within a few roll passes. Temperature deviations were found to decrease, but remain remarkable until the last pass. A linear correlation between the decrease in standard deviation and the temperature change within a roll pass or inter-pass range was identified. From previous investigations [10] it is known, that variations arising in the process tend to accumulate in contrast to the input variations investigated here.

These observations lead to the following conclusions regarding the variational behavior of rolling processes:

- Shape deviations of the input workpiece are of minor importance.
- Uniform heating preliminary to the rolling process is of high importance for uniformity of output workpiece properties.
- Large changes applied in processing steps on a certain property help to achieve low deviations in this property.
- Introduction of additional variations in the process has to be avoided.

These conclusions are in accordance to practical knowledge.

References

- [1] C. Lemieux, Monte Carlo and Quasi-Monte Carlo Sampling. Springer New York, 2009. doi: 10.1007/978-0-387-78165-5.
- [2] C.-Y. Lin, W.-H. Huang, M.-C. Jeng, and J.-L. Doong, ‘Study of an assembly tolerance allocation model based on Monte Carlo simulation’, *Journal of Materials Processing Technology*, vol. 70, no. 1, pp. 9–16, Oct. 1997, doi: 10.1016/S0924-0136(97)00034-4.
- [3] Z. Shen, G. Ameta, J. J. Shah, and J. K. Davidson, ‘A Comparative Study Of Tolerance Analysis Methods’, *Journal of Computing and Information Science in Engineering*, vol. 5, no. 3, pp. 247–256, May 2005, doi: 10.1115/1.1979509.

- [4] J.-Y. Dantan and A.-J. Qureshi, ‘Worst-case and statistical tolerance analysis based on quantified constraint satisfaction problems and Monte Carlo simulation’, *Computer-Aided Design*, vol. 41, no. 1, pp. 1–12, Jan. 2009, doi: 10.1016/j.cad.2008.11.003.
- [5] A.-J. Qureshi, J.-Y. Dantan, V. Sabri, P. Beaucaire, and N. Gayton, ‘A statistical tolerance analysis approach for over-constrained mechanism based on optimization and Monte Carlo simulation’, *Computer-Aided Design*, vol. 44, no. 2, pp. 132–142, Feb. 2012, doi: 10.1016/j.cad.2011.10.004.
- [6] H. Yan, X. Wu, and J. Yang, ‘Application of Monte Carlo Method in Tolerance Analysis’, *Procedia CIRP*, vol. 27, pp. 281–285, Jan. 2015, doi: 10.1016/j.procir.2015.04.079.
- [7] C. Rausch, M. Nahangi, C. Haas, and W. Liang, ‘Monte Carlo simulation for tolerance analysis in prefabrication and offsite construction’, *Automation in Construction*, vol. 103, pp. 300–314, Jul. 2019, doi: 10.1016/j.autcon.2019.03.026.
- [8] M. Weiner, M. Schmidtchen, and U. Prah, ‘A New Approach for Sintering Simulation of Irregularly Shaped Powder Particles – Part I: Model Development and Case Studies’, *Adv Eng Mater*, Feb. 2022, doi: 10.1002/adem.202101513.
- [9] M. Weiner, T. Zienert, M. Schmidtchen, J. Hubáľková, C. G. Aneziris, and U. Prah, ‘A New Approach for Sintering Simulation of Irregularly Shaped Powder Particles – Part II: Statistical Powder Modelling’, *Adv Eng Mater*, Jun. 2022, doi: 10.1002/adem.202200443.
- [10] M. Weiner, ‘Estimation of rolling process variation by usage of a Monte-Carlo method’, presented at the ESAFORM 2023, May 2023, pp. 1575–1582. doi: 10.21741/9781644902479-170.
- [11] M. Weiner, Renzing, C., M. Stirl, and M. Schmidtchen, ‘PyRoLL - An Extensible Open-Source Framework for Rolling Simulation’, *Journal of Open Source Software*, Jan. 2024, doi: 10.21105/joss.06200.
- [12] A. Hensel and T. Spittel, *Kraft- und Arbeitsbedarf bildsamer Formgebungsverfahren*. Leipzig: VEB Deutscher Verlag für Grundstoffindustrie, 1978.
- [13] A. Hensel, P. Poluchin, and W. Poluchin, *Technologie der Metallformung*, 1st ed., vol. 1. Leipzig: Deutscher Verlag für Grundstoffindustrie, 1990.
- [14] G. Zouhar, *Umformungskräfte beim Walzen in Streckkaliberreihen*, vol. 1. Berlin: Akademie Verlag Berlin, 1960.
- [15] J. H. Hitchcock and W. Trinks, ‘Roll neck bearings’, ASME, New York, Report of Special Research Committee on Roll Neck Bearings, 1935.
- [16] A. E. Lendl, ‘Rolled Bars - Part I - Calculation of Spread between non parallel roll surfaces’, *Iron and Steel*, vol. 21, no. 14, pp. 397–402, 1948.

- [17] A. E. Lendl, 'Rolled Bars - Part II - Application of Spread Calculation to Pass Design', Iron and Steel, vol. 21, no. 14, pp. 601–604, 1948.
- [18] A. E. Lendl, 'Rolled Bars - Part III - Application of Spread Calculation to Diamond Passes', Iron and Steel, vol. 22, no. 12, pp. 499–501, 1949.
- [19] Z. Wusatowski, Fundamentals of Rolling, vol. 1. London: Pergamon Press, 1969.
- [20] PyRoll v2.1.3 Documentation. <https://pyroll.readthedocs.io>.

The effect of Fe impurity on the electrodeposition of Zn from spent pickling liquor

Hanna Zakiyya^{1*}, Tamás Kékesi^{1*}

¹ Institute of Chemical Metallurgy and Foundry Engineering, University of Miskolc, H-3515 Miskolc, Egyetemváros, Hungary

* Corresponding contact: hannazakiyya@gmail.com

The potentiodynamic experiments were performed to understand the Zn electrodeposition characteristics with the Fe impurity co-existence. The effect of Fe on the electrodeposition of Zn from simulated spent pickling liquor was conducted by keeping Zn concentration at 90 g dm^{-3} . In contrast, the Fe^{3+} concentrations varied in stationary and stirred electrolytes. Iron in the zinc chloride solution changes the electrolyte nature and conditions for metal deposition. Iron promotes the reduction of hydrogen ions and causes an escalation of the local pH at the cathode. Besides decreasing the efficiency of Zn deposition, iron severely impacts the purity and morphology of the cathode deposit. It was found that the effect of iron concentration on the polarization curves is complex. Initially, it enhances the formation of hydrogen bubbles. Further, increased iron concentrations may make the composition of the Zn-Fe deposit dominantly in favour of iron, resulting in a hydrogen-dominated cathodic mechanism. The loss of the dendritic structure also characterises it – attributed mostly to zinc deposition when hydrogen bubbles are not blocking the cathode. With stirring, it was found that the polarization curves tend to be considerably steeper, indicating the importance of the transport of metal ions especially. As a related effect, however, stirring also helps metal deposition by removing the more giant hydrogen bubbles that partially block the active electrode surface. As the evolution of hydrogen is appreciably stronger in the iron-containing solutions, the physical stability of the deposited crystals is decreased, and iron powder may especially get mixed in the electrolyte during the electrodeposition process.

Keywords: SPL, Zn Electrodeposition, Fe co-deposition, Zn recovery.

1. Introduction

The economically significant part of recovering metal from spent pickling liquor (SPL) is pure metal production. In the stripping plan, the primary goal is the production of pure zinc, which is possible by cathodic deposition. However, the purity of the metal produced would significantly depend on the concentration of the significant accompanying species in the solution, namely iron. Spent pickling liquor, primer liquid waste from the hot dip galvanizing (HDG) industry, comprises various metal compositions obtained from pickling applied before the galvanization process. If produced along the lines of recycling Zn-coated objects, the exhausted solution would be especially rich in zinc, often reaching an $80\text{--}200 \text{ g/dm}^3$ level, while Fe is present at about $10\text{--}20 \text{ g/dm}^3$ concentrations, along with the rest of HCl about $10\text{--}30 \text{ g/dm}^3$ [1–3]. This – so-called Zn-stripping SPL is also characterized by a trace amount of other metals, such as Mn, Al, Cr, Ni, Cu, Co, and Cd, in the total range of less than 1 g/dm^3 [4, 5]. Although

electrochemical separation of various metals in the solution can be done according to the relative potential differences, the co-deposition conditions may curb the efficiency.

Theoretically, iron has a more positive reduction potential than zinc. Thus, the zinc electrodeposition from a Zn-Fe mixed chloride solution may have interfered with the primary cathodic process caused by the side reactions with the iron species. On the other hand, some researchers argue that the co-existence of all iron group metals, including Ni and Co, which also exist in the SPL at concentrations not more than 20 mg/dm^3 , may undergo anomalous deposition [6–9], in which case less noble metals may become preferentially deposited. This apparent inhibiting effect is generally strongest if the occurring limiting current diminishes the kinetically controlled reaction rate of the noble metal. Iron deposition was reported to be highly inhibited in a chloride medium by increasing Zn(II) [7]. Concerning the ambiguity of the Fe effect on the electrodeposition of Zn as a significant contaminant, the impact of Fe concentration on the processed solution is a central question.

2. Experimental set-up

The electrolyte solutions were prepared from analytical grade ZnCl_2 and $\text{FeCl}_3 \cdot 6\text{H}_2\text{O}$ chemicals dissolved in distilled water. The potentiodynamic experiments were performed with 85 cm^3 volume of the solutions. In this series of experiments, the Zn^{2+} concentration was usually kept constant at 90 g dm^{-3} , while the Fe^{3+} concentrations were set as 5, 15, and 30 dm^{-3} , in the range relevant to the SPL liquors. No hydrochloric acid was added to modify the pH, whose initial value ranged usually from 1.0 to 1.3.

An electrolysis cell of rectangular cross-section with the dimensions of $50 \times 50 \times 50 \text{ mm}$ made of glass was used. The capillary tip of the saturated calomel reference electrode was placed close to the surface of the cathode (work electrode) through a bridge tube ending in a Luggin-capillary tip (of 1 mm diameter) and filled with the electrolyte solution. The anode (counter electrode) was made of pure zinc to compensate for the loss of Zn^{2+} concentration caused by the repeated cycles of cathodic deposition. The electrolyte solution was partly refreshed after each setting of the parameters but not so between the parallel potentiodynamic runs. However, the evaluation was based on the average values of the overpotential-current plots taken as the averages of the minimum three parallel (repeated) results.

The initial cathode was made of copper plate with an active surface of 2 cm^2 , and the anode was made of pure zinc rods of 5 mm diameter connected to form a larger surface. The active cathode surface was polished with 800 grit SiC paper, washed with distilled water and acetone, and dried before setting into the cell. All the runs were carried out at room temperature with a

40 mV/s continuous polarization speed and a 10 s^{-1} sampling rate, giving the broadest range of clear results.

3. Experimental results

Comparing the Zn-only polarization graph to those resulting from similar solutions but containing some iron additions can be seen in Figure 1a, b, c and d. The stirring in Zn-only electrolytes depressed the irregular growth of the deposits. It can be inferred from the change in the slope, which shows that the higher the stirring speed, the gentler the slope will be. In the case of a solution containing iron, stirring also seems to help metal deposition as it detaches the H_2 bubbles from the cathode surface, promoting the initial deposition. It was observed that more metal was deposited with a higher stirring speed. As shown in Figure 1, the deposition rate increases with increased stirring speed. However, with 5 g/dm^3 iron addition, the deposition rate changed when the stirring speed was 800 r.p.m.

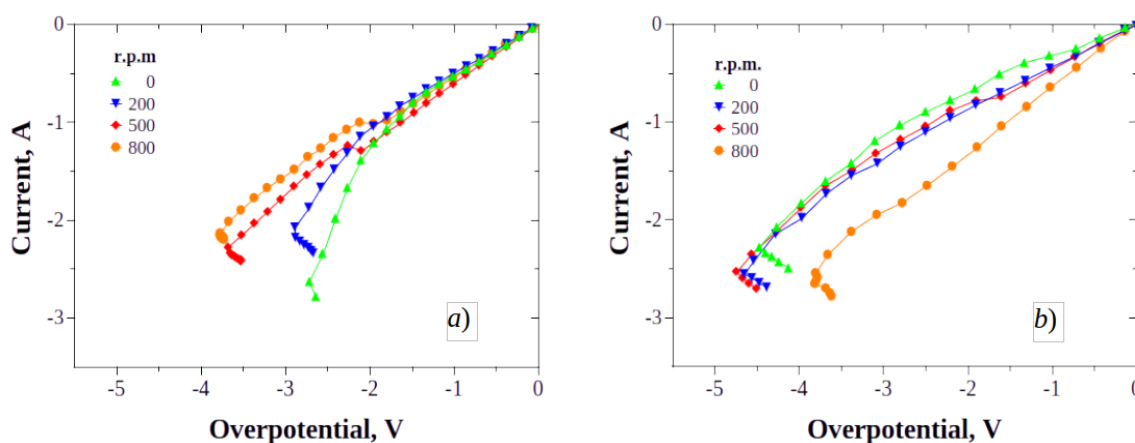


Figure 1: Effect of stirring speed on the deposition of zinc solution and zinc with iron addition (a) 0 g/dm^3 , (b) 5 g/dm^3 .

In general, the curves are steeper, as stirring of the electrolyte enhances the supply of electroactive ions to the cathode's surface, enhancing the current's development. Still, the acceleration in the current is not only caused by the faster deposition of metal alone but also by hydrogen reduction. When iron was added to the solution, forming the primarily dendritic Zn deposit could also enhance iron deposition. Also, the higher stirring speeds would improve the supply of iron to the cathode surface. Thus, more iron might be deposited as the available iron concentration near the surface increases.

Introducing the iron concentration to the stationary solution caused a decrease in the obtained current. Hydrogen bubbles resulting from the reduction of H^+ periodically blocked the cathode surface and hindered the metal deposition. It can be seen from the graphs of Fig. 1 that with

approximately 2.5 V cathode potential, with the stationary and iron-free solution, 2.7 A current can be attained, while with the same setting, all the other graphs only reached about 1 A. It is observed that the generated current tends to be decreased by increasing iron concentration in the 0–30 g/dm³ range, Figure 1 and 2.

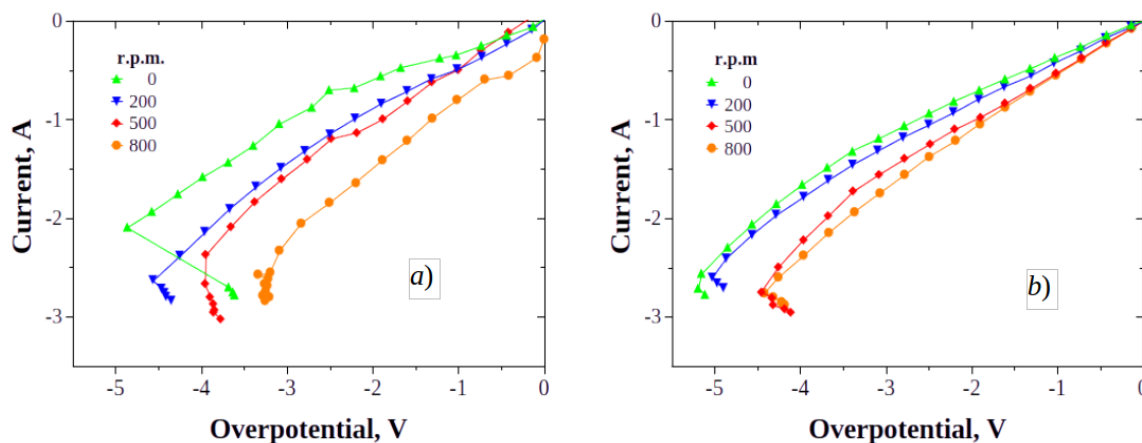
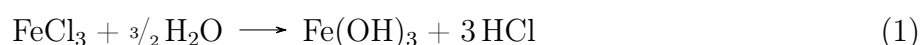


Figure 2: Effect of stirring speed on the deposition of zinc solution and zinc with iron addition (a) 15 g/dm³, (b) 30 g/dm³.

Another remarkable difference is found in the changing of the slopes during polarization. In the case of the pure zinc solution – and if the added iron concentration was very low – the curve slope increased as the cathodic polarization increased. This reflects a more vigorous formation of dendrites, i.e. a faster growth of the actual surface. However, the slope remains constant if iron is added to the solution at higher proportions. This contradicts the suggestion of the Butler-Volmer-Erdey relationship [18]. This discrepancy can be explained by the blocking effect of the evolved hydrogen bubbles adhering to the cathode surface for a while. Thus, the more constant the slope of the polarization curve is, the more dominant the hydrogen reduction can be. It can be seen in the case of the highest iron concentrations in the electrolyte.

The observed voltage ranges may express a further difference in the shapes of the polarization curves and the potential backdrop that finally occurs, forming a virtual hook. As the potentiostat is capable of supplying a total voltage of only 10 V, the conditions may also be limited at the end of the polarization runs by the voltage drop required to drive the current through the main cell from the counter electrode (anode) to the working electrode (cathode). If the polarization curve can span only a short potential range, the resistivity of the complete electric circuit may be high. With the applied constant anode-cathode distance, it is also a good indication of the resistivity of the solution. In the case of iron addition, the hydrolytic conditions expressed by the following reaction



resulted in a more acidic solution (pH 1–1.3), which allowed the relative potential of the cathode to develop further. In the case of the pure zinc solution, on the other hand, the actual surface of the cathode was quickly changed for a larger area by the effectively developed dendrites requiring less polarization potential. Still, the whole electric circuit reached the maximum voltage supplied by the instrument as the solution was closer to the neutral state (pH 4–5). This is an apparent reason why iron addition to the ZnCl_2 electrolyte solution was found to enhance hydrogen evolution during cathodic polarization.

In earlier experiments, the polarization curves were significantly steeper with stirring, showing the importance of ion transport. Stirring, on the other hand, may also enhance metal deposition by eliminating bigger hydrogen bubbles that partially cover the active electrode surface. If iron is present at higher concentrations, the catalytic hydrogen evolution can become much stronger, and the adhesion of deposited crystals is reduced. This way, iron powder may be mixed in the electrolyte during electrodeposition. A high iron concentration in the solution is unsuitable for getting the desired cathode zinc purity. Furthermore, some actual spent pickling liquors may also contain other electropositive metals such as Ni, Pb, Co, Cr, and Cu [10]. The more noble practical impurities (especially Cu and Ni), which are more likely to be deposited, could threaten the product purity. Also, the promotion of hydrogen evolution may have a disturbing effect. Impurities may impair current efficiency and increase energy consumption, in addition to their negative impacts on purity [11]. Therefore, the purification of the zinc-bearing solution (prepared to model the SPL) had to be further developed in this research phase. Also, the effects of the remaining – minor – iron concentrations in the purified electrolyte needed further experimental study.

The processes have been tracked by the potentiodynamic technique applied to freshly prepared cathode surfaces and solutions of different concentrations agitated at various strengths. It has been observed that the high iron concentrations in solutions corresponding to the raw SPL may dramatically change the composition of the cathodic deposit, as illustrated in Figure 3. It is evident that the stirring intensity strongly affects the rate of zinc deposition.

Increasing contamination of Fe will increase hydrogen evolution. The H_2 bubbles initially block, then give an extra stirring, enhancing the transport of the zinc ions. Fe deposit increases quickly as Fe concentration is increased beyond 30 g/dm^3 . The anomalous Zn electrodeposition appeared strongest in the concentration range of Fe around $45\text{--}60 \text{ g/dm}^3$. This interesting – and beneficial – phenomenon needs further confirmation by the galvanostatic experimental technique to be applied in the coming research phase. Furthermore, just at this concentration range, the deposition rate of iron also started to increase, thus indicating that the anomalous behaviour gets weaker if the iron concentration increases. That must be considered a real challenge for the purity of the Zn deposit obtained by longer electrowinning runs, indicating the importance of the solution purification step before the electrodeposition.

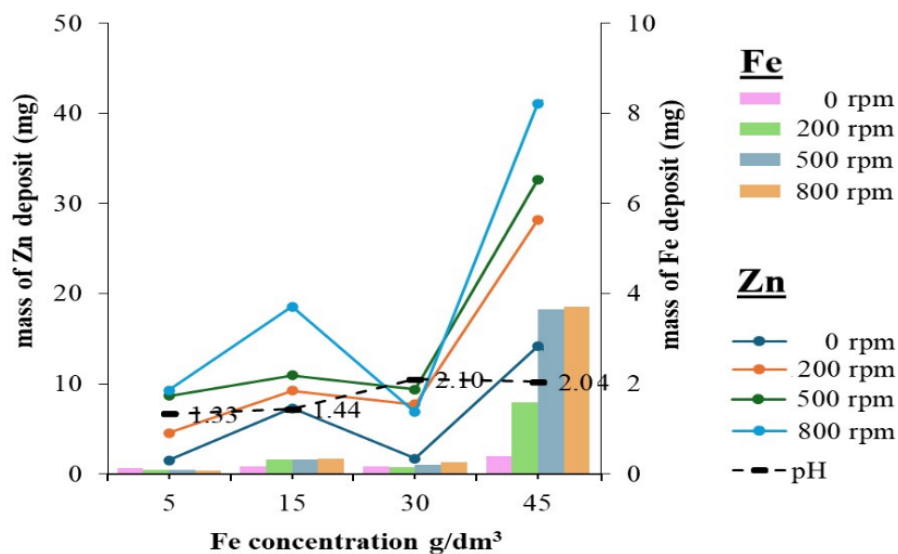


Figure 3: Deposit composition of 90 g/dm³ Zn with various concentration of Fe (pH 1.8, 75 s, 40 mV/s cathodic polarization).

4. Conclusions

Iron in the zinc chloride solution changes the electrolyte nature and conditions for metal deposition. The dark orange indicates that the added iron existed in Fe(III) species. As FeCl₃ was added, the pH of the pure or Zn-based solutions dropped to the range of 1–1.3. This condition enhanced the cathodic evolution of hydrogen. The iron concentration affects the appearance of the final deposit, which tends to be darker as more iron is added. With stirring, it was found that the polarization curves tend to be considerably steeper, indicating the importance of the transport of metal ions especially. As a related effect, however, stirring also helps metal deposition by removing the more giant hydrogen bubbles that partially block the active electrode surface. As hydrogen evolution is appreciably stronger in the iron-containing solutions, the deposited crystals' physical stability is decreased, especially since iron powder may get mixed in the electrolyte during the electrodeposition process. Increasing iron concentration indicated more hydrogen reduction on the cathode surface. It was found that the effect of iron concentration on the polarization curves is complex. Initially, it hurts the generated cathodic current because of the enhancement of hydrogen bubble formation. At a higher concentration range, however, iron deposits at a relatively higher rate, also indicated by the darker colour of the obtained layer. Further, increased iron concentrations may make the composition of the Zn-Fe deposit dominantly in favour of iron, resulting in a hydrogen-dominated cathodic mechanism. The loss of the dendritic structure also characterises it, mainly attributed to zinc deposition when hydrogen bubbles do not block the cathode. As the gas evolution becomes more characteristic, the deposit becomes more powdery. Under such conditions, the cathode becomes smoother, and the active surface is reduced. The powder was easily detached from the cathode surface by increasing the stirring speed.

References

- [1] M. Regel-Rosocka, L. Nowak and M. Wisniewski, 'Removal of zinc(II) and iron ions from chloride solutions with phosphonium ionic liquids', *Sep. Purif. Technol.*, vol. 97, pp. 158-163, 2012. <https://doi.org/10.1016/j.seppur.2012.01.035>.
- [2] J. Carrillo-Abad, M. Garcia-Gabaldon and V. Perez-Herranz, 'Treatment of spent pickling baths coming from hot dip galvanizing by means of an electrochemical membrane reactor', *Desalination*, vol. 343, pp. 38-47, 2014. <http://dx.doi.org/10.1016/j.desal.2013.11.040>.
- [3] A. Agrawal and K. K. Sahu, 'An overview of the recovery of acid from spent acidic solutions from steel and electroplating industries', *J. Hazard. Mater.*, vol. 171, no. 1-3, pp. 61-75, 2009. <https://doi.org/10.1016/j.jhazmat.2009.06.099>.
- [4] R. Gueccia, D. Winter, S. Randazzo, A. Cipollina, J. Koschikowski and G. D. Micale, 'An integrated approach for the HCl and metals recovery from waste pickling solutions: pilot plant and design operations', *Chem. Eng. Res. Des.*, vol. 168, pp. 383-396, 2012. <https://doi.org/10.1016/j.cherd.2021.02.016>.
- [5] A. Arguillarena, M. Margallo, A. Arruti-Ferbandez, J. Pinedo, P. Gomez, I. Ortisz and A. Urutiaga, 'Circular economy in hot-dip galvanizing with zinc and iron recovery from spent pickling acids', *RCS Adv.*, vol. 13, no. 10, pp. 6481-6489, 2023. <https://doi.org/10.1039/d2ra08195d>.
- [6] N. Zech, E. Podlaha and D. Landolt, 'Anomalous Codeposition of Iron Group Metals I. Experimental Result', *Journal of The Electrochemical Society*, vol. 8, no. 146, pp. 2886-28891, 1999.
- [7] S. Díaz, O. Mattos, O. Barcia and F. Miranda, 'ZnFe anomalous electrodeposition: stationaries and local pH measurements', *Electrochimica Acta*, vol. 47, pp. 4091-4100, 2002.
- [8] E. Gómez, E. Pelaez and E. Vallésa, 'Electrodeposition of zinc+iron alloys: I. Analysis of the initial stages of the anomalous codeposition', *Journal of Electroanalytical Chemistry*, vol. 469, no. 2, pp. 139-149, 1999.
- [9] Á. Llavona, LucasPérez, M. CarmenSánchez and V. Manuela, 'Enhancement of anomalous codeposition in the synthesis of Fe-Ni alloys in nanopores', *Electrochimica Acta*, vol. 106, pp. 392-397, 2013.
- [10] M. Regel-Rosocka, 'A review on methods of regeneration of spent pickling solutions from steel processing', *Journal of Hazardous Materials*, vol. 177, no. 1-3, pp. 57-69, 2010.

- [11] B. Tang, W. Su, J. Wang, F. Fu, G. Yu and J. Zhang, 'Minimizing the creation of spent pickling liquors in a pickling process with high-concentration hydrochloric acid solutions: Mechanism and evaluation method', *Journal of Environmental Management*, vol. 98, no. 1, pp. 147-154, 2012.



Metallurgiestudenten
zu Freiberg e.V.

**Kontakte im Studium
und darüber hinaus!**

Stammtische, Exkursionen,
International Students' Day of Metallurgy



Traditionspflege & Networking
Finanz. Unterstützung von Studierenden
Werde Mitglied:  info@metallurgiestudenten.de
 www.metallurgiestudenten.de

Thanks to all Sponsors!

